

# Florida State University Libraries

---

Electronic Theses, Treatises and Dissertations

The Graduate School

---

2011

## Targeted Dye Labeling as a Tool for Imaging Material and Biomaterial Microenvironments

Steven Michael Hira



THE FLORIDA STATE UNIVERSITY  
COLLEGE OF ARTS AND SCIENCES

TARGETED DYE LABELING AS A TOOL FOR IMAGING MATERIAL AND  
BIOMATERIAL MICROENVIRONMENTS

By

STEVEN MICHAEL HIRA

A Dissertation submitted to the  
Department of Chemistry and Biochemistry  
in partial fulfillment of the  
requirements for the degree of  
Doctor of Philosophy

Degree Awarded:  
Spring Semester, 2011

The members of the committee approve the dissertation of Steven Michael Hira defended on March 28<sup>th</sup>, 2011.

---

Geoffrey F. Strouse  
Professor Directing Dissertation

---

P. Bryant Chase  
University Representative

---

Albert E. Stigman  
Committee Member

---

Naresh S. Dalal  
Committee Member

Approved:

---

Joseph B. Schlenoff, Chair, Department of Chemistry and Biochemistry

The Graduate School has verified and approved the above-named committee members.

Dedicated to those that matter most – friends and family

## ACKNOWLEDGEMENTS

First and foremost, I would like to thank my major professor and advisor, Prof. Geoffrey F. Strouse for the opportunity to study under his direction and grow intellectually while completing my doctoral degree. During my time at Florida State University (FSU) he inspired me to target and conduct research on various aspects of chemistry, even expanding into the fields of biology, physics, and engineering. Most importantly, Prof. Strouse taught me how to learn. I would also like to thank my doctoral committee, Prof. Strouse, Prof. Albert E. Stiegman, Prof. Naresh S. Dalal, and Prof. P. Bryant Chase, for their mentoring and support. Throughout my graduate career I have had the unique opportunity to work with a host of talented graduate students, post-docs, research faculty, staff, and faculty in numerous departments at FSU and elsewhere at other institutions. In particular, I had the pleasure of collaborating with Prof. Linda S. Hirst and Dr. Jing Yuan on imaging the sorting of lipid mixtures in tubules (**Chapter 2**), the Strouse research group members concerning nanomaterials (**Chapter 2**), Prof. D. Tyler McQuade, Dr. Brian P. Mason, Dr. Massimo Carraro on targeted dye-labeling of polymer microcapsules and their application to biological systems (**Chapter 2**), Dr. Brian P. Mason, Dr. Chad A. Stoltz, and Dr. Colin W. Roberts on the microscopy characterization of energetic materials (**Chapter 3**), Dr. Khaled Aledealat, Kansheng Chen, Dr. Mark Field, Dr. Gerald J. Sullivan, Prof. P. Bryant Chase, Prof. Peng Xiong, and Prof. Stephan von Molnár on the detection of DNA using Hall magnetometry and fluorescent microscopy (**Chapter 4**), and Dr. M. Dru Roycik, Dale B. Bosco, Prof. Jian Cao, Dr. Yonghao Jin, Prof. Martin A. Schwartz, and Prof. Qing-Xiang Amy Sang for investigating the world of matrix metalloproteinases (**Chapter 5**). Funding for research accomplished within this dissertation was made possible by the National Institute of Health (NIH) grants # 5R01EB000832 and # GM079592, Navy Surface Warfare Center (NSWC) – Indian Head, Materials Research Technology (MARTECH) at FSU, and the Chemistry Department at FSU. I would also like to thank Ric Villani for all of his expert advice in optical microscopy. In addition, I would also like to thank all of the office and technical staff that has helped me throughout my time at FSU. I deeply appreciate my time in Tallahassee, where I am truly grateful of the close friendships that I have been able to form over the years. Lastly, I want to thank all of my friends and family for their support while I pursued

my dreams. As I transition to the next phase of my career, I will never forget those that introduced me to the science that I enjoy researching and those that have supported me along the way.

# TABLE OF CONTENTS

List of Tables .....	ix
List of Figures .....	x
List of Symbols .....	xviii
Abstract .....	xxii
1. GENERAL INTRODUCTION .....	1
1.1 Background .....	1
1.2 Literature Examples of Targeted Dye-labeling .....	2
1.3 Relevant Microscopy Techniques .....	3
1.4 Summary of Remaining Chapters .....	5
2. IMAGING DISTINCT ENVIRONS IN SYNTHETIC AND NATURALLY OCCURRING MICROENVIRONMENTS .....	7
2.1 Introduction .....	7
2.2 Lipid Tubules .....	10
2.2.1 Lipid Tubule Preparation .....	10
2.2.2 Microscopy Details .....	11
2.2.3 Photoinduced Banded Lipid Tubules .....	11
2.3 Nanomaterials .....	12
2.3.1 Microscopy Details .....	12
2.3.2 Nanomaterial Cellular Imaging .....	12
2.2.3 NSET Molecular Beacon Assay and Nanomaterial Cellular Transfer .....	16
2.4 Synthetic Polymer Microcapsules .....	18
2.4.1 Polymer Microcapsule Formation .....	18
2.4.2 Microscopy Details .....	19
2.4.3 Polymer Microcapsule Labeling .....	19
2.4.4 Triple Labeled Polymer Microcapsules .....	20
2.4.5 Cellular Uptake of Microcapsules into CHO cells .....	22
2.5 Conclusions and Future Directions .....	24
3. PROBING SOLVENT INCLUSIONS IN ENERGETIC CRYSTALS USING TARGETED DYE LABELING .....	25
3.1 Introduction .....	25
3.2 RDX Recrystallization .....	27
3.3 Microscopy Details .....	28
3.4 Microscopy Analysis of RDX .....	28
3.5 Evaluation of Two Distinct Recrystallization Methods .....	35
3.6 Conclusions and Future Directions .....	36

4. DETECTION OF TARGET SINGLE STRANDED DNA USING A MICRO-FABRICATED HALL MAGNETOMETER WITH CORRELATED OPTICAL READOUTY .....	38
4.1 Introduction .....	38
4.2 Experimental .....	40
4.2.1 Substrate Fabrication .....	40
4.2.2 Substrate Cleaning .....	42
4.2.3 Substrate Passivation .....	43
4.2.4 Synthetic DNA Design .....	46
4.2.5 DNA Immobilization and Hybridization .....	48
4.2.6 Microscopy Details .....	49
4.2.7 Hall Measurement Details .....	51
4.3 Results and Discussion .....	51
4.3.1 Design .....	51
4.3.2 Detection .....	53
4.3.3 Sensitivity .....	58
4.3.4 Selectivity and Detection Limits .....	59
4.4 Conclusions and Future Directions .....	61
5. LIVE-CELL OPTICAL TRACKING OF A NOVEL DYE-LABELED MATRIX METALLOPROTEINASE INHIBITOR (MMPI) IN LNCAP AND LNCAP-MT1-GFP CELL LINES .....	63
5.1 Introduction .....	63
5.2 Syntheses of Dye-labeled Target MMPI and Controls .....	70
5.2.1 Synthesis of Disulfide Protected Dye-labeled Target MMPI (YHJ-8-91) .....	70
5.2.2 Syntheses of YHJ-8-89 and C <sub>3</sub> DyeControls .....	72
5.3 Quantification of Target MMPI and Controls .....	72
5.4 Microscopy Details .....	73
5.5 Cellular Uptake of Target MMPI in LNCaP and LNCaP-MT1-GFP Cell lines .....	74
5.6 Cellular Uptake of YHJ-8-91, YHJ-8-89, and C <sub>3</sub> Dye in LNCaP-MT1-GFP .....	77
5.7 Quantification of Cellular Uptake of YHJ-8-91, YHJ-8-89, and C <sub>3</sub> Dye in LNCaP-MT1-GFP .....	78
5.8 Qualitative Time-Dependant Cellular Uptake of YHJ-8-91 .....	82
5.9 Probing MMPI-MMP Interactions Using Zymography .....	83
5.10 Conclusions and Future Directions .....	84
APPENDICES .....	86
A. KHÖLER ILLUMINATION ALIGNMENT PROTOCOL .....	86
B. NMR SPECTRA OF FITC-ACETYLENE .....	87
C. THEORETICAL HALL SENSITIVITY CALCULATIONS .....	91
D. MASS SPECTROGRAM OF TARGET MMPI .....	92
E. NMR SPECTRA OF YHJ-8-91, YHJ-8-89, and C <sub>3</sub> Dye .....	93

F.	ANOVA STATISTICS ON THE CELLULAR UPTAKE OF THE MMPI AND CONTROLS .....	99
G.	COPYRIGHT RELEASE FORMS .....	100
	REFERENCES .....	102
	BIOGRAPHICAL SKETCH .....	118

## LIST OF TABLES

5.1. Characteristics of designed synthetic DNA using IDT DNA Oligo Analyzer 3.1. ....	45
F1. ANOVA Statistics on the quantification of cellular uptake of YHJ-8-91, YHJ-8-89, and C <sub>3</sub> Dye 6 hours post incubation. ....	99

## LIST OF FIGURES

1.1. Labeled components of a modern microscopy platform.....	3
2.1. Photo-initiated lipid sorting into disordered (red) and ordered (blue) liquid phases (a,b). Line-scan analysis across (b) showing distinct morphological characteristics for disordered (left, red) and ordered (right, blue) phases (c). Scale bars = 5 $\mu\text{m}$ .....	10
2.2. LSCM micrographs showing the cellular uptake of InP/ZnSMUA passivated quantum dots using Optifect™ 24 hours post transfection. (a) The TLD-DIC image overlaid with quantum dots (green) and cell membrane stain (red). (b) Quantum dot (green) and cell membrane (red) fluorescence overlaid image. (c) The 3-D reconstruction image of InP/ZnS quantum dots (green) and cell membrane stain (red) overlay. Scale bars = 5 $\mu\text{m}$ . ....	14
2.3. LSCM micrographs showing the cellular uptake of InP/ZnSMUA passivated quantum dots using Optifect™ 24 hours post transfection. (a) The TLD-DIC image overlaid with nucleus (blue), quantum dots (green), and cell membrane stain (red). (b) Nucleus (blue), quantum dot (green), and cell membrane (red) fluorescence overlaid image. (c) The triply stained 3-D reconstruction image of InP/ZnS quantum dots (green) and cell membrane stain (red) overlay. Scale bars = 5 $\mu\text{m}$ .....	15
2.4. Wide-field fluorescence micrographs showing the cellular uptake of 5.7 nm Au nanoparticles passivated with fluorescein labeled dsDNA using Optifect™ 24 hours post transfection. (a) The DIC image overlaid with fluorescein fluorescence(green) indicating ligand release. (b) A zoomed in region of (a) depicting fluorescein fluorescence (green) with DIC overlay and fluorescein fluorescence only (green) showing DNA release (punctate) and endosomal escape (diffuse). Scale bar = 50 $\mu\text{m}$ .....	17
2.5. Wide-field fluorescence with DIC overlaid micrographs showing cellular division and the transfer of DNA released off nanoparticle platform (green) to newly formed daughter cells at 1 hr (a), 2 hr (b), 4 hr (c) and 6 hr (d). Scale bars = 10 $\mu\text{m}$ .....	17
2.6. Pictorial representation of the synthesis of polyurea based polymer microcapsules. Taken from Mason, B.P., Hira, S.M., Strouse, G.F., McQuade, D.T. <i>Organic Letters</i> 11, 1479-1482 (2009) – Reproduced with permission by the American Chemical Society. ....	18
2.7. LSCM micrographs showing the selective labeling of Lissamine rhodamine B on the outer shell of polyurea microcapsules with encased pCMS. (a) The	

<p>TLD-DIC image overlaid with selective microcapsule shell labeling (red).  (b-c) The 3-D reconstruction of the polymer shell fluorescent labeling (red)  from two different perspectives. Scale bar = 2 <math>\mu\text{m}</math>. .....</p>	20
<p>2.8. The TLD-DIC overlay showing selective labeling of the interior (blue and  green) and the shell (red) (a). Strategy for selective microcapsule labeling  with three reactive fluorescent dyes (b). Scale bar = 5 <math>\mu\text{m}</math>. Adapted from  Mason, B.P., Hira, S.M., Strouse, G.F., McQuade, D.T. <i>Organic Letters</i> 11,  1479-1482 (2009).....</p>	20
<p>2.9. The selective simultaneous labeling of three spatially separated reactive sites  on polyurea microcapsules using cascade blue hydrazide<sup>TM</sup> (blue), FITC  acetylene (green), and Lissamine rhodamine B (red). Line-scan analysis for  each image is shown as a plot of intensity with respect to distance across the  microcapsule for each individual image. Scale bars = 5 <math>\mu\text{m}</math>. Adapted from  Mason, B.P., Hira, S.M., Strouse, G.F., McQuade, D.T. <i>Organic Letters</i> 11,  1479-1482 (2009) – Reproduced with permission by the American Chemical  Society.....</p>	21
<p>2.10. The 3-D reconstruction images of microcapsules showing the color  coordinated morphologies for cascade blue hydrazide<sup>TM</sup> (blue), fluorescein  acetylene (green), and Lissamine rhodamine B (red). Overlays of cascade blue  hydrazide<sup>TM</sup> (blue) with Lissamine rhodamine B (red) and FITC acetylene  with Lissamine rhodamine B (red) are shown for clarity. Adapted from Mason,  B.P., Hira, S.M., Strouse, G.F., McQuade, D.T. <i>Organic Letters</i> 11, 1479-1482  (2009). .....</p>	22
<p>2.11. The selective simultaneous labeling of three spatially separated reactive sites  on polyurea microcapsules using cascade blue hydrazide<sup>TM</sup> (blue), FITC  acetylene (green), and Lissamine rhodamine B (red). Line-scan analysis for  each image is shown as a plot of intensity with respect to distance across the  microcapsule for each individual image. Scale bars = 5 <math>\mu\text{m}</math>. Adapted from  Mason, B.P., Hira, S.M., Strouse, G.F., McQuade, D.T. <i>Organic Letters</i> 11,  1479-1482 (2009) – Reproduced with permission by the American Chemical  Society.....</p>	23
<p>3.1. The chemical structures for cyclotrimethylene trinitramine, known commonly  as RDX, (left) and Lissamine rhodamine B sulfonyl chloride (right). .....</p>	27
<p>3.2. Optical micrographs of RDX crystals with matching index of refraction fluid  (a) and without matching index of refraction fluid (b) showing the presence  of internal defects. Adapted from Roberts, C.W., Hira, S.M., Mason, B.P.,  Strouse, G.F. &amp; Stoltz, C.A., <i>CrystEngComm</i>, 13, 1074-1076, 2011 –  Reproduced by permission of the Royal Society of Chemistry. ....</p>	28

3.3. Optical micrographs of RDX crystals using bright-field DIC and wide-field microscopy techniques. Bright-field DIC and wide-field fluorescence overlay (a), bright-field DIC (b), and wide-field fluorescence (c) visualizing both the RDX crystal morphology (gray scale) and the presence of crystalline defects (red). Scale bars = 50 $\mu\text{m}$ . .....	30
3.4. Optical micrographs of RDX crystals using LSCM techniques. TLD-DIC and Lissamine rhodamine B sulfonyl chloride overlay (a), TLD-DIC (b), and Lissamine rhodamine B sulfonyl chloride (c) visualizing both the RDX crystal morphology (gray scale) and the presence of crystalline defects (red). Scale bars = 50 $\mu\text{m}$ . .....	31
3.5. Optical micrographs of RDX crystals using TLD-DIC and confocal microscopy techniques. TLD-DIC and Lissamine rhodamine B sulfonyl chloride overlay (a), TLD-DIC (b), and Lissamine rhodamine B sulfonyl chloride, (c) visualizing both the RDX crystal morphology (gray scale) and the presence of crystalline defects (red). An electronic magnification of the same RDX crystal (white box in (a)), where the TLD-DIC and Lissamine rhodamine B sulfonyl chloride overlay (d), TLD-DIC (e), and Lissamine rhodamine B sulfonyl chloride (f) are shown. The spectral confocal profile of the signal acquired in (g) depicts signal originating from Lissamine rhodamine B sulfonyl chloride fluorescence. Scale bars (a-c) = 20 $\mu\text{m}$ and scale bars (d-f) = 1 $\mu\text{m}$ . .....	32
3.6. Laser-induced diffraction patterns can be observed in RDX showing distinct patterns around solvent inclusions. Scale bar = 2 $\mu\text{m}$ . .....	33
3.7. The 3-D reconstruction of defects within an RDX particle shown in red from two different perspectives. ....	34
3.8. RDX particles formed using mechanical stirring agitation (a) and ultrasonic agitation (b). Scale bars = 100 $\mu\text{m}$ . Adapted from Roberts, C.W., Hira, S.M., Mason, B.P., Strouse, G.F. & Stoltz, C.A., CrystEngComm, 13, 1074-1076, 2011 – Reproduced by permission of the Royal Society of Chemistry. ....	35
3.9. The formation of RDX particles using sonocrystallization under fast solvent evaporation (a-b) and slow evaporation (c-d), where both the TLD-DIC only (a,c) and the Lissamine rhodamine B sulfonyl chloride only (b,d) images are shown. Scale bars = 20 $\mu\text{m}$ . Adapted from Roberts, C.W., Hira, S.M., Mason, B.P., Strouse, G.F. & Stoltz, C.A., CrystEngComm, 13, 1074-1076, 2011. ....	36
4.1. The composition of the Hall device heterostructure is shown, where the layers include a GaAs substrate base, layers to reduce lattice mismatches, active layers sandwiched between blocking layers, capping layers, an insulating layer, and the target molecule assembling layer. ....	41

4.2. AFM micrographs of glass substrate mimics. The quality was evaluated based on the presence of artifacts, where a good quality substrate (left) lacks excessive topological features and a poor quality substrate (right) contains excessive topological features. ....	41
4.3. X-Ray Photoelectron Spectroscopy (XPS) characterization of the reduction of Au <sub>2</sub> O <sub>3</sub> to bulk Au by an ethanol rinse. The characteristic shifts in the Au 4f (top) and O 1s peaks (bottom) are shown for native Au <sub>2</sub> O <sub>3</sub> and Au <sub>2</sub> O <sub>3</sub> rinsed with ethanol. ....	44
4.4. Native polyacrylamide gel electrophoresis characterization for the three-strand DNA assembly in the absence of nanobeads showing different mobilities of (1) visual loading dye not observed under fluorescent excitation, (2) reporter strand (disulfide 20mer) and complementary target, (3) probe strand (fluorescein labeled 15mer), (4) reporter and probe strands, (5) probe and complementary target, (6) probe and non-complementary target, (7) reporter, probe, and complementary target, (8) reporter, probe, and non-complementary target (a). The visible bands (3-8) originate from the internal fluorescein modification on the probe strand and the differences in mobility reflect the assembling of the three-strand DNA structure (a). The arrow in (7) signifies the three-strand DNA product, and the band immediately below is most likely attributed to the probe annealed to the complementary target (a). Native polyacrylamide gel electrophoresis characterization for the three-strand DNA assembly in the absence of nanobeads showing different mobilities of (1) probe strand (fluorescein labeled 35mer), (2) complementary reporter and probe strands, (3) non-complementary reporter and probe strands (b). The visible bands (1-3) originate from the internal fluorescein modification on the probe strand and the differences in mobility reflect the assembling of the two-strand DNA structure (b). ....	48
4.5. The assembly of two-strand (a-b) and three-strand (c-d) ssDNA strategies, where green fluorescence indicates the location of the SPM conjugated nanobeads. The complementary sequence (a,c) results in assembly and the non-complementary sequence (b,d) does not result in assembly. Scale bars = 50 μm. ....	50
4.6. Generalized schematic for the detection of label-free target DNA using Hall magnetometry. The label-free target DNA (black) is detected by immobilization at the Hall device via complementary base pairing with receptor DNA (blue) pre-assembled on the Hall device surface to additional complementary probe DNA (red) with an internal fluorescent marker pre-conjugated to the surface of a magnetic nanobead resulting in a detectable Hall signal. Nanobead is not drawn to scale. ....	52
4.7. Optical microscopy characterization (wide-field fluorescence and DIC overlay) of three-strand DNA assembly is shown by the presence of green	

fluorescence indicating the presence of probe DNA (a). SEM was used to evaluate the location and to quantify the number of nanobeads contributing to the Hall response for (iii), where the grey box designates the location of the underlying Hall junction (b). Hall responses for three active junctions (i, ii, iii) and a single control junction (iiic) are plotted as Hall voltage offset versus time; the presence of nanobeads over the active Hall junctions results in a drop in Hall voltage when a dc magnetic field is applied (c). The theoretical device signal stemming from a single 344 nm SPM bead is shown to the right as a function of position over the Hall junction further illustrating the local sensitivity of Hall magnetometry (d). Scale bars = 2  $\mu\text{m}$  in panels a,b. .... 54

4.8. SEM micrograph depicting label-free, three-strand DNA assembly of all six junctions of a Hall magnetometer (a). Scale bar (a) = 10  $\mu\text{m}$ . SEM micrographs at higher magnification of the three active Hall junctions, where the ratio of beads entirely or partially over the Hall junction versus beads outside of the junction are (b) 8/41, (c) 11/68, and (d) 12/73. Scale bars (b-d) = 1  $\mu\text{m}$ . Hall responses for three active junctions (i, ii, iii) and three non-active control junction (ic, iic, iiic) are plotted as Hall voltage versus time; the presence of superparamagnetic (SPM) nanobeads over the active Hall junctions results in a drop in Hall voltage when a dc magnetic field is applied (e). When the dc magnetic field is removed the signal returns to baseline (e). .... 55

4.9. Sequence-specific two-strand DNA assembly and subsequent Hall detection of a single 344 nm nanobead. (a) Pictorial representation of two-strand DNA assembly, where the probe DNA (red) is complementary to the receptor DNA (blue). (b) Hall response data for the active (iv) and control Hall junction (ivc) plotted as Hall voltage versus time, where the drop in Hall voltage corresponds to the presence of a magnetic nanobead. (c) SEM was used to confirm only one nanobead contributed significantly to the signal measured in (iv). Scale bar = 2  $\mu\text{m}$ . .... 57

4.10. The theoretical Hall device cross-sectional response for a single 344 nm SPM bead as a function of position from the center of the junction, where red indicates strongest change in voltage, aqua indicates weakest voltage change, and blue indicates a negative voltage readout. The standard deviation of the noise floor for the device is outlined in black for reference. .... 58

4.11. Three-strand DNA assembly on a mimic array (patterned on a GaAs substrate) for (a) complementary target only and (c) 10 ppm target in non-target DNA. The inlays in the lower left of (a) and (c) are an enlarged portion of (a) and (c), respectively. Scale bars = 50  $\mu\text{m}$ . A line-scan of the wide-field fluorescence microscopy image in (a) showing fluorescein-labeled probe DNA (green) and DIC (black) intensity correlates fluorescence intensity with nanobeads located

primarily over gold pads, where the black arrows signify the presence of a small number of non-specifically bound nanobeads (b). .....	60
5.1. A pictorial description of the varying domains pertinent to MMPs. Subclassifications of MMPs are shown as follows: Matrilysins (a), Collagenases (b), Stromelysins (c), Gelatinases (d), MT-MMPs (e), and synthetically modified MMPS (f). .....	65
5.2. The chemical structures of YHJ-8-91 in protected/inactive (a) and deprotected/active (b) forms, YHJ-8-89 (c), and C <sub>3</sub> Dye (d). .....	69
5.3. The reaction scheme for the synthesis of disulfide protected inhibitor. ....	71
5.4. Thin Layer Chromatography results showing the difference in mobility between disulfide protected inhibitor and unreacted Lissamine rhodamine B under white light and UV illumination (bottom). The spotted reactants and reaction mixture are shown before solvent elution (top). ....	72
5.5. The normalized offset absorption spectra of YHJ-8-91, YHJ-8-89, and C <sub>3</sub> Dye. ....	73
5.6. The cellular uptake of dye-labeled thiolated inhibitor in LNCaP-MT1-GFP. LSCM micrographs of TLD-DIC (a), MT1-GFP (b), rhodamine signature (c), and an overlay of MT1-GFP/rhodamine signature (d) are shown ~ 6.5 hrs post incubation. An electronic zoom of a portion of (a-d) is shown depicting MT1-GFP (e) and MT1-GFP/rhodamine signature overlay (f). The 3-D reconstruction image of LNCaP-MT1-GFP cells with internalized dye-labeled thiolated inhibitor after 24 hr post incubation is shown as a Hoechst 34580 (blue)/rhodamine signature (red) overlay (g). Scale bars (a-d) = 50 μm, (e-f) = 10 μm. ....	75
5.7. The cellular uptake of dye-labeled thiolated inhibitor in LNCaP-GFP. LSCM micrographs of TLD-DIC (a), GFP (b), rhodamine signature (c), and an overlay of GFP/rhodamine signature (d) are shown 4.25 hrs post incubation. An electronic zoom of a portion of (a-d) is shown depicting GFP (e) and GFP/rhodamine signature overlay (f). The 3-D reconstruction image of LNCaP-GFP cells with internalized dye-labeled thiolated inhibitor after 24 hr post incubation is shown as Hoechst 34580 (blue)/rhodamine signature (red) overlay (g). Scale bars (a-d) = 50 μm, (e-f) = 10 μm. ....	76
5.8. The qualitative cellular uptake of YHJ-8-91 (a-c), YHJ-8-89 (d-f), and C <sub>3</sub> Dye (g-i) at 1 hr (a,d,g), 2 hr (b,e,h), and 3 hr (c,f,i) post material incubation. Scale bars = 50 μm. ....	77
5.9. LSCM micrographs showing cellular uptake of YHJ-8-91 (a-e), YHJ-8-89 (f-j), and C <sub>3</sub> Dye (k-o) into LNCaP-MT1-GFP cells 6 hrs post incubation.	

The individual channels for TLD-DIC (a,f,k), Hoechst 34580 (b,g,l), MT1-GFP (c,h,m), YHJ-8-91 (d), YHJ-8-89 (i), C <sub>3</sub> Dye (n), and overlay TLD-DIC, Hoechst 34580, MT1-GFP, and respective compound (e,j,o). Scale bars = 50 $\mu$ m.....	80
5.10. A graph of the quantitative uptake of YHJ-8-91, YHJ-8-89, and C <sub>3</sub> Dye in LNCaP-MT1-GFP cells 6 hours post incubation. Error bars represent standard error. ....	81
5.11. LSCM micrographs showing the cellular uptake of YHJ-8-91 6 hours post incubation. (a) The TLD-DIC image overlaid with Hoechst 34580 (blue), MT1-GFP (green) and YHJ-8-91 (red). (b) Hoechst 34580 (blue) and YHJ-8-91 (red) fluorescence overlaid image. (c) The 3-D reconstruction image of Hoechst 34580 (blue), MT1-GFP (green), and YHJ-8-91 cell membrane stain (red) overlay. Scale bars = 5 $\mu$ m. ....	82
5.12. LSCM micrographs depicting cellular uptake of YHJ-8-91 (red) at 6, 24, and 48 hrs post incubation. ....	82
5.13. The gelatin zymogram of conditioned spent media from LNCaP-MT1-GFP cells incubated with C <sub>3</sub> Dye, YHJ-8-89, YHJ-8-91, and controls are shown, where white bands indicate gelatin digestion (a). The percentage of active MMP-2 to pro-MMP-2 from (a) shown in (b). Bar graphs indicating the level of gelatin digestion caused from MMP-2 (c) and MMP-9 (d). ....	84
A1. Labeled microscope components necessary for alignment for Khöler illumination. ....	86
B1. NMR spectrum of FITC-Acetylene. ....	87
B2. NMR spectrum of FITC-Acetylene. ....	87
B3. NMR spectrum of FITC-Acetylene. ....	88
B4. NMR spectrum of FITC-Acetylene. ....	88
B5. NMR spectrum of FITC-Acetylene. ....	89
B6. NMR spectrum of FITC-Acetylene. ....	89
B7. NMR spectrum of FITC-Acetylene ....	90
B8. NMR spectrum of FITC-Acetylene ....	90
C1. Maple v13 theoretical Hall sensitivity calculations. ....	91

D1. Mass spectrogram for target MMPI.....	92
E1. NMR spectrum of YHJ-8-91. ....	93
E2. NMR spectrum of YHJ-8-91. ....	93
E3. NMR spectrum of YHJ-8-91. ....	94
E4. NMR spectrum of YHJ-8-91. ....	94
E5. NMR spectrum of YHJ-8-89. ....	95
E6. NMR spectrum of YHJ-8-89. ....	95
E7. NMR spectrum of YHJ-8-89. ....	96
E8. NMR spectrum of YHJ-8-89. ....	96
E9. NMR spectrum of C <sub>3</sub> Dye. ....	97
E10. NMR spectrum of C <sub>3</sub> Dye. ....	97
E11. NMR spectrum of C <sub>3</sub> Dye. ....	98
G1. American Chemical Society Copyright Release. ....	100
G2. Royal Society of Chemistry Copyright Release. ....	101

## LIST OF SYMBOLS

2-D .....	two-dimensional
3-D .....	three-dimensional
AFM .....	atomic force microscopy
BARC .....	bead array counter
CHO .....	Chinese hamster ovary
CPP .....	cell penetrating peptide
DCLP .....	dichroic-long pass
DIC .....	differential interference contrast
DMEM .....	Dulbecco's modified eagle medium
DMAP .....	N,N-dimethylaminopyridine
DMF .....	dimethylformamide
DNA .....	deoxyribonucleic acid
DOPC .....	1,2-Dioleoyl-sn-glycero-3-phosphocholine
dsDNA .....	double-stranded DNA
ECM .....	extracellular matrix
ELISA .....	enzymelinkedimmunosorbant assay
ECM .....	extracellular matrix
eSM .....	(2S,3R,4E)-2-acylaminoctadec-4-ene-3-hydroxy-1-phosphocholine (egg sphingomyelin)
EtOH .....	ethanol
FITC .....	fluorescein isothiocyanate
FN .....	fibronectin

FRET.....fluorescence resonance energy transfer

GFP .....green fluorescent protein

GMR .....giant magnetoresistance

GUV .....giant unilamellar vesicle

HPLC .....high-performance liquid chromatography

$K_i$ .....inhibitor disassociation constant

LbL.....layer-by-layer

$L_d$ .....liquid disordered

$L_o$ .....liquid ordered

LNCaP-GFP .....LNCaP cells that express GFP

LNCaP-MT1-GFP.....LNCaP cells that overexpress MT1-GFP

LSCM.....laser scanning confocal microscopy

MRI.....magnetic resonance imaging

MMP .....matrix metalloproteinase

MMPI.....matrix metalloproteinase inhibitor

NMR .....nuclear magnetic resonance

NSET.....nanometal surface energy transfer

ODT .....octadecanethiol

PAGE .....polyacrylamide gel electrophoresis

pAMS .....polyazidomethylstyrene

PBS .....phosphate buffered saline

PBX.....plastic bonded explosive

pCM .....polychloromethylstyrene

PEG-silane .....	2-[Methoxy(Polyethyleneoxy)Propyl]-Trimethoxysilane
PET .....	positron emission tomography
PMPPI.....	polymethylene polyphenol isocyanate
POC.....	point-of-care
RDX .....	cyclotrimethylenetrinitramine
Rh-DPPE.....	1,2-dipalmitoyl-sn-glycero-3-phosphoethanol-amine-N-(Lissamine rhodamine B sulfonyl chloride) (ammonium salt)
SANS .....	small angle neutron scattering
SEM .....	scanning electron microscopy
SERS .....	surface enhanced Raman scattering
ssDNA.....	single-stranded DNA
SNP .....	single nucleotide polymorphism
SPM.....	superparamagnetic
TCEP.....	tris(2-carboxyethyl)-phosphine hydrochloride
TEA.....	membrane-type matrix metalloproteinases
TEPA.....	tetraethylenepentamine
THF .....	tetrahydrofuran
TIMP .....	tissue inhibitor metalloproteinase
TIRF.....	total internal reflection fluorescence
TLC .....	thin layer chromatography
TLD.....	transmitted light detector
TNT.....	trinitrotoluene
TRITC .....	tetramethylrhodamineisothiocyanate

XPS .....X-ray photoelectron spectroscopy

## ABSTRACT

The use of targeted-dye-labeling to probe environs within larger microenvironments is a powerful tool to elucidate the structure and function of specific components in materials. Combining site-specific dye-labeling with optical microscopy characterization methods can allow the tracking dynamics of protein function, the sorting of lipid mixtures as a biological mimic, and the intra-cellular monitoring of cellular proteins through the use of fluorescent proteins. The chapters included in this dissertation will focus on the use of optical microscopy as a tool to image particular fluorescently labeled targets within a surrounding microenvironment. The optical imaging of synthetic and naturally occurring vesicles is shown to be a powerful tool to follow site-specific chemical reactions in polymer microcapsules and the delivery of quantum dots to intra-cellular environments via liposomes, as well as, the sorting of lipids into distinct domains (**Chapter 2**). The implementation of a dye-labeling strategy to optically identify specific environs can be extended to energetic materials in an effort to follow the quality of recrystallization of RDX (**Chapter 3**). The strategy of dye-labeling can be extended to specifically labeling individual DNA sequences conjugated to magnetic beads to monitor and validate Hall-based DNA sequence detection using both two and three-strand DNA assembly onto condensed matter surfaces (**Chapter 4**). Finally, the use of strategically placed fluorescent dye molecules appended to matrix metalloproteinase inhibitor (MMPI) molecules will be explored to monitor the interaction of MMPIs in the presence of LNCaP-MT1-GFP cells (**Chapter 5**). The experiments described within these listed chapters illustrate the validity of utilizing targeted dye-labeling and subsequent tracking via optical microscopy methods as a tool to investigate a host of interdisciplinary research aims in an effort to push the boundaries of the frontiers of science.

# CHAPTER 1

## GENERAL INTRODUCTION

### 1.1 Background

Microscopy as a characterization tool of specimens has led directly to an abundant amount of scientific discoveries including visualizing the phase separation of lipid mixtures, the complex function of motor proteins, and use of fluorescent proteins to monitor biological processes<sup>1-3</sup>. The importance of microscopy in current scientific research can not be understated. According to the Web of Knowledge database, searches of “microscopy” yielded 5933 references (articles, reviews, and communications) in 2010, where sub-searches of “fluorescence” resulted in 2103 references in the same year. The popularization of the use of microscopy as a tool arguably began in 1665 when Robert Hooke published a book entitled *Micrographica* that revolutionized the way one views the world. The book was composed of illustrations of his microscopy observations and allowed the visualization of common everyday elements (ie. cork, fleas, flies, cheese mould, etc.) in far more detail than the naked eye alone can resolve<sup>4</sup>. The visualization of cork by Hooke led to the smallest unit of a living thing referred to as a “cell”<sup>4</sup>. Today, microscopy has evolved from the days of basic observations of everyday, tangible objects to elucidating structure and function of intricate biological specimens and advanced functional materials. In particular, microscopy coupled to targeted fluorescence dyes as a tool to probe microenvironments have pushed the frontiers of science and changed the view of how scientists think about multi-disciplinary fields of research. A few literature examples of fluorescent dye-labeling vastly impacting the global field of science will be described below to illustrate the power of microscopy to gain new insights in scientific research spanning a variety of disciplines.

## 1.2 Literature Examples of Targeted Dye-Labeling

The successful use of targeted dye-labeling as a tool to answer scientific questions in varying multi-disciplinary fields of chemistry, biology, physics, and engineering have been recently reported in literature. Three particular examples described briefly below demonstrate how new scientific insights can be ascertained through such a strategy. In 2003, Baumgart et al. were able to clearly show the separation of lipid mixtures in giant unilamellar vesicles (GUVs)<sup>3</sup>. This phenomenon is of particular interest due to the relevance to lipid bilayer membranes in biological systems. The lipid ordered ( $L_o$ ) and lipid disordered ( $L_d$ ) domains of liposomes were selectively stained with a Lissamine rhodamine B lipid derivative and a perylene dye, respectively<sup>3</sup>. The precise labeling strategy described from this research was later applied to the visualization of phase sorting of lipid tubules described in detail in **Chapter 2**. The fluorescence microscopy data obtained allowed the geometry and curvature of lipid domains to be analyzed with potential relevance to biological processes, such as endocytosis.

The second example of targeted dye-labeling as a tool to elucidate structure and function was described by Yildiz et al. concerning myosin V<sup>2</sup>. Myosin V is a motor protein responsible for transporting cargo down actin filaments within biological systems. The use of targeted dye-labeling various components of the motor allowed the motion to be described as “hand-over-hand” walking rather than “inchworm” sliding, which was the previous source of much debate<sup>2</sup>. By monitoring the fluorescent intensity of molecular dyes appended to various positions located on myosin V using a technique known as total internal reflection epifluorescence (TIRF) microscopy, the two heads of the motor clearly displayed “hand-over-hand” behavior. The ability to record the dynamic movement of motor proteins real-time opens the door for how proteins natively function in biological systems.

The last example of targeted dye-labeling is the use of fluorescent protein labeling, which clearly has revolutionized biological research and evolved into its own cross-disciplinary field involving biochemistry, organic chemistry, molecular biology, and materials science<sup>5</sup>. The discovery of green fluorescent protein (GFP) from the jellyfish *Aequorea victoria* has allowed a non-invasive approach to monitoring components of biological systems<sup>1,5,6</sup>. Since the first discovery, minute mutations in the protein have led to an entire range of fluorescent proteins spanning the entire visible spectrum<sup>6</sup>. The use of a modified GFP chimerically tagged to MT1-MMP is exploited in **Chapter 5** to simultaneously

monitor a small molecule matrix metalloproteinase inhibitor (MMPI) with one of its corresponding protein substrates. The development of fluorescent proteins as a fluorescent based labeling strategy has expanded the available tools for probing unique environs contained within much larger domains.

## Relevant Microscopy Techniques

Although crude in form compared to present technology, the microscope that was developed throughout the 1600's allowed viewing specimens in detail otherwise not known to exist. The lack of an independent recording device to document specimens in the currently viewed state caused scientists to sketch their observations. At this time, scientists had to always question the validity of illustrated representations of their microscopy observations<sup>4</sup>. Presently, artist renditions have been replaced by charge coupled devices (CCDs), photo-multiplier tubes (PMTs), and other electronically based detectors to document scientific observations. The major components of a modern state-of-the-art microscope platform used to conduct research herein are identified in **Figure 1.1** and include a light source, filters, oculars, and an image recorder. The field of microscopy has evolved into a broad class of microscope based techniques of which only a subset will be included here. The techniques most relevant to the following studies represented by the following chapters include bright-field, wide-field, and laser scanning confocal techniques. A brief introduction to these techniques will be explained below.

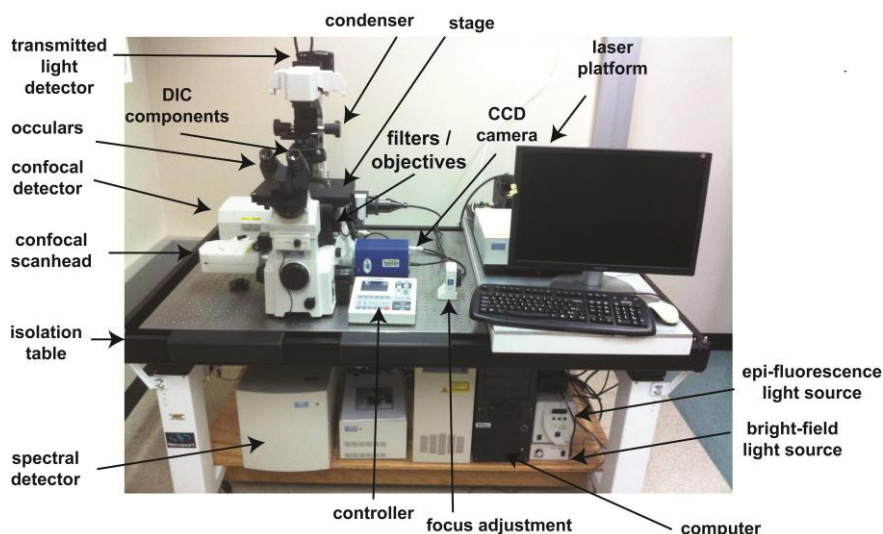


**Figure 1.1:** Labeled components of a modern microscopy platform.

Bright-field microscopy is the natural use of the absorption features of a specimen illuminated by a white light source to provide contrast for visualization<sup>7,8</sup>. The light source is usually set-up in a transmission configuration, where the light source is located on one side of the specimen and the objective is located on the other. Although it is the most common microscopy technique, it is not suitable for all applications of microscopy. Specimens of interest need to be generally thick and opaque enough to provide contrast, a characteristic not always exhibited by biological samples. Combining bright-field microscopy with an optical interference technique, differential interference contrast (DIC), can allow low contrast samples to be more easily investigated<sup>7,8</sup>. In de Sénarmont bias retardation, a type of DIC, light passes through a series of optics including a polarizer, quarter wave plate, two Nomarski prisms, and an analyzer in an effort to take advantage of the difference in velocity of perpendicular and parallel light as it travels through a specimen. Small differences in the index of refraction within a specimen cause variation in the recombination of light creating enhanced depth relief. In a de Sénarmont DIC configuration, the polarizer is adjustable to plus or minus 45°. It is important that the microscope is aligned for Köhler illumination (alignment protocol described in **Appendix A**)<sup>7-9</sup>. Unlike other contrast techniques such as phase, DIC has higher resolving power and does not exhibit a halo surrounding the targeted feature of interest. Although DIC causes depth relief, it is important to note that the relief is an artifact that is quite useful for contrast applications, but not representative of the true three-dimensional (3-D) character of a particular specimen<sup>7</sup>.

Wide-field fluorescence microscopy is a useful technique for imaging fluorescent specimens using a broad excitation source with a series of filters to excite fluorophores and collect the emitted photons along the same optical axis<sup>8</sup>. In the case of wide-field microscopy configurations, the objective also serves as an effective condenser allowing the high numerical aperture characteristics of the objective to increase optical resolution. Modern microscopes are usually configured with filter cubes containing an excitation filter (band-pass) to allow only a band of light from the broad excitation source to excite the fluorophore of interest, a dichroic mirror mounted at a 45° angle to the optical microscope, and a barrier emission filter (band-pass or long-pass) to collect only the corresponding fluorophore emission<sup>7,8</sup>. This convenient method for general fluorescence microscopy applications allows multiple fluorescent molecules to be probed by just utilizing an appropriate filter combination. The drawback of this technique is that the entire field of view is surveyed, which may pose a concern if the fluorophore of interest has a propensity for photo-bleaching or the specimen is sensitive to constant illumination for extended periods of time.

Laser scanning confocal microscopy (LSCM) is extremely useful technique for simultaneously imaging multiple fluorescent probes with overlapping spectral features or thick specimens<sup>9-11</sup>. The use of a pinhole to block light not in the focal plane of interest allows sharper imaging with precise z-resolution to be achieved<sup>9-11</sup>. The use of multiple lasers with multiple detecting channels allows single wavelength excitation for single fluorophore control, further eliminating artifacts contributed from fluorophores not in the spectral region of interest. The laser is scanned over a precise area of the sample, further reducing degradation from areas outside of the specific region of interest. The emission of fluorescent molecules is detected through a series of filters corresponding to specific wavelengths or spectrally through a series of PMTs. The technique of LSCM can be coupled to DIC and imaged via a transmitted light detector (TLD) for a transmission based image originating from the laser excitation source<sup>9</sup>. The use of TLD-DIC is particularly important for biological imaging and sample registration in regions that have not been fluorescently labeled.

## 1.4 Summary of Remaining Chapters

The use of targeted dye-labeling in conjunction with a variety of optical microscopy techniques will be utilized as a tool to probe environs in material and biomaterial microenvironments over the course of the next four chapters. **Chapter 2** will focus on the use of targeted fluorescence dyes in synthetic and naturally occurring microenvironments. In particular, the visualization of the sorting of ordered and disordered phases of lipid mixtures, the delivery, tracking, and controlled release of nanomaterial payloads in an intracellular environment, and the precise labeling of multi-component polymer microcapsules will be investigated. **Chapter 3** will explore, for the first time, solvent inclusions trapped within energetic crystals using a combination of LSCM and fluorescent dye-labeling. **Chapter 4** will investigate the use of Hall magnetometry to detect unlabeled target ssDNA on a device platform with correlated optical read-out from fluorescently labeled ssDNA conjugated superparamagnetic (SPM) beads. The fluorescent label provides a means to validate Hall detection and conduct optical based assays to evaluate the practicality of detection protocols for future point-of-care (POC) applications. The final chapter, **Chapter 5**, will use a fluorescently labeled MMPI to probe the real-time interactions with LNCaP-MT1-GFP expressing cells. The use of targeted dye-labeling coupled to optical microscopy

characterization techniques to investigate a host of interdisciplinary research will be shown to be a valuable asset in the pursuit of scientific discovery.

## CHAPTER 2

# IMAGING DISTINCT ENVIRONS IN SYNTHETIC AND NATURALLY OCCURRING MICROENVIRONMENTS

*Portions of this chapter have been previously published in the following articles:*

Yuan, J., Hira, S.M., Strouse, G.F., Hirst, L.S. Lipid bilayer discs and banded tubules:

Photoinduced lipid sorting in ternary mixtures. *Journal of the American Chemical Society***130**, 2067-2072 (2008).

Mason, B.P., Hira, S.M., Strouse, G.F. & McQuade, D.T. Microcapsules with three orthogonal reactive sites. *Organic Letters***11**, 1479-1482 (2009).

### 2.1 Introduction

Biological systems are perhaps the most ideal model for the presence of microenvironments surrounded by a much larger matrix. The simplest component of any living unit is a cell, which can be further broken down into smaller domains such as organelles<sup>12</sup>. The nucleus, cytoplasm, plasma membrane, mitochondria, golgi apparatus, endoplasmic reticulum, lysosomes, and even endosomes are examples of organelles within a larger more complete biological system that contain unique micron or sub-micron environments. In particular, these listed microenvironments are home to a host of functions including the replication and transcription of DNA, the regulation of proteins, ion mobility, and even small molecule recognition, signaling, and transport<sup>12</sup>. Attempts at further understanding these complex microenvironments and their nested processes down to differences in the spatial locations of single chemical functionalities may lead to a deeper understanding of lipid sorting, the capability of tracking nanomaterial cellular uptake, and the ability to create novel microcapsules for catalysis or drug delivery applications.

Examples of vesicles that contain distinctive microenvironments have been the interest of study in fields ranging from drug delivery to advanced material design. Creating artificial polymeric vesicles with unique microenvironments that can be optically interrogated may lead to significant advances in biomaterials for drug delivery. The experiments

described herein, probe the use of targeted dye labeling to monitor smaller environs contained within larger domains. Using strategically located dye molecules allows the visualization of lipid mixture sorting<sup>13</sup>, nanoparticle payload release, and reactive site labeling of polymer microcapsules<sup>14</sup>. Whether the vesicles are of natural (endosome) or synthetic in origin (polymer microcapsule), novel insights into the structure and function of these microenvironments can be investigated to gain a better understanding and achieve a global perspective.

Optical microscopy can provide a powerful tool to interrogate giant unilamellar vesicles (GUVs), which are a model system for how lipid content affects lipid phases. The synthetic GUV has been widely explored due to micron-scale domain formation and ease of investigation using microscopy<sup>15, 16</sup>. Membrane organization at the cellular level is an area of active research in molecular biology and biophysics<sup>17-20</sup>. The generation of lipid rafts has a variety of fascinating biological relevance and implications in endocytosis, cell adhesion, cell signaling, and ionic and molecular transport<sup>20-22</sup>. The synthetic study of the coexistence of multiple lipid phases and degrees of liquid immiscibility allow complex cellular environments to be minimized with the absence of proteins and other small molecules detracting from the source of the physical phenomenon<sup>21</sup>. Hollow lipid tubules have received recent attention because of striking similarities to GUVs with added geometric confinement in an effort to mimic transport channels, as well as, micro-reactors, and synthetic templates<sup>23, 24</sup>. By allowing the photo-oxidation of unsaturated lipids, it has been shown that chain reactions initiated by singlet oxygen can alter lipid morphology resulting in the presence of multiple liquid phases with varying domain size<sup>13, 22, 25</sup>. The photo-induced phase separation of lipid tubules formed from a ternary mixture can be probed as a model for new biological materials.

Nanomaterials are ideal candidates for nucleic acid or drug intracellular delivery and have gained interest over the last decade for the treatment of a variety of disease states<sup>26-31</sup>. Confocal microscopy of traceable bio-mimetic transport agents can allow insight into trans-membrane transport. Optical tracking of the delivery platform allows confirmation that the deliverable arrived at the intended destination. Nanomaterials based on quantum dots are of particular interest due to the favorable nanometer size regime for biological applications, broad excitation with narrow emission characteristics that shift with size for bar-coding multiple targets, large absorption cross-sections for two-photon tissue penetration, resistance to photobleaching, rapid ligand exchange for target functionalization, and ease of synthesis<sup>32-41</sup>. Although many compositions of quantum dots exist, quantum dots with InP cores are of

particular interest due to reduced toxicity concerns based on animal studies on larger InP (100-1000 nm)<sup>42, 43</sup>. The liposomal cellular uptake of water soluble InP/ZnS nanomaterials using a commercial transfecting agent, Optifect™, will be investigated for future applications of tracking biological processes and targeted drug delivery.

The release of molecular components from bio-mimetic transport agents can be followed using microscopy. Biological materials based on Au nanoparticles have been recently explored as molecular rulers<sup>44-48</sup>. The Au nanoparticle core provides a universal energy transfer acceptor for molecular dyes lower in energy than the surface plasmon resonance scattering transition of the metal nanoparticle. The quenching of fluorescence by nanometal surface energy transfer (NSET) follows an  $r^{-4}$  distance dependence and has been recently thoroughly characterized for a plethora of molecular dyes<sup>49</sup>. While the metal nanoparticle does not fluoresce, the fluorescence intensity quenching of molecular dyes in close proximity to the metal nanoparticle can provide a molecular beacon monitoring approach to track biological processes<sup>50-52</sup>. The implementation of a molecular beacon to investigate the DNA release off a Au nanoparticle platform will be investigated as an optical tool to monitor nanomaterial cellular delivery.

Polymeric microcapsules are synthetic candidates for drug delivery applications due to the ability to functionalize the outer shell and protect packages internally from outside environments<sup>53</sup>. Optical microscopy allows the cellular delivery of materials and subsequent intra-cellular response to be visualized. The syntheses of microcapsules have been around almost a century, but recent advancements on synthesis and functionalization have led to novel materials for catalysis and drug delivery applications<sup>14, 54-60</sup>. The use of layer-by-layer (LbL) microcapsule synthetic strategies has led to a variety of promising biological applications<sup>61</sup>. Although the LbL synthetic strategy results in tailored materials, high throughput synthesis may not be practical. Implementing a rapid synthetic approach based on emulsion templating methods, the copolymerization of multiple polymers in the formation of hollow microcapsules with three chemically specific reactive sites will be investigated for future applications in drug delivery.

## 2.2 Lipid Tubules

### 2.2.1 Lipid Tubule Preparation

Lipid tubules composed of 1,2-Dioleoyl-sn-glycero-3-phosphocholine (DOPC), (2S,3R,4E)-2-acylamino-octadec-4-ene-3-hydroxy-1-phosphocholine (egg sphingomyelin) (eSM), and cholesterol in a 1: 1: 1 mol % DOPC/ eSM/ cholesterol ratio were prepared by using flow assisted rehydration. Fluorescent dyes of 1,2-dipalmitoyl-sn-glycero-3-phosphoethanol-amine-N-(Lissaminerhodamine B sulfonyl) (ammonium salt) (Rh-DPPE) (Avanti Polar Lipids) and perylene (Fluka) were added to the lipid mixture at a final amount of 0.2 mol %. The lipid solution was dip-coated on a clean glass slide in the form of small droplets. The slide was dried under vacuum for 2 hours creating a lipid film. The lipids were re-hydrated with  $18.2 \text{ m}\Omega \text{ cm}^{-1}$  Milli-Q water or a 100mM sucrose solution. The sample were covered with a glass coverslip and sealed with vacuum grease. Optical microscopy characterization of samples was performed within 24 hours of sample preparation.

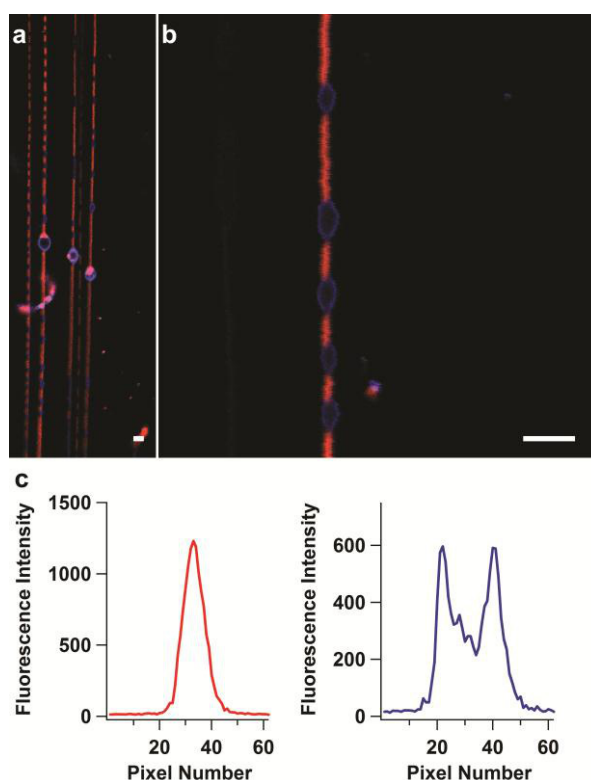


**Figure 2.1:** Photo-initiated lipid sorting into disordered (red) and ordered (blue) liquid phases (a,b). Line-scan analysis across (b) showing distinct morphological characteristics for disordered (left, red) and ordered (right, blue) phases (c). Scale bars =  $5 \mu\text{m}$ .

### 2.2.2 Microscopy Details

Laser Scanning Confocal Microscopy (LSCM) images of hollow lipid tubules were acquired with an inverted Nikon TE2000-E2 Eclipse C2Si spectral confocal microscope (Nikon Instruments Inc., Melville, NY, USA) equipped with a Nikon CFI Plan Apochromat TIRF 60X oil-immersion objective (NA 1.49, 0.12 mm WD). Simultaneous laser excitation from a 404 nm diode was used to excite perylene (emission filter: 450/35) and a 561 nm diode pumped solid-state laser was used to excite Rh-DPPE (emission filter: 605/75) using a 65.1  $\mu\text{m}$  pinhole. The data were analyzed using Nikon NIS Elements software.

### 2.2.3 Photoinduced Banded Lipid Tubules

The coexistence of liquid ordered ( $l_o$ ) and liquid disordered ( $l_d$ ) phases of ternary lipid tubule systems was investigated using confocal microscopy. Continuous and uniform lipid tubules containing Rh-DPPE and perylene were prepared and exposed to microscopy illumination for  $\sim 5$  seconds causing photo-oxidation of the unsaturated C-C bonds creating lipid peroxides. The photo-oxidation caused separation into two phases in the form of bands, where ordered phases were labeled by perylene and disordered phases were labeled by Rh-DPPE as shown in **Figure 2.1**. Once the phase separation is initiated, the native state can not be regenerated. Uniform lipid tubules spanning millimeter overall length scales are partially shown in **Figure 2.1a**. Upon closer inspection, the morphology of separation can be clearly identified into two distinct components:  $\sim 1$  micron wide with varying length disordered phases (red) and  $\sim 2 \times 4$  micron ordered bulges (blue) as shown in **Figure 2.1b**. A plot of fluorescence intensity versus distance depicts two types of morphological environments (**Figure 2.1c**). The ordered phase selectively stained with Rh-DPPE displays uniform intensity across the short axis of a tubule (red) while the perylene intensity is concentrated at the walls indicating a resolvable hollow tubule structure. The uniform Rh-DPPE intensity may be due to irresolvable tubule dimensions under the microscopy conditions utilized for these experiments. A plausible explanation for the bulges in only the ordered phases may be due to curvature restrictions in ordered phases where disordered phases can avoid curvature restrictions because of the inherent disorder as suggested by G. van Meer and W. L. Vaz<sup>62</sup>. The ability to synthetically generate photo-induced lipid sorting in tubule geometries may

lead to novel functional materials and insights on transporter channel properties and lipid raft function in cellular environments.

## **2.3 Nanomaterials**

### **2.3.1 Microscopy Details**

Laser Scanning Confocal Microscopy (LSCM) images of nanomaterials were acquired with an inverted Nikon TE2000-E2 Eclipse C2Si spectral confocal microscope (Nikon Instruments Inc., Melville, NY, USA) equipped with a Nikon CFI Plan Apochromat 40X objective (NA 0.95, 0.14 mm WD), condenser (NA 0.52), differential interference contrast (DIC), and a transmitted light detector. A 404 nm diode was used to excite Hoechst 34580 (emission filter: 450/35), a 488 nm argon ion laser was used to excite InP/ZnS mercaptoundecanoic acid (MUA) passivated quantum dots (emission filter: 515/30), and a 561 nm diode pumped solid-state laser was used to excite Alexa Fluor® 594 wheat germ agglutinin conjugate (emission filter: 605/75) using a 33.3  $\mu\text{m}$  pinhole. Spectral confocal (5 nm, resolution) was used to verify that the observed fluorescence was attributed to the spectral profile of InP/ZnS MUA quantum dots. Fluorescent microscopy was also carried out on an inverted Nikon TE2000-E2 Eclipse microscope (Nikon Instruments Inc.) equipped with a Nikon CFI Plan Apochromat 40x objective (NA 0.95, 0.14 mm WD). Wide-field imaging of NSET molecular beacon assays utilized an EXFO E-Cite illumination source, a FITC filter (Chroma, ex: 480/30, DCLP: 505, em: 535/40). Images were acquired on a Photometrics Coolsnap HQ<sub>2</sub> CCD camera. Bright-field overlays utilized DIC to observe the differences in the index of refraction of the samples and provide images of the cells. The data were analyzed using Nikon NIS Elements software.

### **2.3.2 Nanomaterial Cellular Imaging**

Nanomaterials can be used to track the delivery of biological materials into cells. The use of InP/ZnS core shell quantum dots are an ideal platform for the delivery of materials into cells due to the lack of evidence of toxic side effects commonly thought to be problematic in cadmium based materials<sup>42, 43</sup>. Core-shell InP/ZnS MUA passivated quantum dots with peak emission at ~560 nm were transfected into Chinese hamster ovary (CHO) cells at 30%

confluence grown in Dulbecco's modified eagle medium (DMEM) with non-essential amino acids using Optifect™ transfecting reagent, a cationic liposome. The role of the cationic liposome is to encapsulate the nanomaterial target to allow for cell mediated endocytosis. The transfection was accomplished using published protocols from the manufacturer in the absence of antibiotics. The uptake of quantum dots from the surrounding media and across the plasma membrane was investigated after 24 hours of incubation to determine if these materials are a viable candidate as an optically traceable material delivery platform.

The media containing the nanomaterials in Optifect™ was removed and replaced with a tris buffered saline (TBS) solution containing (5 µg/ mL of Alexa Fluor® 594 wheat germ agglutinin conjugate) as a live-cell membrane stain and allowed to react for 1 minute. The cell membrane stain was removed and washed twice with TBS and replaced with fresh media for imaging. The use of Alexa Fluor® 594 wheat germ agglutinin conjugate in live microscopy conditions is ideal for short term studies conducted immediately after staining (< 20 minutes). Initial labeling results in specificity for the plasma membrane. Although, over time the dye will be endocytosed and lead to Alexa Fluor® 594 based fluorescence artifacts located within the plasma membrane in addition to the cell surface.

The use of a 488 nm argon ion laser to excite the InP/ZnS quantum dots and overlay with the differential interference contrast (DIC) image acquired with a transmitted light detector (TLD) allows the nanomaterials to be visualized in relation to the CHO cells. The combination of quantum dot excitation with a 488 nm laser and Alexa Fluor® 594 wheat germ agglutinin conjugate excitation with a 561 nm diode pumped solid state laser allows the nanomaterial and the cell membrane to be clearly identified as shown in **Figure 2.2a-b**. Due to the quantum dot peak emission ~560 nm, the quantum dot signal bleeds into the red channel. The labeling of the cellular surface with spectrally different fluorescent dye is critical in determining whether biomaterials have transversed the plasma membrane or solely lie on the cellular surface. It is important to note, the use of a TLD detector to acquire transmission based images does not pass through a pinhole and therefore does not provide good depth resolution. To determine the location of the quantum dot package within the contents of a cellular environment a series of two-dimensional (2-D) images were acquired using a small pinhole (33.3 µm) and a step size of 0.250 µm along the z-axis. The series of discrete 2-D images were compiled and reconstructed to create a three-dimensional (3-D) image for analysis as shown in **Figure 2.2c**. The use of a maximum intensity projection within the Nikon NIS Elements software adjusted all signal acquired from a z-stack and adjuststo the highest pixel intensity. The 3-D compiled image was rotated 360° across

multiple directions to determine that the InP/ZnSMUA quantum dots are able to be clearly imaged encapsulated within an internal cellular environment, most likely endosomes, and not on the cellular surface.

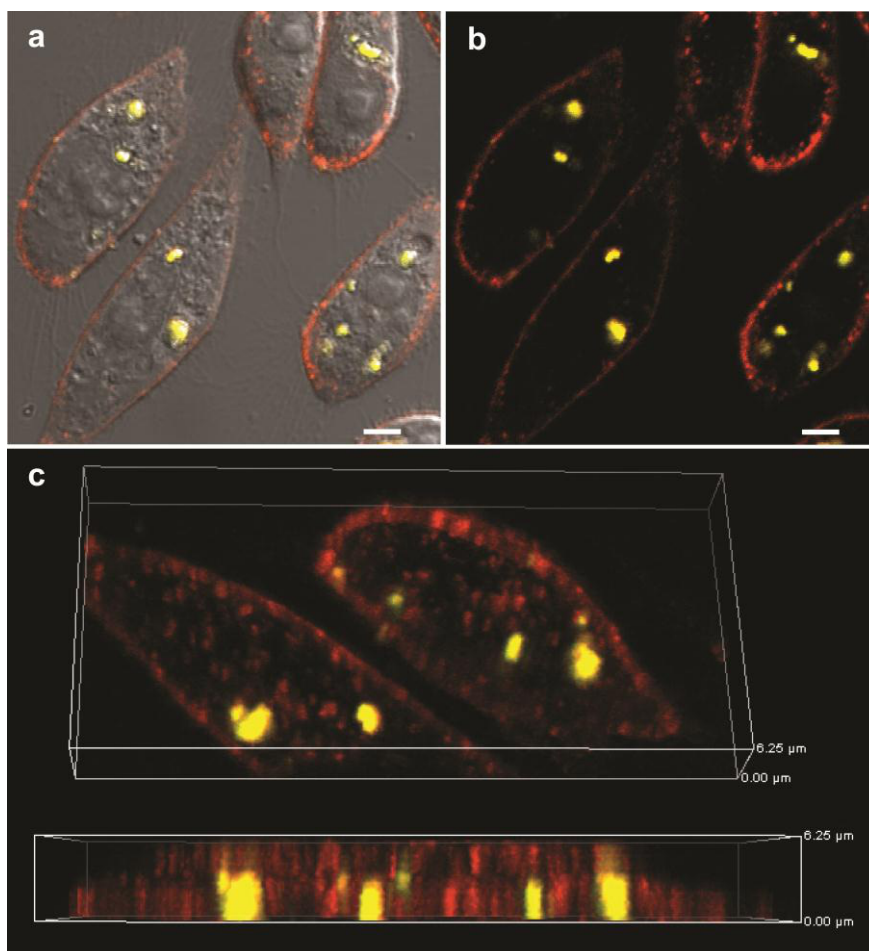


**Figure 2.2:** LSCM micrographs showing the cellular uptake of InP/ZnSMUA passivated quantum dots using Optifect™ 24 hours post transfection. **(a)** The TLD-DIC image overlaid with quantum dots (green) and cell membrane stain (red). **(b)** Quantum dot (green) and cell membrane (red) fluorescence overlaid image. **(c)** The 3-D reconstruction image of InP/ZnS quantum dots (green) and cell membrane stain (red) overlay. Scale bars = 5 μm.

More advanced nanomaterial microenvironment analysis can be achieved by staining additional cellular components, such as the nucleus. Although there are numerous DNA intercalators that selectively stain various grooves of DNA, Hoechst 34580 was specifically chosen based on the efficient excitation with a 404 nm diode laser excitation source resulting in predominantly blue emission and a 2-fold fluorescence enhancement upon minor groove adenine/thymine rich DNA intercalation. Cells were incubated with a TBS solution containing Hoechst 34580 (5 μg/ mL) for 30 minutes at 37 °C in a 5% CO<sub>2</sub> incubator. The

use of three lasers to selectively excite three separate dyes and obtain fluorescence signatures was utilized to monitor the uptake of InP/ZnSMUA coated quantum dots as shown in **Figure 2.3a-b**. The 3-D reconstruction of the cell and encased nanomaterial is shown in **Figure 2.3c**. Applying an alpha blending projection within the Nikon NIS Elements software takes into account nearest neighbor pixel intensity to determine the particular 3-D pixel intensity. Alpha blending is particularly useful for representing surface features. The localization of the selectively transfected quantum dots (green) is clearly shown contained within the plasma membrane (red) and not in the nucleus (blue). The static 3-D reconstructed image shown in Figure 2.3c allows the internalization to be clearly identified within 24 hours of liposomal incubation and holds promise for applications of stable, optically traceable delivery platform to cellular microenvironments.

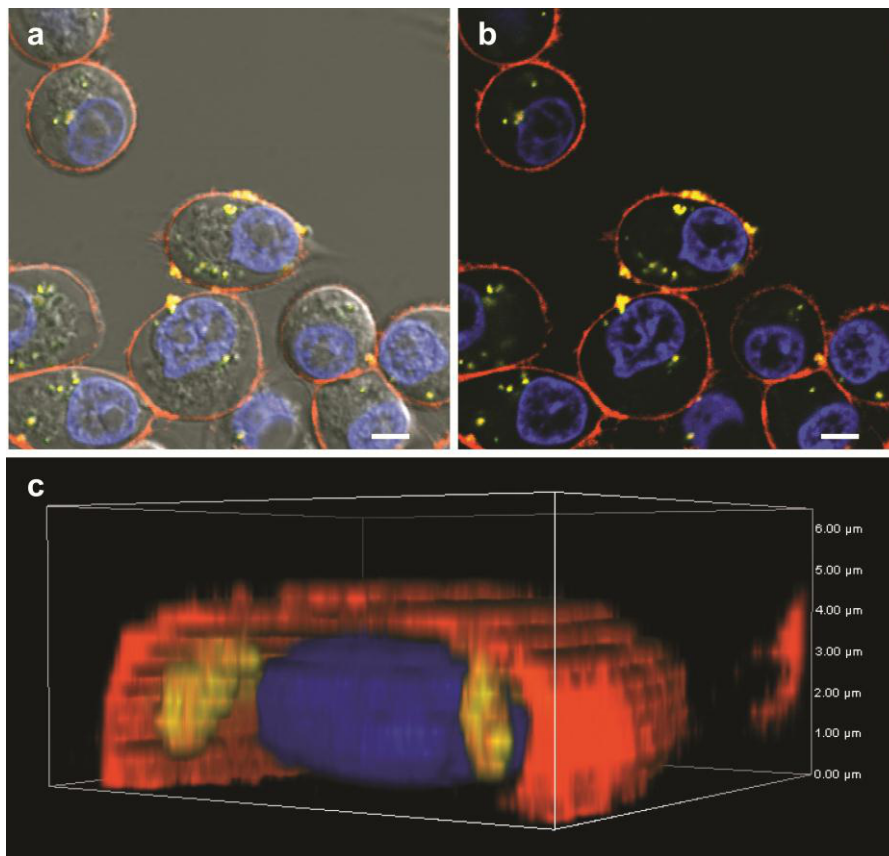


**Figure 2.3:** LSCM micrographs showing the cellular uptake of InP/ZnSMUA passivated quantum dots using Optifect™ 24 hours post transfection. (a) The TL-DIC image overlaid with nucleus (blue), quantum dots (green), and cell membrane stain (red). (b) Nucleus (blue), quantum dot (green), and cell membrane (red) fluorescence overlaid image. (c) The triply stained 3-D reconstruction image of InP/ZnS quantum dots (green) and cell membrane stain (red) overlay. Scale bars = 5 μm.

### 2.3.3 NSET Molecular Beacon Assay and Nanomaterial Cellular Transfer

The release of DNA off a nanomaterial platform was investigated using a NSET based molecular beacon strategy. The proximity based energy transfer assay has been well characterized for the fluorescence quenching of a series of molecular dyes by Au nanoparticles<sup>49</sup>. Although previously published studies utilized 1.5-2.0 nm Au nanoparticles, larger 5.7 nm Au also can be used to quench molecular dye emission with slightly modified distant dependent quenching efficiencies. The assay consisted of utilizing a 5.7 nm Au nanoparticle to efficiently quench the emission of Alexa Fluor® 488 covalently attached to DNA. The sequences of double-stranded DNA (dsDNA) appended to 5.7 nm Au were purchased commercially from Midland Certified Reagent Company Inc. are 5'- /SHC<sub>6</sub>-GCT GAT GAC TAT CGA ATT CGG TAG TAG GCG-3' and 5'- /AF488C<sub>6</sub>-CGC CTA CTACCGAATTCG ATA GTCATC AGC-3'. Optifect™ was used as to transfect CHO cells in DMEM with non essential amino acids at 30% confluence with the DNA labeled Au nanoparticles analogous to section 2.3.1. The real-time, live-cell Alexa Fluor® 488 labeled DNA release was detected as an increase in fluorescence intensity with time. The gradual DNA release off the nanoparticle surface was observed using wide-field fluorescence microscopy within 1 hr post transfection as shown in **Figure 2.4**. Micrographs were acquired at 1, 2, 4, 6, and 12 hours were taken in the same general area of the imaging dish and show signs of cellular degradation (not shown). The 24 hour time point shows cell elongation indicative of healthy growth suggesting that 800 μs exposure times over extended periods of time causes photo-initiated damage. The nanomaterial transfection and subsequent DNA release was observed to occur within one hour of material transfection. No fluorescence intensity was observed over the timescale of the experiment for cationic liposomes prepared with DNA conjugated nanoparticles in the absence of cells (not shown). Since a transfecting agent was used, the nanomaterial was taken up by cells through endocytotic pathway resulting in punctate packages. The transformation from early to late endosomes involves a drop in pH and increased levels of glutathione, which is believed to facilitate thiol-based ligand release as shown by Rotello et al<sup>51</sup>. Diffuse fluorescence was also observed in the vicinity of endosomal packages suggesting DNA escape. Large packages of Au can be seen over the time course suggesting aggregation of the Au nanoparticle following surface passivated DNA release and subsequent endosomal re-packaging of the nanomaterials over time due to an osmotic pressure induced perturbation of the endosomal package. Cells that

were transfected while undergoing mitosis were observed to transfer endosomal packages to newly formed daughter cells as shown in **Figure 2.5**. This observation has implications on dosing levels, where cells may be exposed to transfected nanomaterials for extended periods of time through the slow release of DNA from the surface of the nanomaterial following package transfer to daughter cells. Further, more extensive studies are currently underway.

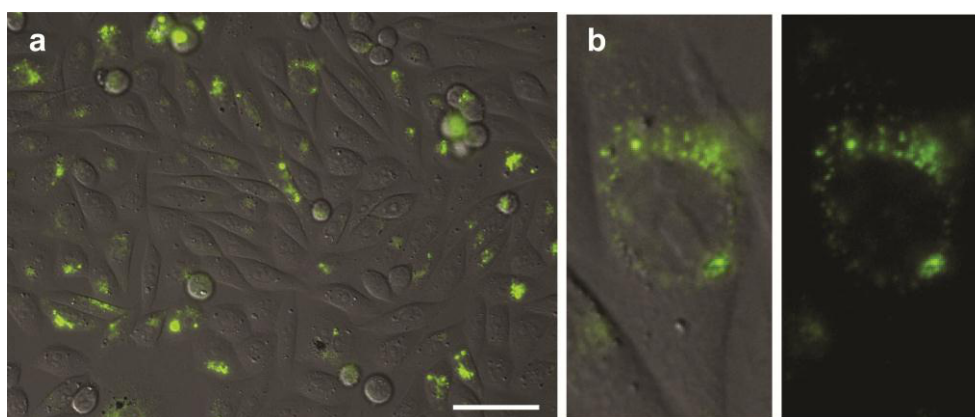


**Figure 2.4:** Wide-field fluorescence micrographs showing the cellular uptake of 5.7 nm Au nanoparticles passivated with fluorescein labeled dsDNA using Optifect™ 24 hours post transfection. **(a)** The DIC image overlaid with fluorescein fluorescence (green) indicating ligand release. **(b)** A zoomed in region of **(a)** depicting fluorescein fluorescence (green) with DIC overlay and fluorescein fluorescence only (green) showing DNA release (punctate) and endosomal escape (diffuse). Scale bar = 50  $\mu\text{m}$ .

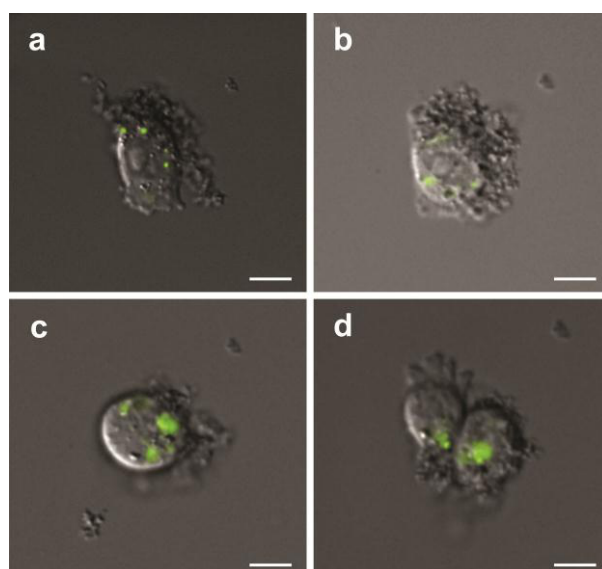


**Figure 2.5:** Wide-field fluorescence with DIC overlaid micrographs showing cellular division and the transfer of DNA released off nanoparticle platform (green) to newly formed daughter cells at 1 hr **(a)**, 2 hr **(b)**, 4 hr **(c)** and 6 hr **(d)**. Scale bars = 10  $\mu\text{m}$ .

## 2.4 Synthetic Polymeric Microcapsule

### 2.4.1 Polymer Microcapsule Formation

Highly cross-linked polymer microcapsules containing a polyureabase structure were synthesized via a copolymerization of polymethylenepolyphenylisocyanate (PMPPI) and tetraethylenepentamine (TEPA) in a chloroform and water emulsion. Encapsulating polychloromethylstyrene (pCMS) and/or polyazidomethylstyrene (pAMS) during the synthetic process yields a polymer microcapsule with reactive amine functionalities on the shell and reactive chloromethyl and azidomethyl functionalities encased within the capsule walls. To ensure that all of the isocyanates were converted to amines, N,N-dimethylaminopyridine (DMAP) was added. By varying the degree of agitation during the polymer polymerization, different sized microcapsules can be produced. The amine loading on the capsule shell was determined to be 0.04 mmol/g amine by treatment with trifluoroacetic acid anhydride and subsequent elemental analysis. The general synthetic strategy employed for polymer microcapsule formation is shown in **Figure 2.6**.

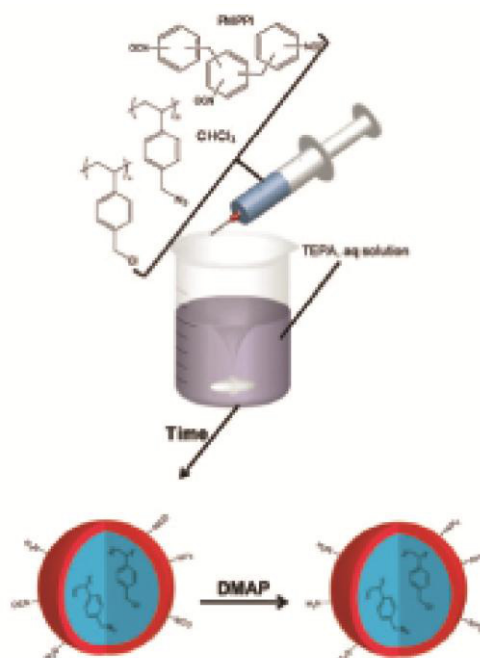


**Figure 2.6:** Pictorial representation of the synthesis of polyurea based polymer microcapsules. Taken from Mason, B.P., Hira, S.M., Strouse, G.F., McQuade, D.T. *Organic Letters* **11**, 1479-1482 (2009) – Reproduced with permission by the American Chemical Society.

The three reactive dyes chosen to react with three chemically reactive moieties were cascade blue hydrazide™ (Invitrogen), Lissamine rhodamine B sulfonyl chloride (Invitrogen), and fluorescein isothiocyanate (FITC) acetylene with a small amount of catalytic copper. The use of a Huisgen cycloaddition as a ‘click’ reagent labeling strategy allows precise and reliable targeted functionalization used for biological applications<sup>63-65</sup>. The FITC acetylene was synthesized by reacting FITC with propargyl amine in THF<sup>66</sup>. Reaction completion was verified by thin layer chromatography (TLC) and the structure was verified using NMR (**Appendix B**).

### 2.4.2 Microscopy Details

Laser Scanning Confocal Microscopy (LSCM) images of microcapsules were acquired with an inverted Nikon TE2000-E2 Eclipse C2Si spectral confocal microscope (Nikon Instruments Inc., Melville, NY, USA) equipped with a Nikon CFI Plan Apochromat 40X objective (NA 0.95, 0.14 mm WD), condenser (NA 0.52), differential interference contrast (DIC), and a transmitted light detector. A 404 nm diode was used to excite Cascade Blue™ or Hoechst 34580 (emission filter: 450/35), a 488 nm argon ion laser was used to excite FITC acetylene or acridine yellow (emission filter: 515/30), and a 561 nm diode pumped solid-state laser was used to excite Lissaminerrhodamine B or Alexa Fluor® 594 wheat germ agglutinin conjugate (emission filter: 605/75) using a 33.3 μm pinhole. The data were analyzed using Nikon NIS Elements software.

### 2.4.3 Polymer Microcapsule Labeling

The fluorescent labeling of pCMS encased polymer microcapsules was investigated using confocal microscopy. The successful labeling of free amines localized on the outer shell of microcapsules with Lissamine rhodamine B (red) is shown in **Figure 2.7a** as an overlay with transmitted DIC. The absence of Lissamine rhodamine B emission at the center of the hollow microcapsule illustrates the chemical specificity of labeling. Differences in the inner polymer morphology contained on the inside of the microcapsule compared to the outer shell can be visualized. A series of distinct 2-D images were reconstructed and projected in 3-D to visualize the hollow nature of these microcapsules (**Figure 2.7b-c**). The step-size

between 2-D images in **Figure 2.7b-c** was intentionally kept larger (1  $\mu\text{m}$ ) than the available z-resolution to create a series of rings to provide additional perception of depth of field.

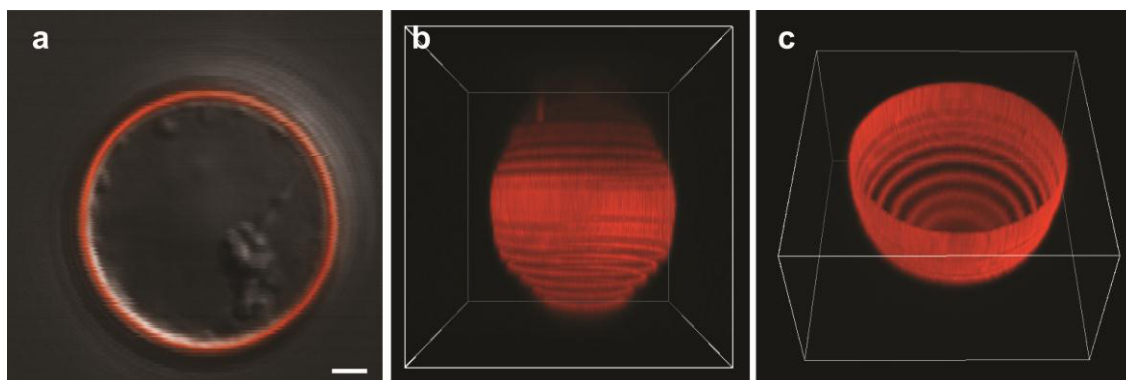


**Figure 2.7:** LSCM micrographs showing the selective labeling of Lissamine rhodamine B on the outer shell of polyurea microcapsules with encased pCMS. **(a)** The TLD-DIC image overlaid with selective microcapsule shell labeling (red). **(b-c)** The 3-D reconstruction of the polymer shell fluorescent labeling (red) from two different perspectives. Scale bar = 2  $\mu\text{m}$ .

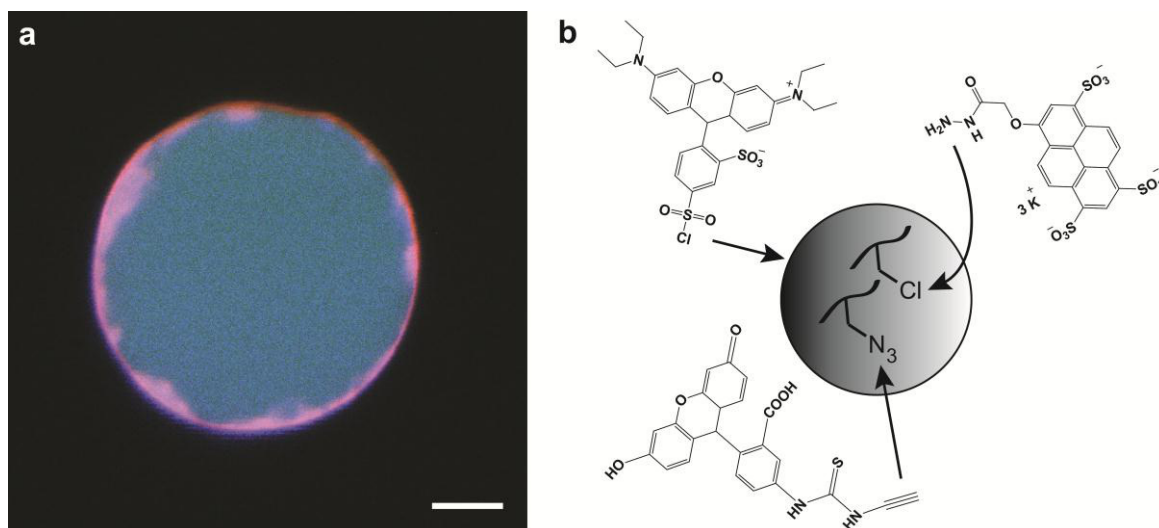


**Figure 2.8:** The TLD-DIC overlay showing selective labeling of the interior (blue and green) and the shell (red) **(a)**. Strategy for selective microcapsule labeling with three reactive fluorescent dyes **(b)**. Scale bar = 5  $\mu\text{m}$ . Adapted from Mason, B.P., Hira, S.M., Strouse, G.F., McQuade, D.T. *Organic Letters* **11**, 1479-1482 (2009).

#### 2.4.4 Triply Labeled polymer Microcapsules

Simultaneous labeling of all three reactive sites contained on or within the polymer microcapsule was accomplished by adding all three reactive fluorescent dyes in a 1: 1: 1 ratio in THF with a catalytic amount of copper and rocked overnight as shown in **Figure 2.8**. The

microcapsules were washed with DMF until the supernatant was free of unlabeled fluorescent dye. Additional washes of water, methanol, THF, and diethyl ether were performed and the product was dried under vacuum. Simultaneous characterizations of all three fluorescent dyes, along with the DIC overlay, are also shown.

Closer inspection of microcapsule morphology can be evaluated by plotting the corresponding fluorescence intensity as a function of distance across a microcapsule. Evidence of labeling specificity solely by chemical functionality is shown in **Figure 2.9**. The cascade blue and fluorescein molecular dyes uniformly labeled the core, while Lissamine rhodamine B predominately labeled the shell wall resulting in increased intensity over the capsule shell. The slight amount of cascade blue shell labeling may be due to polymer emission from the use of a violet, 404 nm, laser source. Further evidence of molecular specificity can be seen by generating a 3-D reconstruction of the microcapsule and displaying half the data. The individual components (blue, green, and red) are shown separately and in combination for clarity in **Figure 2.10a-e**. Precise morphological defects in the form of crenation can be clearly seen in the 3-D reconstructed image. The absence of non-specific chemical labeling outside of the targeted region of interest shows a high level of capsule control, a characteristic needed for complex biological applications.

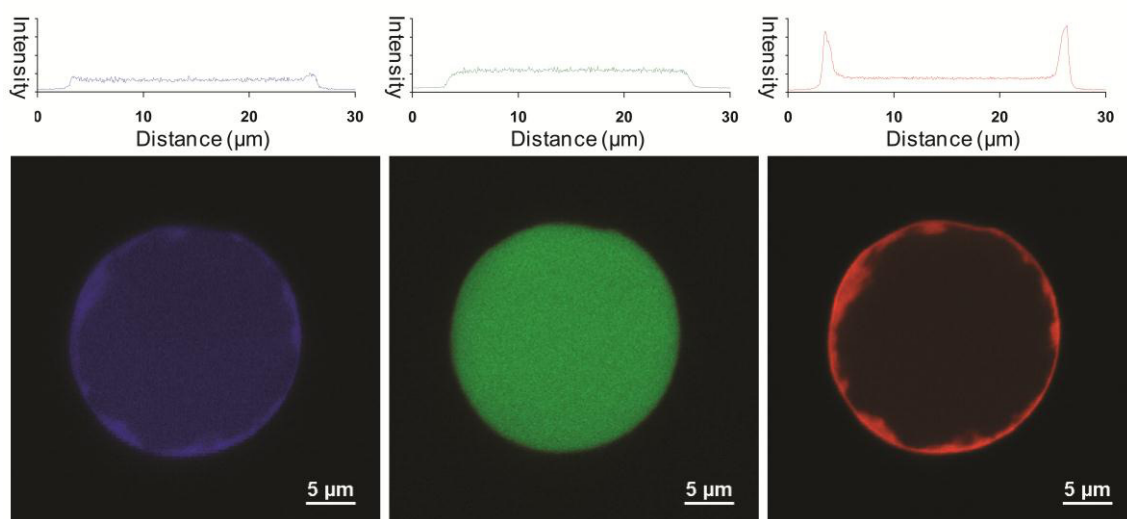


**Figure 2.9:** The selective simultaneous labeling of three spatially separated reactive sites on polyurea microcapsules using cascade blue hydrazide<sup>TM</sup> (blue), FITC acetylene (green), and Lissamine rhodamine B (red). Line-scan analysis for each image is shown as a plot of intensity with respect to distance across the microcapsule for each individual image. Scale bars = 5  $\mu\text{m}$ . Adapted from Mason, B.P., Hira, S.M., Strouse, G.F., McQuade, D.T. *Organic Letters* **11**, 1479-1482 (2009) – Reproduced with permission by the American Chemical Society.

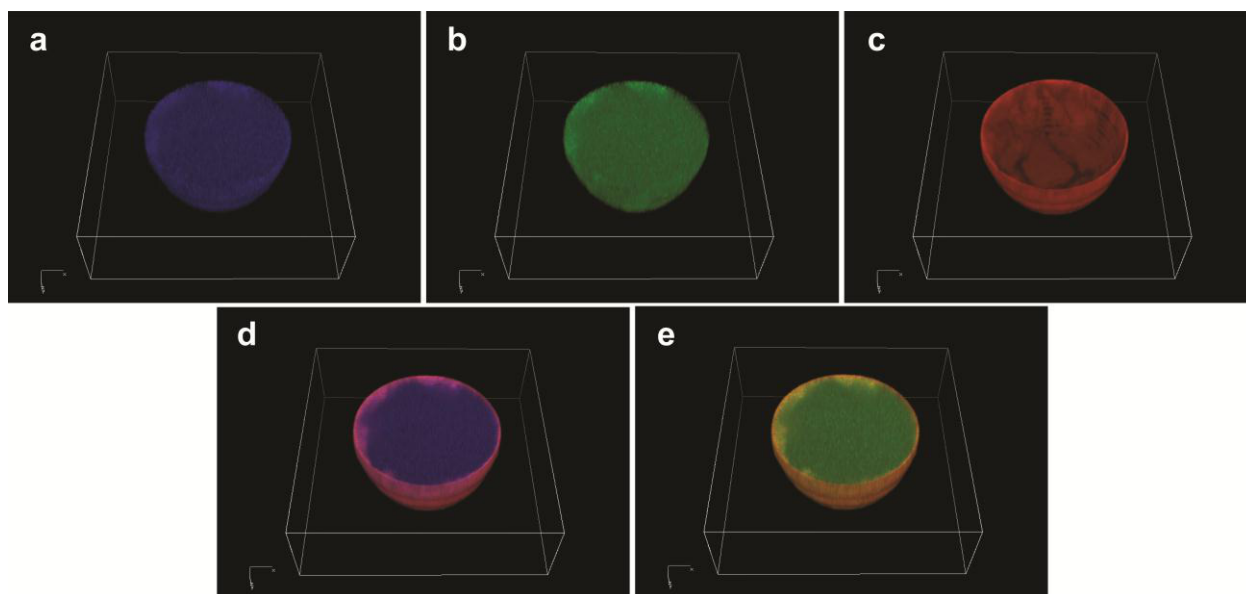


**Figure 2.10:** The 3-D reconstruction images of microcapsules showing the color coordinated morphologies for cascade blue hydrazide™ (blue), fluorescein acetylene (green), and Lissamine rhodamine B (red). Overlays of cascade blue hydrazide™ (blue) with Lissamine rhodamine B (red) and FITC acetylene with Lissamine rhodamine B (red) are shown for clarity. Adapted from Mason, B.P., Hira, S.M., Strouse, G.F., McQuade, D.T. *Organic Letters* **11**, 1479-1482 (2009).

### 2.4.5 Cellular Uptake of Microcapsules into Chinese Hamster Ovary Cells

The application of these multifunctional microcapsules with multiple reactive sites into biological systems may allow for a delivery platform with tailored characteristics for precise biological applications. One could imagine modifying these capsules by loading multiple drugs or genetic materials enclosed within the capsule walls, while leaving the outside native or appending biologically friendly delivery based agents on the outside of the capsule such as cell penetrating peptides (CPPs) or aptamers<sup>67, 68</sup>. Experiments described are preliminary, but focused exclusively on whether a package of considerable size can be endocytosed by mammalian cells.

Chinese hamster ovary (CHO) cells were utilized for experiments, due in part to their robustness and accessibility, to determine if microcapsules can transfect across the plasma membrane. Microcapsules were internally functionalized with acridine yellow by previously reacting one of the available amines with chloromethyl polystyrene, while the outside microcapsule shell was maintained in its native state with available reactive amine functionalities (**Figure 2.11a**). CHO cells at 30% confluence were incubated with acridine

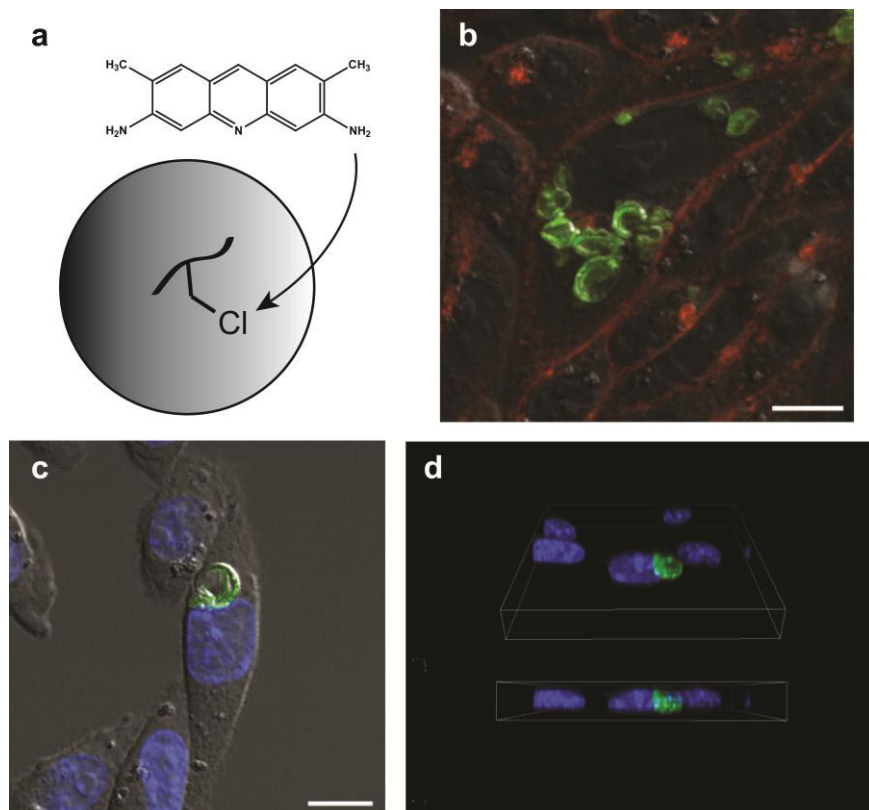


**Figure 2.11:** Pictorial reaction labeling of acridine yellow with pCMS encased within polyurea microcapsules (a). LSCM micrographs showing the cellular uptake of acridine yellow microcapsules (green) into CHO cells with a cell membrane stain (red) (b). LSCM micrograph of acridine yellow (green) microcapsules in CHO cell overlaid with a nuclear stain (blue) (c). The 3-D reconstruction image of acridine microcapsule (green) and nuclear stain (blue) showing definitive cellular uptake (d). Scale bars = 5  $\mu\text{m}$ .

yellow functionalized microcapsules for 24 hours. Microscopy analysis shows uptake across the plasma membrane and into the cytoplasm (**Figure 2.11b**). Due to the excessive micron scale size, the microcapsules settle out of solution over time so precise quantification of uptake was not possible. Those capsules that settle out near cells have the opportunity to be taken into cells via an endocytotic pathway, most likely macro-pinocytosis because of the large size of the packages. Other known cellular uptake mechanisms such as clatherin or caveola-mediated endocytosis are not within the same size regime as the micron-sized polymer capsules. Both cell nuclei staining using Hoechst 34580 and a plasma membrane stain, Alexa Fluor® 594 wheat germ agglutinin were utilized to ensure that the microcapsules were located within the plasma membrane and not solely on the cell surface. In addition, z-stack imaging was performed to reconstruct the material-cell interface in a 3-D fashion to determine the precise location of the materials in a similar fashion described in section 2.3(**Figure 2.11bc**). Many microcapsules were washed away indicating that many did not get

endocytosed, but those leftover were located within the plasma membrane as shown in **Figure 2.11b-c**. The 3-D reconstruction shown in **Figure 2.11d** clearly shows the presence of the acridine yellow stained microcapsule within the plasma membrane and along the nuclear envelope. Due to the massive size, the nucleus appears to be slightly deformed in shape at the point of contact between the microcapsule and the nuclear envelope. Acridine compounds have been shown to intercalate into the structure of DNA<sup>69</sup>. These preliminary results suggest that large microcapsules (> 1 $\mu$ m) can be taken up by CHO cells without initially releasing its contents. It is evident from **Figure 2.11** that although the microcapsules are not fully swelled and appear to have significant shape deformation, the exterior microcapsule walls are still intact.

## 2.5 Conclusions and Future Directions

The use of targeted dye labeling in conjunction with optical microscopy based characterization methods has allowed small environs to be probed within much larger domains. Whether fluorescent dyes partitioned to ordered and disordered phases of lipid tubules, nanomaterials encased within CHO cells, or synthetic polymer microcapsules containing three orthogonal reactive sites, the micron and sub-micron environs can be selectively probed within larger domains using targeted dye labeling. The extraordinary specificity of fluorescent molecular dyes and quantum dots to selectively probe environs containing differences in single chemical functionalities has the potential to compliment and in specific cases enhance the precise interrogation of microenvironments.

## CHAPTER 3

### PROBING SOLVENT INCLUSIONS IN ENERGETIC CRYSTALS USING TARGETED DYE LABELING

*Portions of this chapter have been previously published in the following article:*

Roberts, C.W., Hira, S.M., Mason, B.P., Strouse, G.F. & Stoltz, C.A. Controlling RDX explosive crystallite morphology and inclusion content via simple ultrasonic agitation and solvent evaporation. *CrystEngComm* **13**, 1074-1076 (2011).

#### 3.1 Introduction

Organic energetic materials based on cyclotrimethylene trinitramine, commonly known as RDX, have been widely used as a major component in many explosive material formulations including Composition B (60% RDX/40% trinitrotoluene (TNT)), C4 (91% RDX/9% polyisobutylene), and A5 (99% RDX/1% stearic acid)<sup>70</sup>. The application of RDX as a commonly used explosive is due in part to its favorable density for subsequent detonation velocity and detonation pressure, but its energetic properties are affected by the quality of crystalline structure<sup>70, 71</sup>. Recent research has targeted a series of reduced sensitive versions of RDX for their dominant role in military applications involving insensitive munitions (IM) for reasons of unintentional detonation in storage, handling, or transportation<sup>72</sup>. Combining formulations of RDX with an insensitive surrounding matrix in the form of plastic-bonded explosives (PBX) has been shown to decrease shock instability over native RDX providing a safer energetic compound<sup>72-74</sup>. A number of hypotheses centered on the source of material instability have been proposed, where the major culprits include internal crystal defects, surface crystal defects, and particle morphology<sup>72, 73, 75-77</sup>. Defects, whether of internal or surface in origin, can be the source of ‘hot spots’ during initiation, drastically changing the material properties<sup>75, 78-81</sup>. Although the reasons for the reduced shock sensitivity are debatable, it has been recently shown using small angle neutron scattering (SANS) that there is a correlation between PBX shock sensitivity and RDX void content<sup>82</sup>.

Probing structural defects (both surface and internal) in energetic crystals has been traditionally accomplished using a blend of microscopy-based characterization for qualitative analysis and complementary mechanical characterization for quantitative analysis. Microscopy techniques have focused on bright-field microscopy, confocal laser scanning microscopy, scanning electron microscopy (SEM), atomic force microscopy (AFM), SANS, and X-ray diffraction<sup>70</sup>. All of these methods have their advantage and disadvantages depending on the type of defect and the location of the defect. Although SANS and X-ray diffraction provide unique chemical information about the uniformity of atoms in a crystal lattice, high throughput characterization is not feasible and access to such sophisticated techniques are limited.

The ability to control the amount and location of defects in RDX during the crystallization process is a major concern. Even though the commercial manufacturing of reduced sensitivity grades of RDX tends to be proprietary, there have been attempts at controlling the particle quality, size, morphology, and inclusion content<sup>83-85</sup>. Studies focused on altering cooling rates, use of anti-solvents, and the use of sonication during the recrystallization process have been explored<sup>86</sup>. Traditional methods controlling the rate of solvent evaporation or cooling, concomitant with mechanical stirring or agitation of solvent, leads to a variety of solvent dependent morphologies. Due to the high supersaturation levels of RDX used under these methods, a large size distribution results from high nucleation and growth rates. At low saturation levels, variable nucleation leads to irreproducible results. The use of sonocrystallization to control the crystallization process may provide a way to induce nucleation at low saturation levels and obtain uniform RDX crystals. More precisely, the use of ultrasound during the recrystallization causes cavitations in the mother solution where small voids are formed and violently collapsed<sup>84</sup>. The cavitations generate localized areas of supersaturation levels of RDX where nucleation can take place without being at supersaturation levels throughout the entire volume of solvent. The use of sonocrystallization in conjunction with tuning the solvent evaporative rates has the potential to improve the quality of RDX.

The novel use of fluorescent dyes to probe micron and submicron defects during the recrystallization process of energetic crystals has the potential to eliminate many of the drawbacks of traditional methods utilized to characterize internal voids while allowing convenient and rapid characterization. In particular, an additional benefit of using a fluorescence based characteristic technique allows the sample to be interrogated without the need to match sample refractive index for background contrast and allow the best resolution

for optical based techniques by ultimately tuning the both the excitation source and the dye emission towards the violet and blue, respectively. The experiments described herein probe the crystal morphology and internal inclusion content using microscopy based techniques of RDX samples prepared using conventional and sonocrystallization strategies<sup>87</sup>.

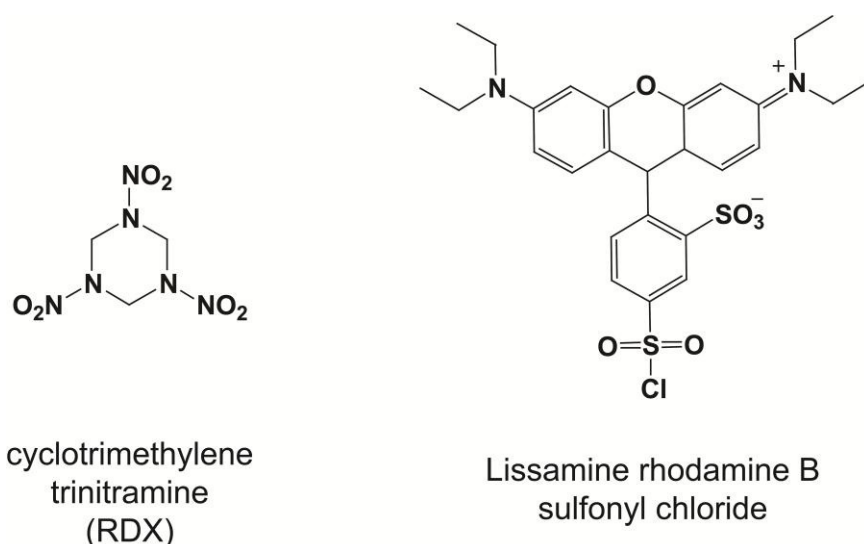


**Figure 3.1:** The chemical structures for cyclotrimethylene trinitramine, known commonly as RDX, (left) and Lissamine rhodamine B sulfonyl chloride (right).

### 3.2 RDX Recrystallization

Samples of RDX were recrystallized by first dissolving in solvent (acetone or dimethylformamide) or solvent with 1.3% by mass Lissamine rhodamine B sulfonyl chloride and allowed to evaporate at 40 °C. The chemical structures of RDX and Lissamine rhodamine B sulfonyl chloride are shown in **Figure 3.1**. Solvent evaporation was controlled by adjusting the size of the opening of the crystallization container to the outside ambient environment. Agitation of the mother solution was conducted using either sonication using an ultrasonic bath at a frequency of 40 KHz or mechanical stirring at a rate of 775 rpm. Samples were stored as a solid in the absence of light until microscopy characterization was performed.

### 3.3 Microscopy Details

Optical microscopy characterization using matching index of refraction was carried out on a Nikon SMZ 1500 stereomicroscope with a magnification of 11.25X and aniline ( $n_D^{20}$  1.586) as a refractive index matching fluid. Laser Scanning Confocal Microscopy (LSCM) images of RDX crystals deposited onto a glass coverslip were acquired with an inverted Nikon TE2000-E2 Eclipse C2Si spectral confocal microscope (Nikon Instruments Inc., Melville, NY, USA) equipped with a Nikon CFI Plan Apochromat 40X objective (NA 0.95, 0.14 mm WD), condenser (NA 0.52), differential interference contrast (DIC), and a transmitted light detector. A 561 nm diode pumped solid-state laser was used to excite Lissamine rhodamine B sulfonyl chloride (emission filter: 605/75) using a 33.3  $\mu\text{m}$  pinhole. Spectral confocal (5 nm, resolution) was used to verify that the observed fluorescence was attributed to the spectral profile of Lissamine rhodamine B sulfonyl chloride. Wide-field imaging of the RDX crystals utilized an EXFO X-Cite illumination source at 50% power and a TRITC filter (Chroma, ex: 540/25, DCLP: 565, em: 620/60). Images were acquired on a Photometrics Coolsnap HQ<sub>2</sub> CCD camera. Bright-field overlays utilized differential interference contrast (DIC) to observe the differences in the index of refraction of the samples. The data were analyzed using Nikon NIS Elements software.

### 3.4 Microscopy Analysis of RDX

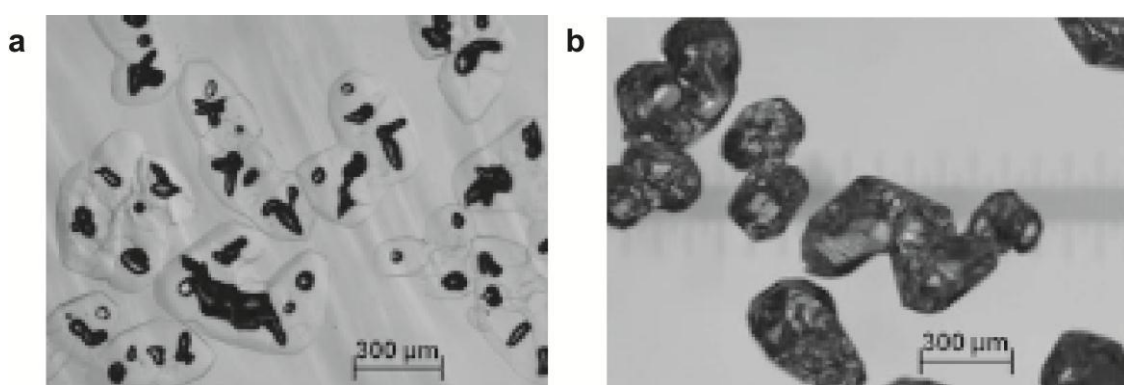


**Figure 3.2:** Optical micrographs of RDX crystals with matching index of refraction fluid (**a**) and without matching index of refraction fluid (**b**) showing the presence of internal defects. Adapted from Roberts, C.W., Hira, S.M., Mason, B.P., Strouse, G.F. & Stoltz, C.A., *CrystEngComm*, 13, 1074-1076, 2011 – Reproduced by permission of the Royal Society of Chemistry.

Internal voids stemming from solvent defects have been traditionally characterized using optical microscopy with matching refractive index. In order to visualize internal solvent defects in RDX, the crystals are immersed in aniline ( $n_D^{20}$  1.586) to match the refractive index of the surrounding crystal and allow the inclusions to be distinguished. A comparison of RDX crystals using optical microscopy with and without matching refractive index fluid can be seen in **Figure 3.2**. Although large inclusions can be easily observed in **Figure 2b**, the presence of small defects is not resolvable. The other major drawback of this technique is that different energetic materials need different fluids to appropriately match the correct refractive index for each material. This limitation renders formulation analysis inefficient due to the inability to conduct high throughput microscopic analysis on multiple types of energetic materials.

Incorporating fluorescently labeled dye molecules into the solvent required for crystallization allows crystalline defects from trapped solvent inclusions to be identified. The ability to acquire measurable signal in the absence of substantial background is a desirable attribute for material characterization that is inherent in fluorescence based techniques. As shown in **Figure 3.3**, RDX crystals can be visualized using a combination of bright-field illumination with DIC and wide-field fluorescence microscopy. The RDX crystal morphology can be observed in the DIC channel, while the presence of solvent defects can be observed through a TRITC filter without the need for a matching index of refractive fluid since the solvent defects will photoluminescence at wavelengths distinct to the fluorophore. The optical resolution,  $r$ , of objects within an image can be theoretically calculated using the following equation:

$$r = \frac{(1.22 \times \lambda)}{(NA_{objective} + NA_{condenser})}, \quad (3.1)$$

where  $\lambda$  is the wavelength of light and  $NA$  is the numerical aperture. The bright-field image shown in **Figure 3.3** has a theoretical resolution limit of 978 nm using 550 nm for  $\lambda$  (mean wavelength of a tungsten-halogen light source) and a  $NA$  aperture of 0.95 and 0.52 for the objective and condenser, respectively. In wide-field and other fluorescence techniques in which the objective serves as both the excitation transmitter and collector a higher the optical resolution,  $r$ , of objects within an image can be calculated using the following equation:

$$r = \frac{(1.22 \times \lambda)}{(NA_{objective} + NA_{condenser})}, \quad (3.2)$$

where the  $NA$  of the objective is solely used. The wide-field fluorescence image shown in **Figure 3.3** has a theoretical resolution limit of 360 nm, where the  $\lambda$  used to excite Lissamine

rhodamine B sulfonyl chloride sulfonyl chloride was 540 nm. The advantage of utilizing fluorescence based optical techniques over bright-field clearly allows for higher resolution data to be realized. A closer inspection of **Figure 3.3b-c** shows that fluorescence based techniques can achieve higher resolution, but scattering artifacts from the broad wavelength excitation source used under wide-field conditions and the crystal face make in-depth analysis of defects difficult.

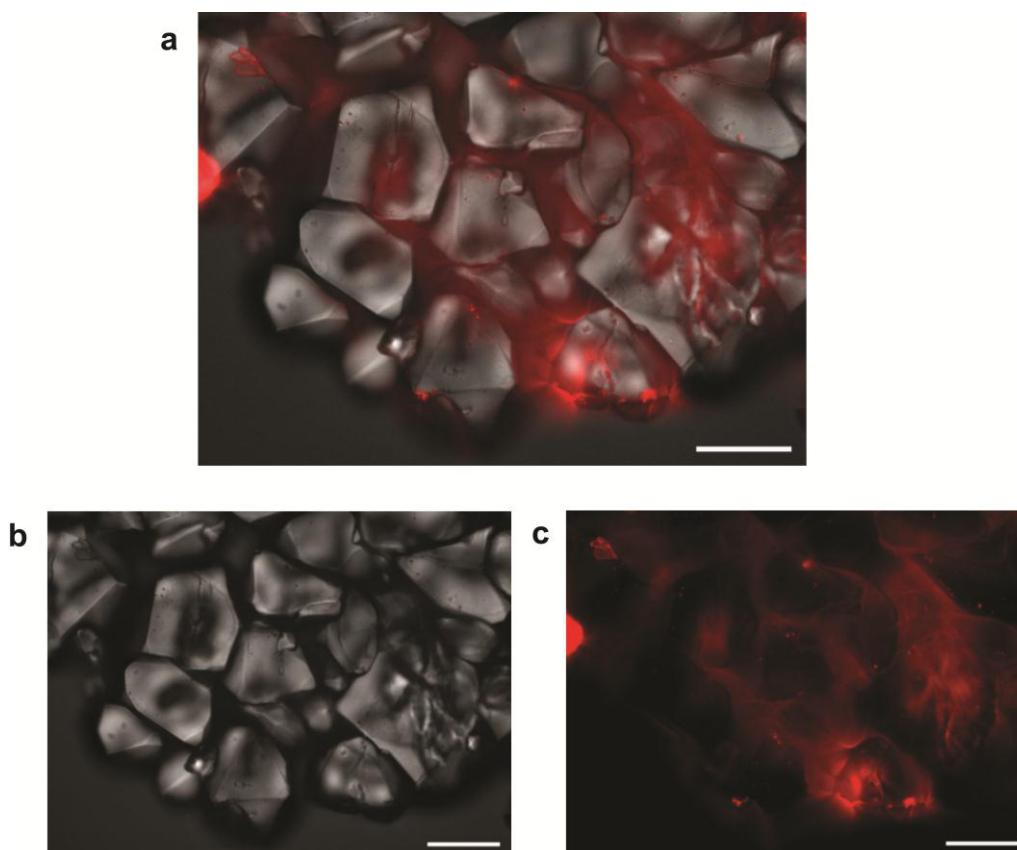


**Figure 3.3:** Optical micrographs of RDX crystals using bright-field DIC and wide-field microscopy techniques. Bright-field DIC and wide-field fluorescence overlay (a), bright-field DIC (b), and wide-field fluorescence (c) visualizing both the RDX crystal morphology (gray scale) and the presence of crystalline defects (red). Scale bars = 50  $\mu\text{m}$ .

It has been previously shown in literature that defects in energetic materials can be observed using confocal laser scanning microscopy by capitalizing on the difference between laser scattering of the crystal matrix and its defects<sup>88, 89</sup>. In an effort to increase size and shape defect resolution from crystal scattering artifacts in **Figure 3.3**, a fluorescent dye molecule was investigated to eliminate contributions from scattered light off of the crystal faces. Coupling the benefits of acquiring signal from an emitting molecule spectrally shifted from the excitation source with the gained spatial resolution of using a pinhole to eliminate signal not in the focal plane of interest may significantly enhance current microscopic

characterization specifications. It is clearly shown in **Figure 3.4** that the solvent defects in crystalline RDX shown in **Figure 3.3** are much more resolved using LSCM, where the quantity and the size of defects are more readily observable. The reduction in scattering artifacts by utilizing a pinhole allow for a more complete picture, where small defects approaching sub-micron were not previously able to be visualized. This gained resolution has large implications on the ability to screen batches of energetic materials for even small amounts of defects that can compromise both the material performance and safe handling.

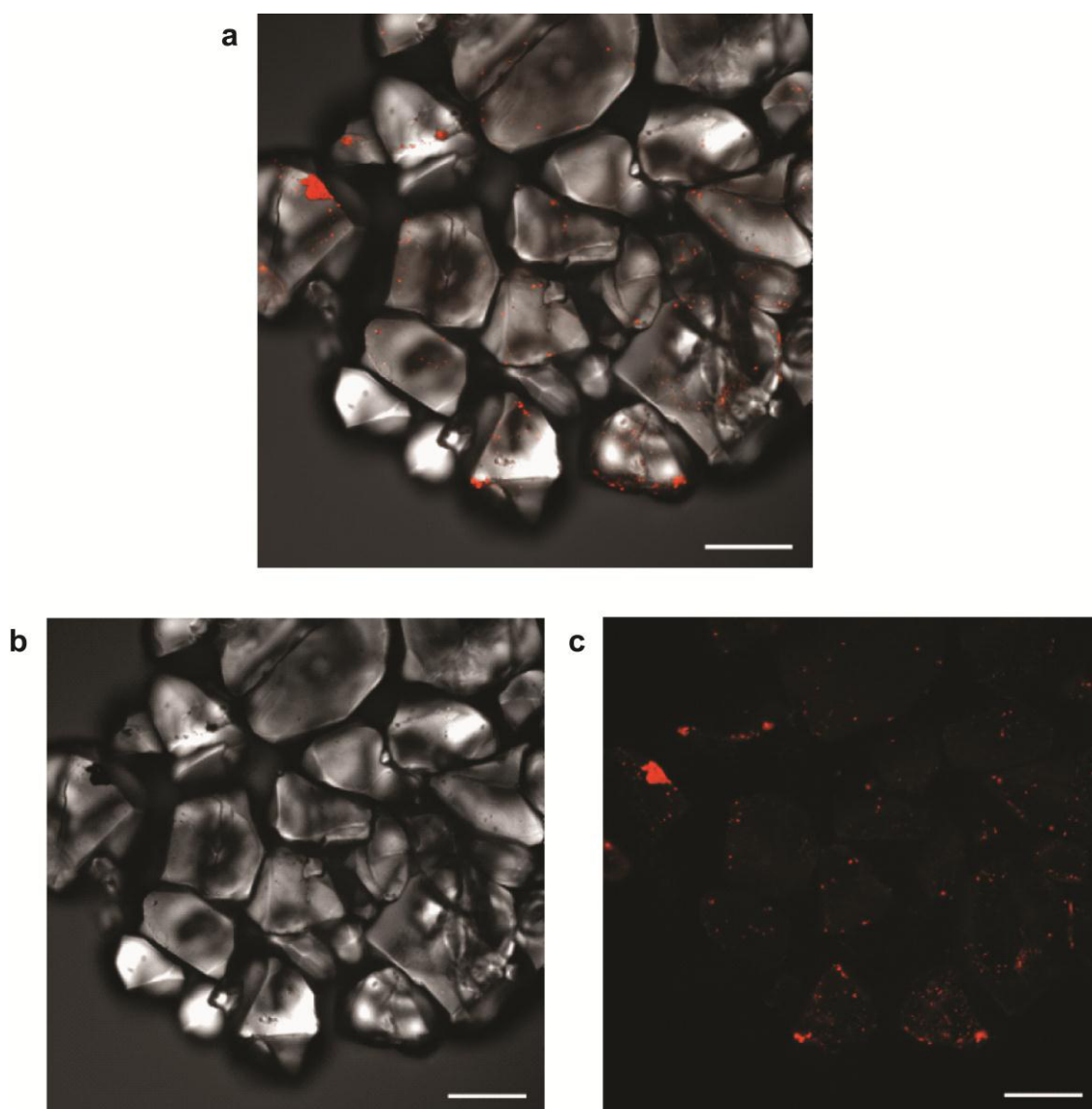


**Figure 3.4:** Optical micrographs of RDX crystals using LSCM techniques. TLD-DIC and Lissamine rhodamine B sulfonamide overlay (**a**), TLD-DIC (**b**), and Lissamine rhodamine B sulfonamide (**c**) visualizing both the RDX crystal morphology (gray scale) and the presence of crystalline defects (red). Scale bars = 50  $\mu\text{m}$ .

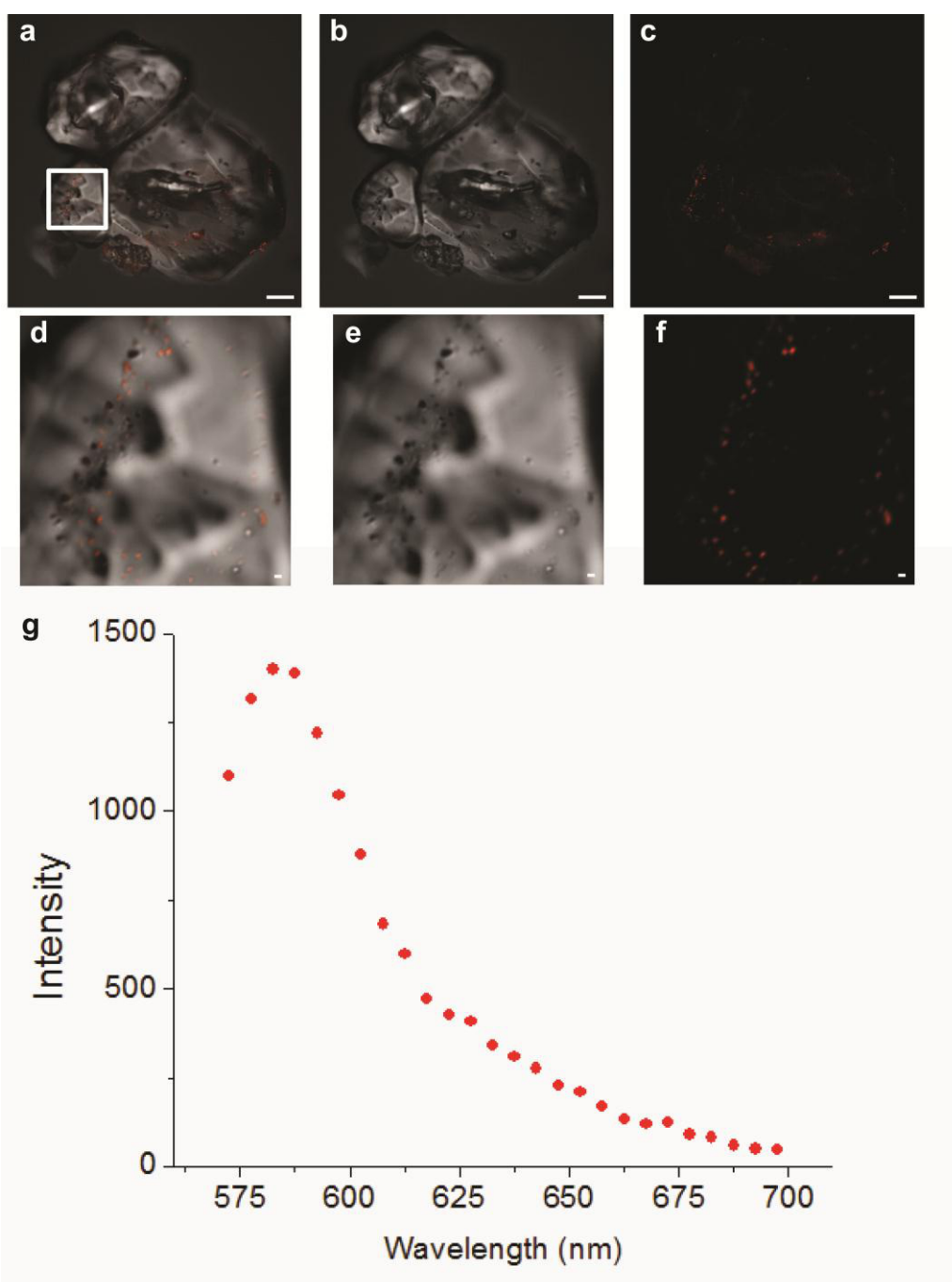


**Figure 3.5:** Optical micrographs of RDX crystals using TLD-DIC and confocal microscopy techniques. TLD-DIC and Lissamine rhodamine B sulfonyl chloride overlay (**a**), TLD-DIC (**b**), and Lissamine rhodamine B sulfonyl chloride, (**c**) visualizing both the RDX crystal morphology (gray scale) and the presence of crystalline defects (red). An electronic magnification of the same RDX crystal (white box in (**a**)), where the TLD-DIC and Lissamine rhodamine B sulfonyl chloride overlay (**d**), TLD-DIC (**e**), and Lissamine rhodamine B sulfonyl chloride (**f**) are shown. The spectral confocal profile of the signal acquired in (**g**) depicts signal originating from Lissamine rhodamine B sulfonyl chloride fluorescence. Scale bars (**a-c**) = 20  $\mu\text{m}$  and scale bars (**d-f**) = 1  $\mu\text{m}$ .

The use of LSCM to probe energetic crystals allows an electronic magnification to be employed for closer inspection of defects without sacrificing defect resolution as shown in **Figure 3.5**. At an objective magnification of 40X and an additional electronic magnification allows small defects on the order of sub-micron to be visualized. These observable defects were not observable using either bright-field or wide-field fluorescence microscopy techniques. The ability to visualize such small defects allows energetic materials to be more accurately characterized to aid in the development of IM. To ensure that the signal registered in the confocal microscope originates from Lissamine rhodamine B sulfonyl chloride and not some other artifact, such as excitation scattering, the intensity profile versus wavelength was acquired at each pixel and evaluated. The spectral profile for one of the observable defects in **Figure 3.5e** clearly demonstrates that the signal is due to the spectral manifold of Lissamine rhodamine B sulfonyl chloride. Acquiring spectral data is necessary to validate the observed signal in the respective detector due to scattering or laser diffraction artifacts. Under some instances of material characterization, the appearance of laser induced diffraction patterns around inclusions could also be observed as shown in **Figure 3.6**. The change in diffraction patterns around the solvent inclusions further validates the measured fluorescent signal.

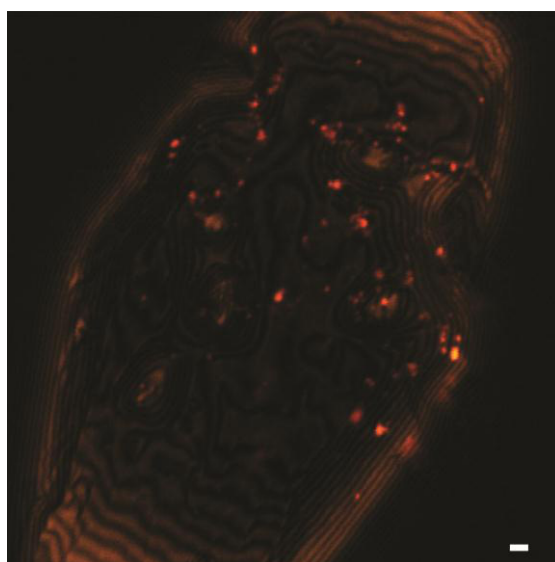


**Figure 3.6:** Laser-induced diffraction patterns can be observed in RDX showing distinct patterns around solvent inclusions. Scale bar = 2  $\mu\text{m}$ .

For a more complete picture of the defects found in energetic crystals it is important to probe the three-dimensional (3-D) defect populations. Since the use of LSCM utilizes a

pinhole to eliminate out of focus light, a series of two-dimensional (2-D) images in the (x,y) plane can be acquired with discrete steps along the z-axis to access optical information throughout many focal planes. Multiple 2-D images can be compiled and reconstructed to form a 3-D rendition for more complete particle characterization and analysis. The resolution between two objects in a 2-D image is dictated by an airy disk, where the resolution of two objects in a 3-D image is dictated by a point-spread function. The separation of two objects is resolvable until one airy disk interacts with more than half of the second airy disk. The diffraction limited resolution of optical microscopy approaches 200 nm. When comparing between 2-D and 3-D resolution, the z resolution is always less resolvable. Typically the z-axis resolution does not exceed 2-3 times the (x,y) resolution for a given specimen. A series of 2-D images can be compiled to form a z-stack and rendered to build a 3-D image, where the location and quantity of internal defects found in RDX can be seen as shown in **Figure 3.7**. The acquired data is shown at two different angles in order to show multiple perspectives. The elongation in the defects along the z-axis is an artifact attributed to z-aberration from the reduced resolution. Although slight aberration is observed, the lack of drastic z-axis fluorescence distortion in the shapes of the defects is quite promising for applications requiring the overall quality of energetic materials to be evaluated.

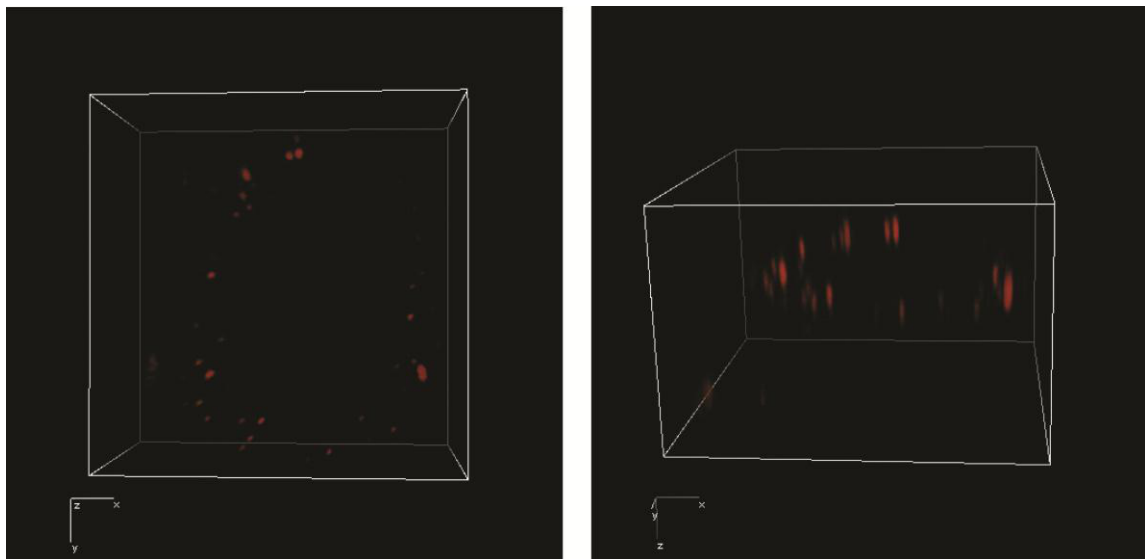


**Figure 3.7:** The 3-D reconstruction of defects within an RDX particle shown in red from two different perspectives.

### 3.5 Evaluation of Two Distinct Recrystallization Methods of RDX

In an effort to improve the overall quality of RDX, the use of sonocrystallization during the recrystallization process was evaluated compared to classical stirring recrystallization methods. Differences between RDX recrystallized from acetone using mechanical stirring based agitation and ultrasonic agitation are shown using optical microscopy characterization using matching index of refraction in **Figure 3.8**. A qualitative inspection of mechanical stirring agitation data shows a wide size distribution and inclusion content; while samples prepared using ultrasonic agitation clearly show a small size distribution with a small amount of internal defects. The rate of solvent evaporation also plays a major role on the formation of particles of RDX. **Figure 3.9** compares RDX prepared under sonocrystallization conditions with rapid solvent evaporation and slow evaporation. A clear difference in crystal morphology is observable, where the rapid evaporation of solvent leads to rough crystals with many solvent defects trapped within the particle. On the contrary, slow solvent evaporation leads to very smooth and uniform particles with no observable defects within the detection limits of the microscopy apparatus used in these studies. The recrystallization of RDX in the presence of ultrasound under slow evaporation conditions creates an ideal energetic material for IM applications.

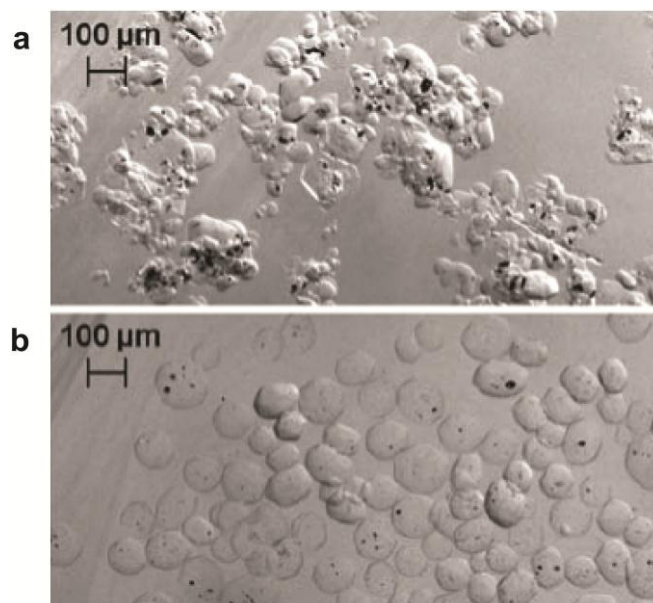


**Figure 3.8:** RDX particles formed using mechanical stirring agitation (a) and ultrasonic agitation (b). Scale bars = 100  $\mu\text{m}$ . Adapted from Roberts, C.W., Hira, S.M., Mason, B.P., Strouse, G.F. & Stoltz, C.A., *CrystEngComm*, 13, 1074-1076, 2011 – Reproduced by permission of the Royal Society of Chemistry.

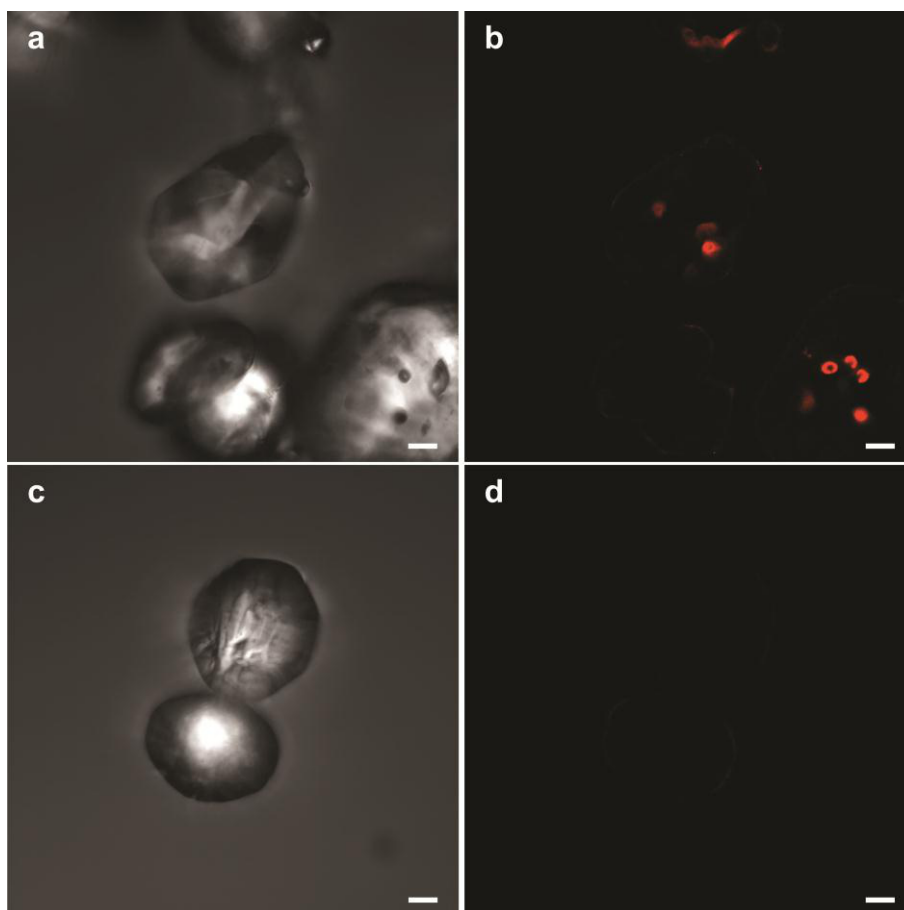


**Figure 3.9:** The formation of RDX particles using sonocrystallization under fast solvent evaporation (**a-b**) and slow evaporation (**c-d**), where both the TLD-DIC only (**a,c**) and the Lissamine rhodamine B sulfonyl chloride only (**b,d**) images are shown. Scale bars = 20  $\mu\text{m}$ . Adapted from Roberts, C.W., Hira, S.M., Mason, B.P., Strouse, G.F. & Stoltz, C.A., *CrystEngComm*, 13, 1074-1076, 2011.

### 3.6 Conclusions and Future Directions

The use of fluorescence microscopy techniques to characterize defects in energetic materials allows for both higher resolution and 3-D characterization. The ability to scatter particles of RDX onto glass without the need to use an index of refraction matching fluid allows for the rapid characterization of multiple formulations of energetic materials. The combination of dark background signal inherent with fluorescence microscopy and increased resolution of internal defects allows for higher quality materials to be regulated. The visualization of submicron defects using optical characterization techniques is a major step forward in energetic characterization. Moreover, the ability to characterize crystals in all three dimensions makes it possible to understand where these defects are located within the crystal framework. Future studies comparing crystal size with defect size, quantity, and

location may allow for new insights on the role of “hot spots” on energetic material properties. In addition to fluorescence based signal acquisition, the use of laser diffraction may also be used to probe the crystalline inclusions. It has been suggested that the local environment of Lissamine rhodamine B sulfonyl chloride can affect the energy of the peak wavelength. A closer investigation on the effect of the location of the defects with changes in the spectral profile of Lissamine rhodamine B sulfonyl chloride may also provide new insights into unique environs within a larger macro environment to better understand the crystal strain present in these materials. It is clear that the use of sonocrystallization drastically reduces the amount of defects in RDX particles. The adaptation of both the microscopy characterization and the recrystallization methods described above can significantly improve the quality regulation of RDX and provide a more uniform energetic material for its multitude of applications.

## CHAPTER 4

# DETECTION OF TARGET SINGLE STRANDED DNA USING A MICRO-FABRICATED HALL MAGNETOMETER WITH CORRELATED OPTICAL READOUT

*Portions of this chapter have been formatted for publication as follows:*

Hira, S.M., Aledealat, K., Chen, K., Field, M., Sullivan, G.J., Chase, P.B., Xiong, P., von Molnár, S., Strouse, G.F. Detection of target ssDNA using a micro-fabricated Hall magnetometer with correlated optical readout. *Manuscript Submitted.*

### 4.1 Introduction

The ability to detect and discriminate specific nucleic acid sequences within a biological mixture has implications for genome sequencing, bio-warfare target detection, and the development of an efficient point-of-care (POC) device for pathogen identification<sup>90-95</sup>. Through the integration of biology with nanotechnology, a detection platform utilizing magnetic transduction can capitalize on the high biological specificity of DNA base pairing<sup>96</sup>, the scalability of nanotechnology<sup>97</sup>, the selectivity of self-assembled monolayer technology<sup>98</sup>, and the sensitivity of magnetic transduction<sup>99, 100</sup>. Coupling the extreme sensitivity of Hall based magnetic detection, which operates over wide magnetic field and temperature ranges, with the versatility and specificity of DNA base pairing can allow the realization of a new biological detection strategy that will improve POC diagnostics and subsequent medical treatment.

In this chapter the detection of a 35-base pair DNA target sequence is demonstrated at the single-bead level on a Hall magnetometer biosensor. The biosensor is able to identify a single bead bound to target DNA (35 base pair) and is amenable to the discrimination of DNA at the 364 pM concentration in 36  $\mu$ M extraneous DNA (< 10ppm). The detection strategy utilizes three-strand DNA annealing to co-localize a superparamagnetic (SPM) bead labeled probe strand, a label-free target strand, and a receptor strand at the surface of the Hall device, which induces a voltage change in the Hall junction due to a change in the stray

magnetic field sensed by the device. This study demonstrates the effective use of an optical/magnetic bead detection platform to measure DNA at the picomolar (pM) level in the presence of  $\mu\text{M}$  extraneous DNA. The technology represents a mimic for pathogenic DNA or RNA detection. Development of single nucleotide mismatch and real world pathogen samples are underway, but are too preliminary to include within this chapter.

Many biosensors<sup>101-117</sup> still suffer from limitations in stability, portability, sensitivity, and selectivity. Traditional enzyme linked immunosorbant assay (ELISA) based sensor platforms are sensitive at the pM level and require 1-2 days for detection of a protein target. Giant magnetoresistive (GMR) sensors, which are recent additions to the biosensor field, can detect at the pM level or femtomolar (fM) level if magnetically assisted<sup>118</sup>. Optical based sensors, whether colorimetric or using fluorescence resonance energy transfer (FRET) assays allow detection at the attomolar (aM) to nanomolar (nM) level. A novel approach often utilized in optical based biosensors is the use of a three-strand DNA annealing approach to produce an optical response that is directly proportional to the annealing event. The use of three-strand ssDNA annealing strategies has been investigated for biological target detection for the last 15 years and has been shown increase overall sensitivity. Mirkin et al. first used the controlled assembly and aggregation of DNA labeled Au nanoparticles in solution as a colorimetric sensor<sup>119</sup>. Years later Taton et al. utilized the tethering of DNA coated Au nanoparticles to DNA coated surfaces using a label-free target sequence for Ag amplified colorimetric detection with single nucleotide mismatch sensitivity<sup>106</sup>. The technology has evolved further and has been shown to detect  $\sim 6 \times 10^6$  copies of genomic DNA using Ag amplified scanometric detection on a commercial platform<sup>120, 121</sup>. In addition to the assembly of Au nanoparticles, the assembly of Ag nanoparticles onto smooth metal films using three-strand DNA assembly has been demonstrated for surface-enhanced Raman spectroscopic detection of DNA sequences<sup>122</sup>. Optical methods focused on fluorescence blotting assays has reached aM sensitivities<sup>115</sup>, while methods employing energy transfer detection of the three-strand assembly allows nM pathogen DNA detection<sup>112</sup>. Despite these applications of multi-sequence DNA assembly in literature, current magnetic detection strategies have not utilized such three-strand DNA assemblies. Moreover, the use of a three-strand DNA strategy would allow screening of only the target ssDNA, which may lead to high throughput analysis.

Sensing technologies based on magnetic transduction, whether Hall magnetometry or GMR, circumvent many of the limitations of classical sensor designs since they exhibit low sensitivity to the surrounding biological matrix of samples, can be mass produced, and if

configured properly, can offer dynamic, label-free detection in a micro-fabricated scalable platform<sup>123, 124</sup>. Magnetic transduction based sensing technologies cover a wide range of methods including GMR sensors through the use of a spin valves<sup>118, 125-129</sup> or bead array counters (BARCs)<sup>130, 131</sup>, and Hall based sensors<sup>132-137</sup>. Already examples of GMR devices have demonstrated detection of matrix-insensitive proteins at the fM level using a magnetic transduction based device<sup>129</sup> and aM level by adding additional magnetic beads to amplify the signal<sup>138</sup>. The use of Hall magnetometry for DNA biosensing could represent the next generation for magnetic based transduction devices, since a Hall junction is a 4-point probe device (current, voltage), scalable down to the nanoscale, can be mass produced using standard photolithography and fabrication methods, displays a linear response through a wide range of magnetic fields<sup>139</sup> with minimal temperature range dependence<sup>140</sup>, and can operate at high frequency allowing for phase sensitive detection of the transient fields associated with SPM nanoscale beads. Hall biosensors may offer a viable alternative to exclusively fluorescence based microarray technologies for POC applications.

## 4.2 Experimental

### 4.2.1 Substrate Fabrication

The  $1\mu\text{m}^2$  Hall junction is fabricated into the surface of an epitaxially grown heterostructure consisting of a GaAs substrate containing an InAs quantum well core supplied by Teledyne Scientific Company, Thousand Oaks, California, USA. The devices were fabricated using a combination of photolithography and wet chemical etching. An insulation layer of  $\text{SiO}_2$  (60 nm) was sputtered over the entire device surface, followed by a layer of Ti (5 nm), and deposition of  $3\mu\text{m}$  gold pads (20 nm thick) directly over the protected Hall junction. A schematic of the layer by layer substrate components is shown in the **Figure 4.1**. Registry of the gold pad was accomplished by photolithography using alignment markers in the photomask. Initial mimics utilized number 1 or 1.5 glass coverslips or  $\text{SiO}_2$  wafer to evaluate DNA-bead assembly due to ease of microscopy analysis and availability. Subsequent mimic microarrays ( $3\mu\text{m}$  round patterns and  $2\mu\text{m} \times 4\mu\text{m}$  patterns) were fabricated onto the  $\langle 100 \rangle$  face of a single crystal GaAs wafer and resembled a more realistic mimic due to the device composition. Gold evaporation was accomplished immediately prior

to use to limit the contamination of the fresh gold surface from outside sources found in the ambient atmosphere.

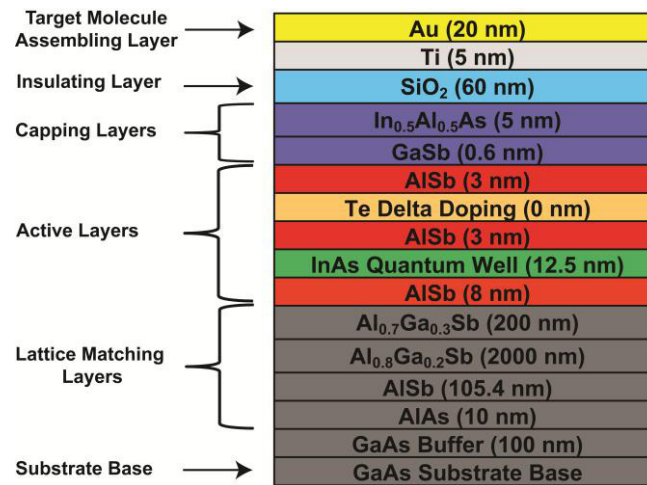


**Figure 4.1:** The composition of the Hall device heterostructure is shown, where the layers include a GaAs substrate base, layers to reduce lattice mismatches, active layers sandwiched between blocking layers, capping layers, an insulating layer, and the target molecule assembling layer.

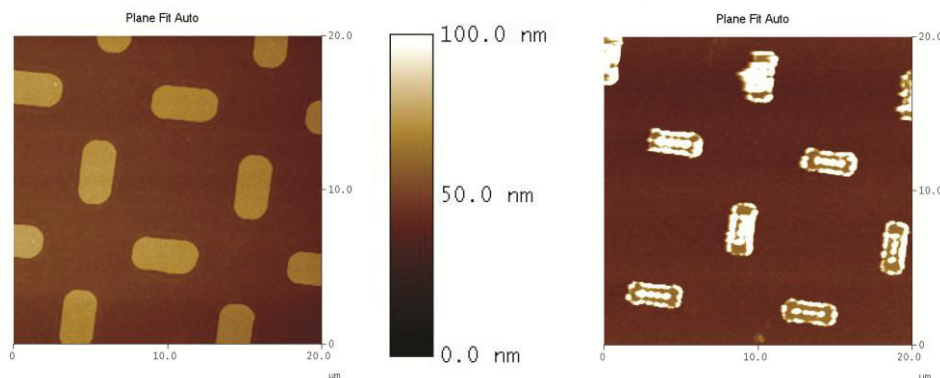


**Figure 4.2:** AFM micrographs of glass substrate mimics. The quality was evaluated based on the presence of artifacts, where a good quality substrate (**left**) lacks excessive topological features and a poor quality substrate (**right**) contains excessive topological features.

The overall quality of the patterned mimics or actual Hall device was evaluated prior to biological assembly using atomic force microscopy (AFM). Micrographs generated by AFM of two mimic substrates are shown in **Figure 4.2** to illustrate successful substrate patterning (**left**) and unsuccessful substrate patterning (**right**). In some cases, the photolithography process caused large structural artifacts around the photolithography

prepared patterns or resulted in the complete absence of patterns. Only substrates with clean patterns without artifacts were used for biological assembly.

### 4.2.3 Substrate Cleaning

The freshly Au deposited substrates were cleaned prior to use for 1 min at low power in an oxygen plasma (Harrick Plasma PDC-001). The oxygen plasma creates an oxidizing environment in which organic contaminants are oxidized along C-C bonds. The substrates were rinsed with HPLC grade absolute ethanol for 1 min and dried under a constant stream of nitrogen gas in a clean room environment. The use of lesser grades of ethanol yielded irreproducible molecular assembly, where it is suspected that the HPLC grade ethanol is of the purest form and essential to maintaining a clean gold substrate surface. The propensity of bulk gold to form gold oxide ( $\text{Au}_2\text{O}_3$ ) has been previously reported in literature, where the treatment of the oxidized surface with ethanol facilitated the reduction back to bulk gold<sup>141, 142</sup>. Although thermodynamically unstable,  $\text{Au}_2\text{O}_3$  can range in thickness from a few Å to tens of Å depending on the time of the oxidizing environmental conditions. While it has been shown that  $\text{Au}_2\text{O}_3$  will spontaneously reduce over time,  $\text{Au}_2\text{O}_3$  is stable enough that significant reduction will not occur over the timescales of our experiments described herein. The effectiveness of ethanol to reduce  $\text{Au}_2\text{O}_3$  back to bulk gold was investigated using X-ray photoelectron spectroscopy (XPS) to ensure that the substrates are ideal for successful subsequent DNA SAMs. Since the presence of Au oxide will only exist at the topmost surface layer, XPS characterization was chosen due to the inherent surface sensitivity of the technique. The XPS analysis of a gold oxide surface and a gold oxide surface followed by an ethanol rinse are shown in **Figure 4.3a-b**. The two signatures of interest are the Au 4f doublet and the O 1s singlet. The gold oxide sample exhibits peaks for the Au 4f doublet at 85.9 eV and 89.6 eV and an O 1s singlet at 530.4 eV, characteristics of  $\text{Au}_2\text{O}_3$ . The gold oxide surface followed by an ethanol rinse gives rise to peaks for the Au 4f at 84.1 eV and 87.8 eV and the O 1s at 532.5 eV. The chemical shifts observed for both the Au 4f and O 1s peaks are within the experimental resolution of 1.1 eV and are consistent with the chemical reduction of  $\text{Au}_2\text{O}_3$  to bulk Au by ethanol previously published in literature<sup>141, 142</sup>. In addition to the chemical shifts, a visual color change was observed from orange/brown ( $\text{Au}_2\text{O}_3$ ) to metallic gold (bulk Au) further confirming the experimental observation. The

XPS data collected provides evidence that an ethanol rinse is essential to ensure for a pristine bulk gold surface for subsequent molecular self-assembly.

The affect of cleaning methods on the cleanliness of Au films was investigated using static contact angle measurements. A SiO<sub>2</sub> wafer was coated with 5 nm of Ti followed by 20 nm of Au and subjected to a dilute solution of photoresist (1 drop in > 10 mL). The static contact angle was measured on a KSV contact angle measurement system after substrate cleaning using three separate methods and after a 15 second dips in a octadecanethiol (ODT) ethanol solution (3.5 mM). The normal wash method consisted of a 3 minute wash in acetone, 1 minute wash in methanol, and a 1 minute wash in isopropanol. The piranha cleaning method consisted of a 15 minute wash in freshly prepared piranha solution and copious amounts of 18.2 mΩ cm<sup>-1</sup> water. The final comparative method utilized 1 minute oxygen plasma under low power, followed by an ethanol rinse. Substrates subjected to all methods were dried under a constant stream of nitrogen gas. The normal wash resulted in static contact angles of 52.60° and 71.50° after cleaning and after the ODT dip, respectively. The piranha cleaned samples resulted in static contact angles of 70.25° and 105.22° after cleaning and after the ODT dip, respectively. The oxygen plasma cleaned samples resulted in static contact angles of 91.64° and 111.82° after cleaning and after the ODT dip, respectively. The data acquired from oxygen plasma cleaned samples followed by an ODT treatment are in good agreement with literature, validating the cleaning method used<sup>142</sup>. The effect of the PEG-silane on the wet ability of the SiO<sub>2</sub> surface was also empirically investigated using static contact angle measurements. It was found that piranha cleaning glass yielded a contact angle less than 10°, while PEG-silane treatment resulted in a 34° contact angle.

### 4.2.3 Substrate Passivation

In an effort to reduce the risk of biofouling outside of the deposited Au regions, the SiO<sub>2</sub> surface was passivated by 2-[Methoxy(Polyethyleneoxy)Propyl]-Trimethoxysilane (PEG-silane) (purchased from Gelest, Inc.)<sup>143</sup>. 100 μL of PEG-silane was added to 50 mL of HPLC grade toluene in a clean 50 mL graduated cylinder, followed by 40 μL of concentrated hydrochloric acid. The cleanliness of the glassware used is critical in the successful silanization of substrates. All glassware was cleaned with fresh piranha solution (30% hydrogen peroxide (30% v/v), 70% concentrated sulfuric acid) for at least 10 minutes, followed by copious amounts of 18.2 mΩ cm<sup>-1</sup> water, a final absolute ethanol rinse, and dried

at 115 °C. **Caution:** Piranha solution is violently reactive and should be handled with extreme care! Other important notes are as follows: Always add the hydrogen peroxide to the sulfuric acid when making piranha solution; the solution will become very hot very quickly. Use piranha solution immediately for best results. Because of the hazards associated with piranha solution only make necessary quantities for sufficient substrate cleaning. The PEG-silane solution was sonicated for 10 minutes and used immediately. It is important to note that water is produced in the silanization reaction, where a small amount may fall out of the clear toluene solution since it is denser than toluene. In cases when the silanization solution was cloudy with a homogenous milky precipitant, the functionalization of samples was aborted and the preparation of fresh PEG-silane was repeated.

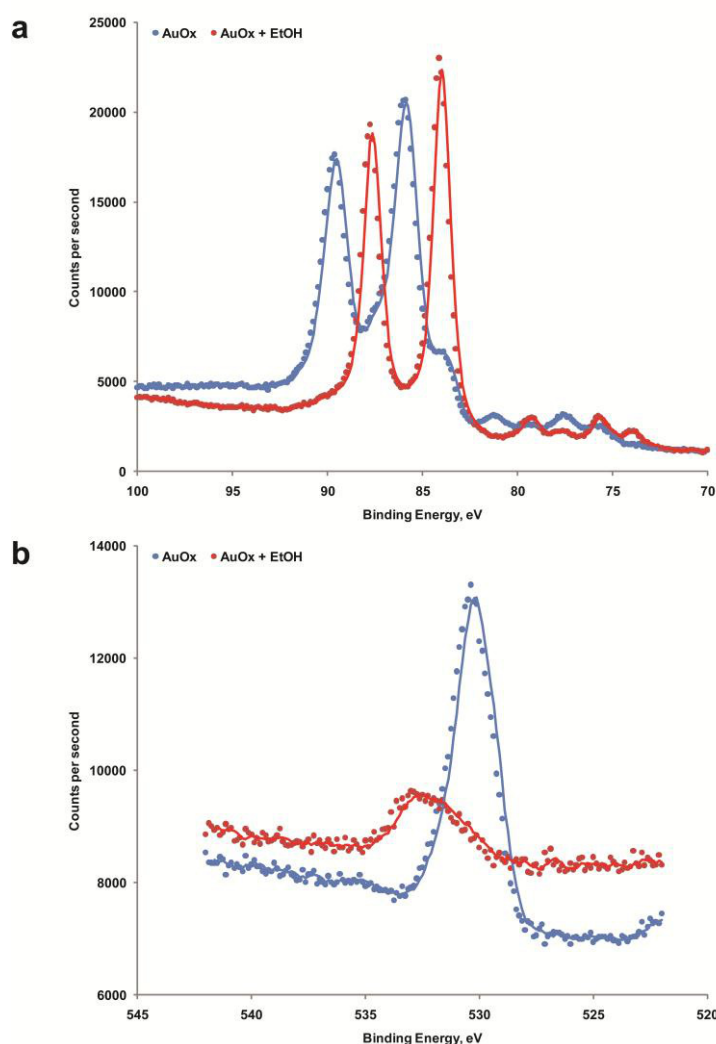


**Figure 4.3:** X-Ray Photoelectron Spectroscopy (XPS) characterization of the reduction of  $\text{Au}_2\text{O}_3$  to bulk Au by an ethanol rinse. The characteristic shifts in the Au 4f (top) and O 1s peaks (bottom) are shown for native  $\text{Au}_2\text{O}_3$  and  $\text{Au}_2\text{O}_3$  rinsed with ethanol.

**Table 4.1:** Characteristics of designed synthetic DNA using IDT DNA Oligo Analyzer 3.1.

NAME	SEQUENCE <sup>1,2</sup>	$\epsilon$ , $L \cdot (\text{mol} \cdot \text{cm})^{-1}$	$T_M$ , <sup>3</sup> °C	G-C CONTENT, %	$\Delta G$ Hybridization, $\text{kcal} \cdot \text{mol}^{-1}$	$\Delta G$ Homodimer Formation, $\text{kcal} \cdot \text{mol}^{-1}$	Hairpin <sup>3</sup> $T_M$ , °C
M35BiFAMIII	5'-/5Bio/CGA C/iFLUORdT/G TGA CAA TCT <b>AG CTG</b> CCG ATA GAG TAG TC-3'	354100	78.6	48.6	-61.46	-6.34	27.6
M35SSIII	5'-RSSR-GAC TAC TCT ATC GGC <b>AGC TAA</b> GAT TGT CAC AGT CG-3'	337500	78.6	48.6	-61.46	-6.34	29
M35SSNon- CompControllIII	5'-RSSR-CGA CTG TGA CAA TCT TAG CTG CCG ATA GAG TAG TC-3'	340400	78.6	48.6	-61.46	-6.34	27.6
M15BiFAMIV	5'-TCA TTC ACA CAC /iFLUORdT/CG /3Bio/-3'	151400	62.9	46.7	-25.19	-3.61	N/A
M20SSIV	5'-/RSSR/ GTC TTG TCT CCT GTC <b>AGC TA</b> -3'	178300	70.6	50.0	-33.29	-6.34	-5.3
M35CompIV	5'-CGA GTG TGT GAA TGA T <b>AG CTG</b> ACA GGA GAC AAG AC-3'	361400	79.1	48.6	-59.96	-6.34	20.5
M35NonCompIV	5'- GTC TAA GAG TGT CCT GGC TAT GAT CCG TGA GTA TG-3'	340800	78.4	48.6	-60.73	-4.62	15.7

<sup>1</sup> Modifier Key: /5Bio/ = 5' biotin, /iFLUORdT/ = internal Fluorescein dT, /RSSR/ = 5' C<sub>6</sub>H<sub>12</sub>OH disulfide C<sub>6</sub>H<sub>12</sub> Linker  
<sup>2</sup> **AGCT** = recognition sequence for ALUI enzyme  
<sup>3</sup> Based on 20 mM sodium phosphate buffer with 300 mM NaCl at pH 7.0

#### 4.2.4 Synthetic DNA Design

Synthetic DNA oligonucleotides were commercially synthesized (Midland Certified Reagent Company). The two-strand DNA system consisted of a 5' disulfide modified complementary receptor sequence 5'- /RSSR/- GAC TAC TCT ATC GGC AGC TAA GAT TGT CAC AGT CG-3', a 5' disulfide modified non-complementary receptor sequence 5'- /RSSR/- CGA CTG TGA CAA TCT TAG CTG CCG ATA GAG TAG TC -3', and a 5' modified biotinylated probe with an internal fluorescein dT sequence 5'- /BIOTIN/- CGA C - /iFLUORdT/- G TGA CAA TCT TAG CTG CCG ATA GAG TAG TC -3'. The three-strand DNA system and consisted of a probe sequence 5'-TCA TTC ACA CAC -/iFLUORdT/- CG - /3BIOTIN/- 3' labeled with an internal fluorescein dT and biotin, receptor sequence 5'- /RSSR/- GTC TTG TCT CCT GTC AGC TA -3' with a disulfide modifier, a 35 base pair unmodified target sequence 5'- CGA GTG TGT GAA TGA TAG CTG ACA GGA GAC AAG AC -3', and a 35 base pair unmodified non-target control sequence 5'- GTC TAA GAG TGT CCT GGC TAT GAT CCG TGA GTA TG -3'. The lyophilized DNA was buffer exchanged using a NAP-V size exclusion column (GE Healthcare) equilibrated with 20 mM sodium phosphate buffer, 50 mM NaCl pH 7.0. The 5'-/RSSR/- functionality on the receptor ssDNA consisted of a six carbon spacer, a disulfide, and a hexanol terminus. The 5'- /BIOTIN/ and the /3BIOTIN/-3' are designed to link with streptavidin coated superparamagnetic (SPM) nanobeads (350 nm mean size, Bangs Laboratories). The use of SPM beads allows the beads to remain dispersed in solution due to paramagnetic behavior at RT until an external magnetic field is applied preserving the native structure and function of biological targets. The specific linkage of biotin with streptavidin was chosen to conjugate the DNA to the nanobeads based on its profound binding constant of  $10^{15} \text{ M}^{-1}$  and its high temperature stability of 112 °C when fully conjugated<sup>144</sup>. Finally, the -/iFLUORdT/- modifier is a fluorescein dT on a six carbon spacer internally and covalently bound to a thymine base. The use of a fluorescent dye was engineered as a component in the device platform as a redundant optical signature for dual modality readout and serves as a direct comparator to fluorescent microarray technology. The presence of a fluorophore in the annealing strategy is completely independent from magnetic transduction based detection and has no bearing on the measured Hall response. Based on the mean size and binding capacity of the commercially available SPM nanobeads, each 350 nm magnetic bead contains approximately 36,000 probe DNA strands, each of which contain a fluorescent marker.

Although it is expected that the dye labeled probe DNA involved in hybridization would not emit due to energy transfer between the dye and the gold surface, there are tens of thousands of markers that are outside of the critical distance for energy transfer to occur and are therefore still observable. The DNA was synthetically designed to base pair to complement DNA through Watson-Crick base pairing and limit the amount of secondary interactions that can take place. Sequences were evaluated using IDT DNA Oligo Analyzer 3.1 for molecular weight, melting temperature ( $T_M$ ), G-C content, extinction coefficient, homo dimer formation, and hairpin analysis as shown in **Table 4.1**. Both the two-strand and three-strand DNA variants were engineered to have an enzyme cut site for ALU1, although it was not utilized for the experiments described herein. Since enzyme binding sites are palindromic and can influence homo-dimer formation, the  $\Delta G$  of each DNA sequence was kept above  $-9 \text{ kJmol}^{-1}$  during design to minimize the probability of unwanted DNA structures formed at room temperature.

DNA hybridization was evaluated using a gel shift assay for both three-strand and two-strand DNA assemblies using native polyacrilamide gel electrophoresis (PAGE) as shown in **Figure 4.4**. The change in DNA mobility in the gel caused by sequence length and structure can be seen for the three-strand (**Figure 4.4a**) and two-strand (**Figure 4.4b**) annealing strategies. The designation of lane contents with numbers for **Figure 4.4a** are as follows: (1) visual loading dye not observed under fluorescent excitation, (2) reporter strand (disulfide 20mer) and complementary target, (3) probe strand (fluorescein labeled 15mer), (4) reporter and probe strands, (5) probe and complementary target, (6) probe and non-complementary target, (7) reporter, probe, and complementary target, (8) reporter, probe, and non-complementary target. The visible bands (3-8) originate from the internal fluorescein modification on the probe strand and the differences in mobility reflect the assembling of the three-strand DNA structure. The arrow in (7) signifies the three-strand DNA product, and the band immediately below is most likely attributed to the probe annealed to the complementary target. The designation of lane contents with numbers for **Figure 4.4b** are as follows: (1) probe strand (fluorescein labeled 35mer), (2) complementary reporter and probe strands, (3) non-complementary reporter and probe strands. The visible bands (1-3) originate from the internal fluorescein modification on the probe strand and the differences in mobility reflect the assembling of the two-strand DNA structure. **Figure 4.4** clearly demonstrates the successful assembly of the two-strand and three-strand DNA architectures at room temperature. Although annealing does not continue to completion, the presence of a detectable quantity of product was observed.

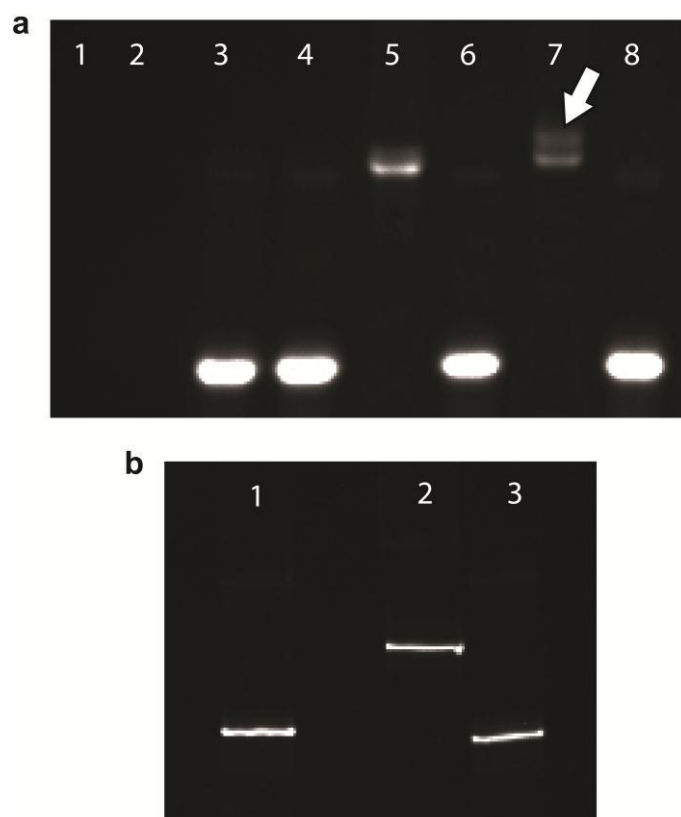


**Figure 4.4:** Native polyacrylamide gel electrophoresis characterization for the three-strand DNA assembly in the absence of nanobeads showing different mobilities of (1) visual loading dye not observed under fluorescent excitation, (2) reporter strand (disulfide 20mer) and complementary target, (3) probe strand (fluorescein labeled 15mer), (4) reporter and probe strands, (5) probe and complementary target, (6) probe and non-complementary target, (7) reporter, probe, and complementary target, (8) reporter, probe, and non-complementary target (a). The visible bands (3-8) originate from the internal fluorescein modification on the probe strand and the differences in mobility reflect the assembling of the three-strand DNA structure (a). The arrow in (7) signifies the three-strand DNA product, and the band immediately below is most likely attributed to the probe annealed to the complementary target (a). Native polyacrylamide gel electrophoresis characterization for the three-strand DNA assembly in the absence of nanobeads showing different mobilities of (1) probe strand (fluorescein labeled 35mer), (2) complementary reporter and probe strands, (3) non-complementary reporter and probe strands (b). The visible bands (1-3) originate from the internal fluorescein modification on the probe strand and the differences in mobility reflect the assembling of the two-strand DNA structure (b).

#### 4.2.5 DNA Immobilization and Hybridization

The receptor DNA (not previously reduced) was incubated on top of the device for 6 hrs, in an enclosed incubation chamber containing a supersaturated NaCl solution for humidity stabilization, in the form of a 50  $\mu$ L droplet at a DNA concentration of 9  $\mu$ M. The device

was immersed in 5 mL of  $18.2 \text{ m}\Omega \text{ cm}^{-1}$   $\text{H}_2\text{O}$  containing 0.1% Tween-20 (v/v), twice in 5 mL of  $18.2 \text{ m}\Omega \text{ cm}^{-1}$   $\text{H}_2\text{O}$  to rinse and remove unbound sequences of DNA, and dried under a constant stream of nitrogen gas. It is interesting to note that both not pre-reducing the disulfide modification before self assembly and later not reacting the surface with 6-mercaptohexanol did not hinder subsequent DNA hybridization as previously reported in literature for free thiols<sup>96, 145</sup>. The subsequent successful DNA hybridization may be attributed in part to the carbon-carbon packing of the carbon spacer or to the steric hindrance caused by the hexanol terminus to effectively separate the immobilized DNA to allow sufficient space for DNA base pairing. The reporter DNA was bio-conjugated to the SPM nanobead (350 nm mean size, Bangs Laboratories) through a biotin-streptavidin linkage at 30 °C for 1 hr. The DNA-nanobead conjugate was purified away from free DNA using magnetic separation and washing the sample 5 times with 20 mM sodium phosphate buffer, 300 mM NaCl pH 7.0. The three-strand DNA strategy included a pre-conjugation step of the target DNA to the probe DNA-SPM conjugate at 80°C and allowed to slowly cool over 1 hr. Unbound nucleic acids were purified away using magnetic separation. The hybridization assay was carried out by incubating a 25  $\mu\text{L}$  droplet of target biotinlyted DNA (7  $\mu\text{M}$ ) bound to streptavidin coated SPM beads for 2 hrs in an enclosed incubation chamber containing a super saturated NaCl solution. The device was washed once in 5 mL of 20 mM sodium phosphate buffer with 300 mM NaCl at pH 7.0 containing 0.1% Tween-20 (v/v), twice in 5 mL of 20 mM sodium phosphate buffer with 300 mM NaCl at pH 7.0, and stored in of 20 mM phosphate buffer with 300 mM NaCl at pH 7.0 and protected from ambient light. The assembly of two-strand and three-strand ssDNA strategies on GaAs mimics is shown in **Figure 4.5**. In both strategies employed, the complementary ssDNA (**Figure 4.5a,c**) annealed on the substrates and gives rise to a green fluorescence signature in a patterned array. In the presence of non-complementary ssDNA (**Figure 4.5b,d**), no assembly and thus no pattern occurs. For further scanning electron microscopy (SEM) analysis and Hall detection the substrates are immersed in a 300 mM sodium acetate solution for 5 minutes and dried under a constant stream of nitrogen gas over a NdFeB magnet. The use of sodium acetate is crucial to maintaining clean surfaces deplete of crystalline salts.

## 4.2.6 Microscopy Details

Fluorescent microscopy was carried out on an inverted Nikon TE2000-E2 Eclipse microscope (Nikon Instruments Inc.) equipped with a Nikon CFI Plan Apochromat 40X objective (NA 0.95, 0.14 mm WD). Wide-field imaging of the substrates utilized an EXFO E-Cite illumination source, a FITC filter (Chroma, ex: 480/30, DCLP: 505, em: 535/40). Images were acquired on a Photometrics Coolsnap HQ<sub>2</sub> CCD camera. Bright-field overlays utilized differential interference contrast (DIC) to observe the differences in the index of refraction of the samples. The data were analyzed using Nikon NIS Elements software. Scanning electron microscopy (SEM) was carried out on a FEI Nova 400 Nano SEM and utilizing a through-the-lens (TLD) detector. Samples were imaged natively without a conductive coating. Charging of the samples is evident because the substrates contain magnetic beads and consist of patterned Au (conductor) on SiO<sub>2</sub> (insulator). Artifacts due to charging were limited by using an excitation of 1 keV. The SEM images were acquired using a 32 scan average to obtain the clearest data.

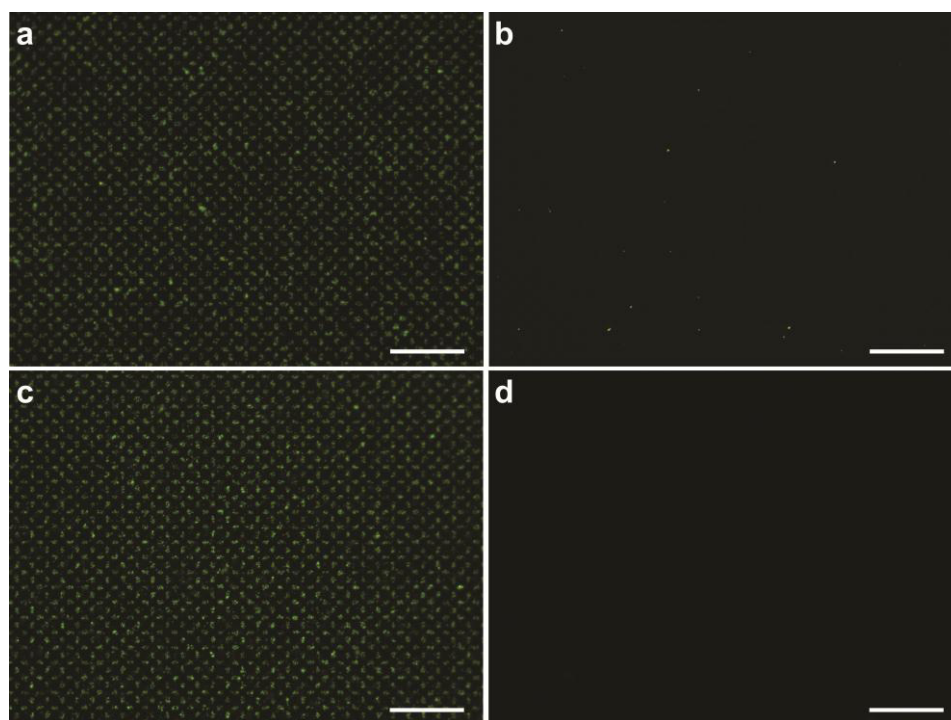


**Figure 4.5:** The assembly of two-strand (**a-b**) and three-strand (**c-d**) ssDNA strategies, where green fluorescence indicates the location of the SPM conjugated nanobeads. The complementary sequence (**a,c**) results in assembly and the non-complementary sequence (**b,d**) does not result in assembly. Scale bars = 50  $\mu\text{m}$ .

## 4.2.7 Hall Measurement

The detection of pre-immobilized SPM beads is achieved by employing an ac phase-sensitive technique previously reported<sup>137</sup>. The Hall device is biased with a dc current  $I = 50 \mu\text{A}$  and the beads are magnetized with an ac magnetic field; lock-in detection of the ac Hall voltage occurs at the magnetic field frequency. The application of an additional dc magnetic field reduces the SPM bead's susceptibility and thus the ac magnetic field generated by the beads. This produces a drop in the ac Hall voltage signal indicating the presence of the beads.

## 4.3 Results and Discussion

### 4.3.1 Design

A schematic of the Hall magnetometer based biosensor and detection strategy used for detection of a single stranded DNA (ssDNA) target sequence by three-strand annealing over the surface of a  $1 \mu\text{m}^2$  Hall junction is shown in **Figure 4.6**. The biosensor platform is assembled in parallel steps in order to limit the processing time for target detection. In theory, the platform can be operated in a label-free approach, as shown by others for equivalent three-strand annealing SERS<sup>122</sup> and colorimetric (gold plasmon shift) based technologies by simultaneously annealing the target, sensor, and probe sequences<sup>106, 119-121</sup>. The platform is composed of six  $1 \mu\text{m}^2$  Hall junctions (**Figure 4.7a**) etched into an epitaxially grown, vertically integrated InAs quantum well heterostructure isolated from the surrounding environment by a 60 nm overlayer of silicon dioxide, as previously described<sup>134, 136</sup>. The six available Hall junctions are divided into a set of three bio-active sensors (i, ii, iii) and three non-active controls (ic, iic, iiic). The bio-active sensors are generated via patterning  $3 \mu\text{m}$  gold bonding pads evaporated onto the  $\text{SiO}_2$  layer only over the bio-active junctions (i, ii, iii). The bonding pads provide a site for self-assembly of the receptor single strand DNA onto the surface of the Hall junction sensor without modifying the properties of the InAs quantum well heterostructure. The non-active controls do not have the gold bonding pad. To minimize bio-fouling of the device by the biological constituents in the sample via non-specific interactions, the exposed  $\text{SiO}_2$  surface is selectively modified by a polyethylene glycol conjugated silane moiety<sup>143</sup>. The bio-active junctions are modified by self-assembly of the receptor ssDNA (blue) onto the gold pads by exposure of a solution of the receptor to

the Hall junction platform (**Figure 4.6-I**), and subsequent washing to remove unbound DNA. The fluorescein labeled probe ssDNA sequence (red) is pre-appended to the SPM bead platform via streptavidin-biotin conjugation (**Figure 4.6-II**).

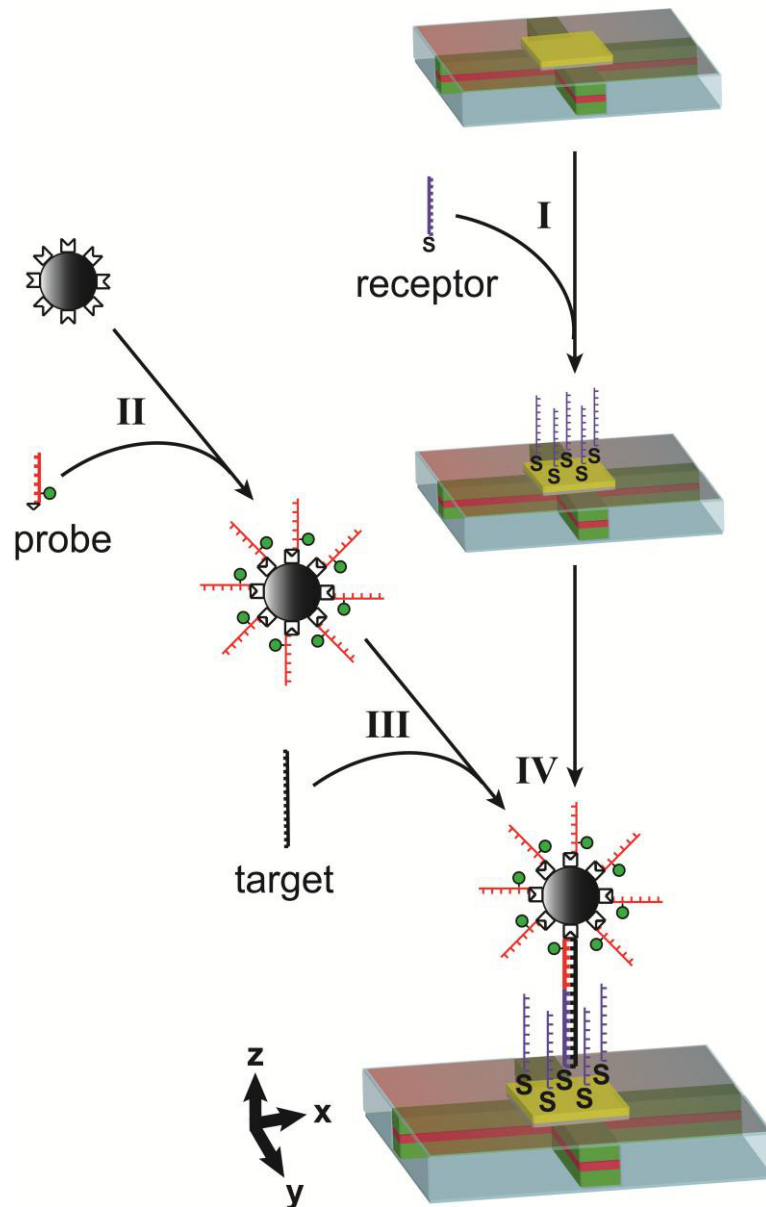


**Figure 4.6:** Generalized schematic for the detection of label-free target DNA using Hall magnetometry. The label-free target DNA (black) is detected by immobilization at the Hall device via complementary base pairing with receptor DNA (blue) pre-assembled on the Hall device surface to additional complementary probe DNA (red) with an internal fluorescent marker pre-conjugated to the surface of a magnetic nanobead resulting in a detectable Hall signal. Nanobead is not drawn to scale.

Prior to the detection of the target DNA sequence (black), the probe strand and the target strand are pre-hybridized (**Figure 4.6-III**). The detection of the target DNA is then accomplished by annealing the SPM bead-probe-target complex with the receptor sequence (blue) pre-assembled at the surface of the Hall device platform at room temperature (**Figure 4.6-IV**). The assembly of the three-strand sequence requires 3 hr, which is equivalent to standard FRET, plasmonic, GMR and SERS based detection scenarios, but far faster than optical chip techniques that can require 16-24 hrs to achieve hybridization. Although the simultaneous addition of all three ssDNA components is experimentally feasible, stepwise assembly allowed the added benefit that the observed signal is not artificially enhanced by non-specific, non-DNA bound SPM beads. All unbound nucleic acid species and nucleic acid labeled SPM beads are removed by magnetic separation prior to final three-strand DNA assembly and washed prior to Hall detection. The strategy allows the specific binding event at the electrically isolated gold pad to induce a direct voltage response in the device without altering the device properties directly, as would be observed in SPR based devices. The stepwise, parallel strategy allows convenient concentration amplification for the target ssDNA from extraneous DNA fragments. The overall performance of a biosensor is reflected in the ability to discriminate binding, the limit of detection of binding, and the fidelity of binding as described below.

### 4.3.2 Detection

In **Figure 4.7** the detection of the 35-bp target on the dual optical/ Hall device sensor is shown for a 25  $\mu$ L droplet containing 7  $\mu$ M DNA. The specificity of the assembly of the three-strand DNA complex onto the gold pad (grey circle) over the Hall junction is clearly observed in the wide-field fluorescence overlaid with differential interference contrast (DIC) micrograph (**Figure 4.7a**). The observed green photoluminescence in **Figure 4.7a** arises from the fluorescein label on the probe strand and requires the three strand annealing process to occur in order for the probe to be optically detectable. The lack of non-specific binding of the probe to regions outside of the gold pad region confirms the specificity of the three-strand assembly protocol. The specificity of the assembly on the gold pads is further confirmed by comparing the optical micrograph (**Figure 4.7a**) and the scanning electron micrograph (**Figure 4.7b, Figure 4.8**). Scanning electron microscopy (SEM) imaging of junction (iii) indicates  $\sim$ 73 beads are present on the 3  $\mu$ m gold pad. Inspection of the DIC image of

junction (iii) (**Figure 4.7a**) reveals the registry between the underlying Hall junction in the SEM image (**Figure 4.7b**, grey box) and the gold pad on the surface of the Hall magnetometer results in only ~12 nanobeads being positioned directly or partially over the active area of the Hall junction.

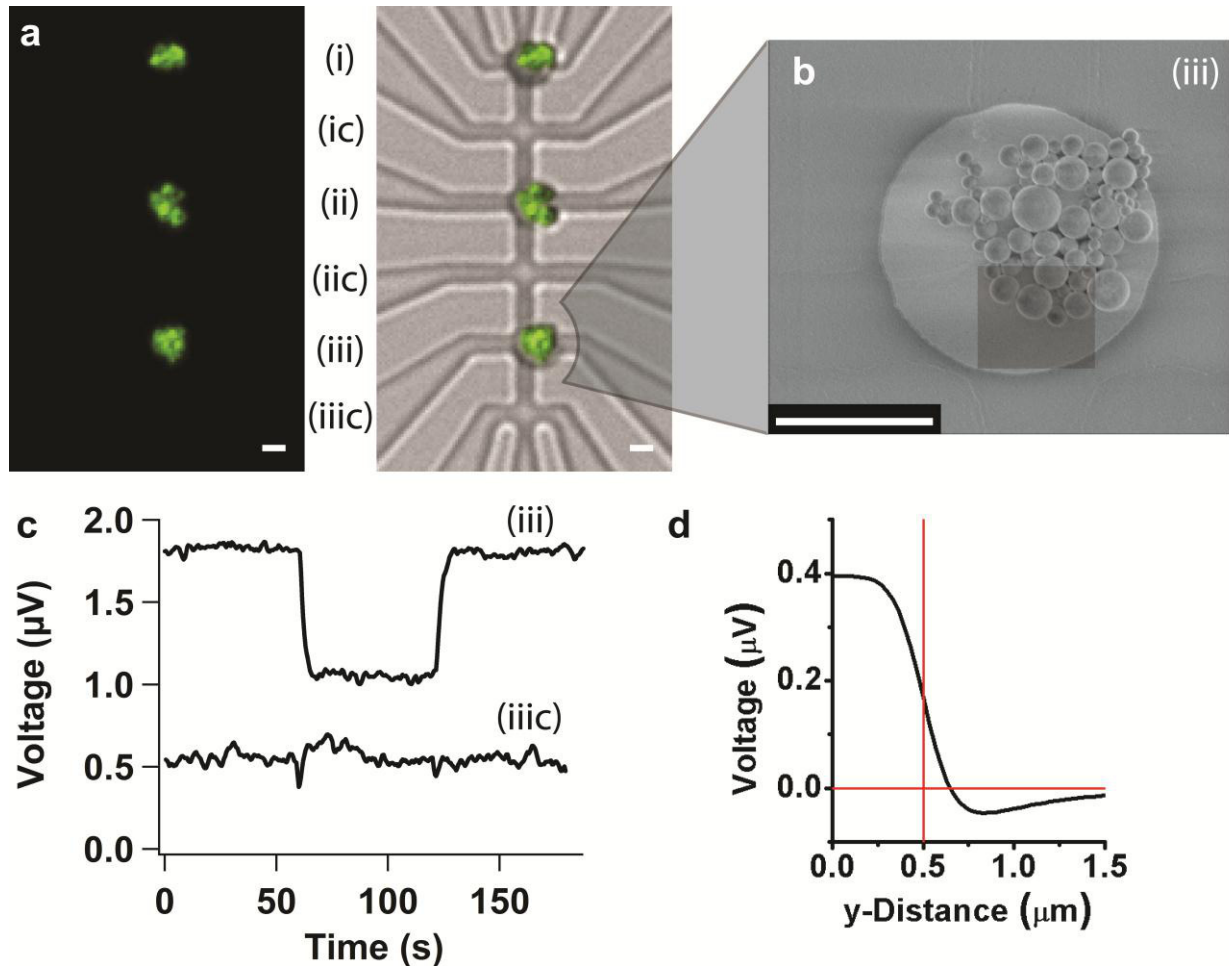


**Figure 4.7:** Optical microscopy characterization (wide-field fluorescence and DIC overlay) of three-strand DNA assembly is shown by the presence of green fluorescence indicating the presence of probe DNA (**a**). SEM was used to evaluate the location and to quantify the number of nanobeads contributing to the Hall response for (iii), where the grey box designates the location of the underlying Hall junction (**b**). Hall responses for three active junctions (i, ii, iii) and a single control junction (iiic) are plotted as Hall voltage offset versus time; the presence of nanobeads over the active Hall junctions results in a drop in Hall voltage when a dc magnetic field is applied (**c**). The theoretical device signal stemming from a single 344 nm SPM bead is shown to the right as a function of position over the Hall junction further illustrating the local sensitivity of Hall magnetometry (**d**). Scale bars = 2  $\mu\text{m}$  in panels **a,b**.

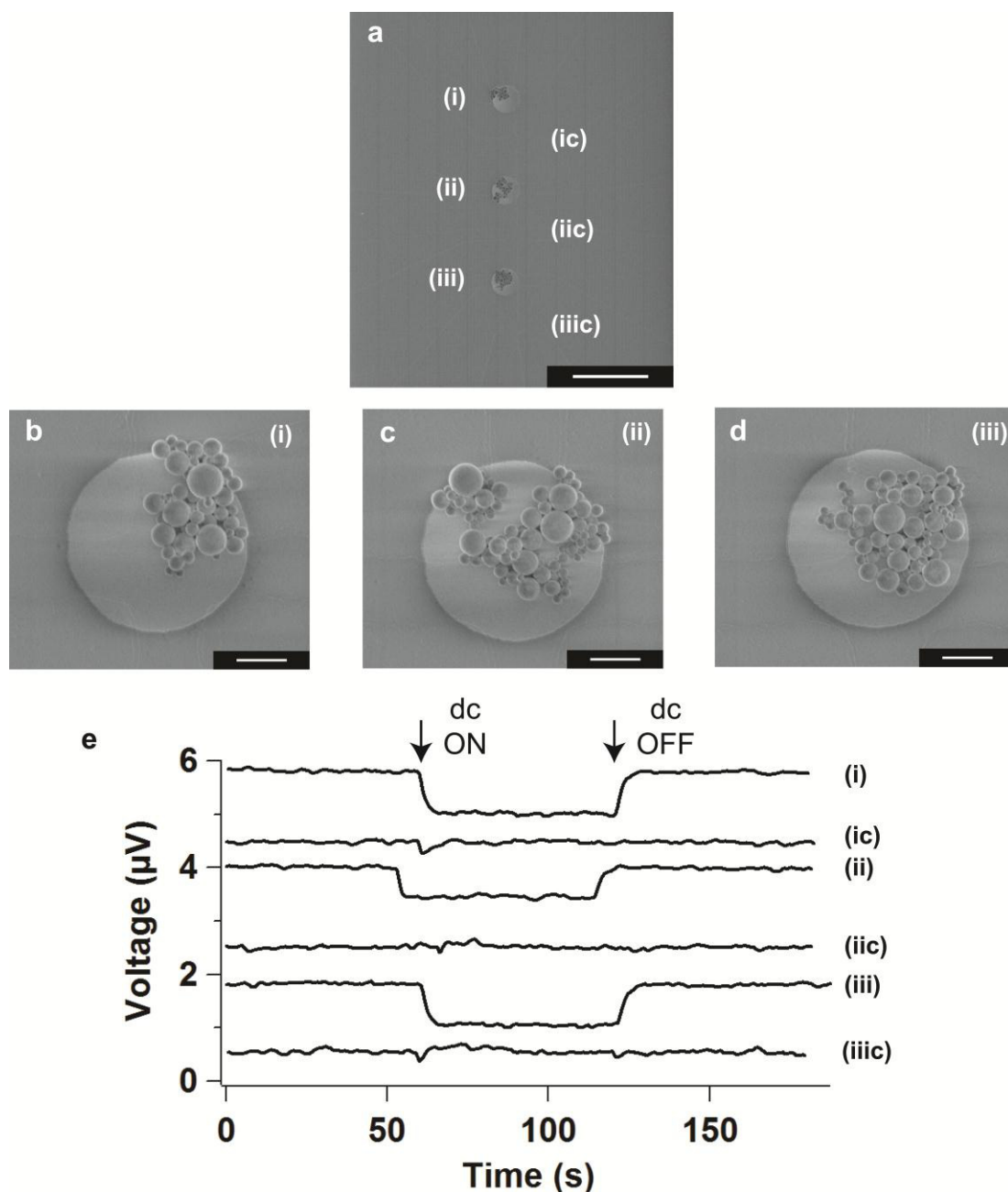


**Figure 4.8:** SEM micrograph depicting label-free, three-strand DNA assembly of all six junctions of a Hall magnetometer (a). Scale bar (a) = 10 μm. SEM micrographs at higher magnification of the three active Hall junctions, where the ratio of beads entirely or partially over the Hall junction versus beads outside of the junction are (b) 8/41, (c) 11/68, and (d) 12/73. Scale bars (b-d) = 1 μm. Hall responses for three active junctions (i, ii, iii) and three non-active control junction (ic, iic, iiic) are plotted as Hall voltage versus time; the presence of superparamagnetic (SPM) nanobeads over the active Hall junctions results in a drop in Hall voltage when a dc magnetic field is applied (e). When the dc magnetic field is removed the signal returns to baseline (e).

For detection of the DNA annealing event, the presence of the SPM bead is measured as a change in voltage by the use of both an ac and dc magnetic field. The use of both ac and dc fields allows for the binding event signal to be cleanly isolated by using lock-in detection. In the absence of the external dc field, no signal is detectable in the Hall junction. The ac magnetic field of 3.76 mT at 93 Hz is used to induce magnetization of the SPM nanobeads. The 70.6 mT dc magnetic field (NdFeB) is applied perpendicular to the Hall junction to shift the magnetization of the nanobeads to lower susceptibility as given by the expression  $\Delta V_H \propto \Delta M$ , where  $\Delta M$  is the change in the ac magnetization before and after the dc field was applied. The Hall sensor was operated in constant current mode with an applied dc current of 50  $\mu$ A.

The voltage response to binding of the target sequence with the pre-appended probe and 350 nm magnetic bead to the receptor strand on single active junction and a single control junction are shown in **Figure 4.7c**. The voltage response for all junctions and controls are shown in **Figure 4.8**. The voltage across the control junction (iiic) is  $0 \pm 0.03$   $\mu$ V. The successful assembly of ssDNA over the active Hall junctions (i, ii, iii) results in a sharp drop in measured Hall voltage for all three active sensor elements. The Hall voltage measurements are 0.79  $\mu$ V (Signal/Noise (S/N) 40), 0.55  $\mu$ V (S/N 28), and 0.78  $\mu$ V (S/N 39) for (i, ii, iii), respectively. In **Figure 4.7**, the observed step function is generated by the application and removal of the external dc magnetic field in the presence of the small ac field to allow lock-in detection. The standard deviations in signal or noise levels for all junctions (i, ic, ii, iic, iii, iiic) is  $< 0 \pm 0.04$   $\mu$ V on average in the presence and absence of the applied dc field as shown in **Figure 4.8**. The standard deviations were calculated from the entire acquired signal from control junctions and separated signals from active junctions, where the dc on signal was analyzed separately from the dc off signal acquired before and after the dc magnetic field was applied.

To analyze the voltage change per binding event, the number of beads per Hall junction must be assessed. In **Figure 4.7b** and **Figure 4.8**, the SEM micrographs indicate the presence of 41 beads on junction (i), 68 beads on junction (ii) and 73 beads on junction (iii). In **Figure 4.8**, the voltage response for the three pads is similar regardless of the number of beads bound at the center of the Hall junction. The largest expected voltage change in the Hall magnetometer will occur for beads directly over the Hall junction, falling rapidly for beads positioned  $> 0.5$   $\mu$ m from the device center (**Figure 4.7d**). Directly over the Hall junction (shaded region **Figure 4.7b**) junction (i) has 8 beads, junction (ii) has 11 beads and

junction (iii) has 12 beads. Calculation of the predicted voltage response as a function of the distance of the bead from the center of the Hall junction is shown in **Figure 4.7d**. For a single 350 nm magnetic bead approximately 272 nm from the Hall device a voltage response of 0.4  $\mu\text{V}$  per bead is expected. The experimental value of  $\sim 0.6 - 0.8 \mu\text{V}$  measured in **Figure 4.7c** following DNA annealing of the target and probe indicates that more than one bead, but not all of the bound beads contribute to the measured Hall voltage. For junction (iii), the result suggests the measured voltage is likely dominated by the 12 beads directly over the center of the Hall junction (southeast corner of the pad in **Figure 4.7d**). Based on the theoretical voltage and the observed voltage in response to DNA annealing in **Figure 4.7c**, a single bead should be detectable.

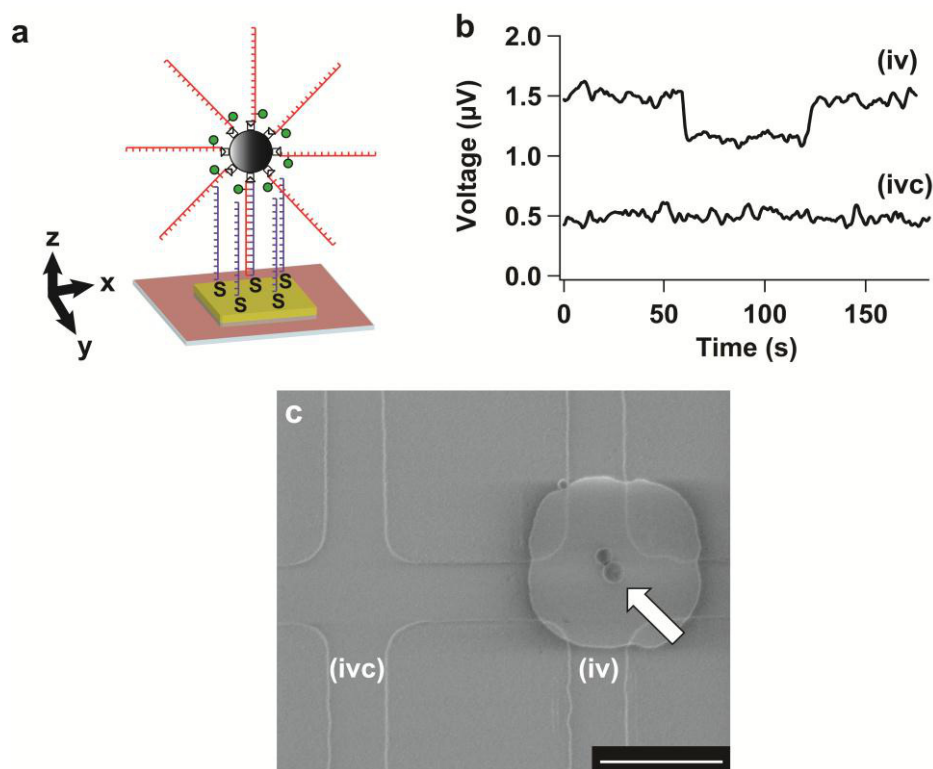


**Figure 4.9:** Sequence-specific two-strand DNA assembly and subsequent Hall detection of a single 344 nm nanobead. **(a)** Pictorial representation of two-strand DNA assembly, where the probe DNA (red) is complementary to the receptor DNA (blue). Hall response data for the active (iv) and control Hall junction (ivc) plotted as Hall voltage versus time, where the drop in Hall voltage corresponds to the presence of a magnetic nanobead **(b)**. SEM was used to confirm only one nanobead contributed significantly to the signal measured in (iv) **(c)**. Scale bar = 2  $\mu\text{m}$ .

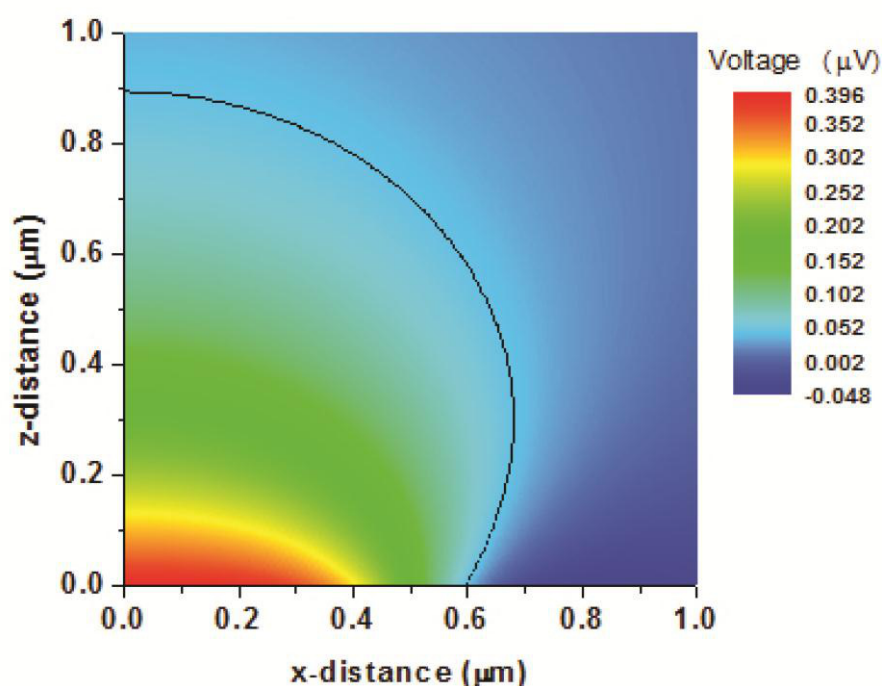


**Figure 4.9:** The theoretical Hall device cross-sectional response for a single 344 nm SPM bead as a function of position from the center of the junction, where red indicates strongest change in voltage, aqua indicates weakest voltage change, and blue indicates a negative voltage readout. The standard deviation of the noise floor for the device is outlined in black for reference.

### 4.3.3 Sensitivity

Although magnetic transduction devices are remarkably sensitive with the observation of single bead detection for a < 500 nm magnetic bead reported for an antibody-antigen sandwich assay based assembly of a magnetic bead on a micron sized Hall device<sup>136</sup> and the multiple bead detection by GMR device<sup>128</sup>, the report of three-strand DNA target detection at the single magnetic bead detection by a Hall device has not been reported to date. Single bead detection is observed for a 35-base pair DNA annealing event onto a Hall device, as shown in **Figure 4.9**. The Hall voltage response (**Figure 4.9b**) and corresponding SEM image (**Figure 4.9c**) for the two-strand annealing event (**Figure 4.9a**) indicates a voltage of  $0.34 \pm 0.03 \mu\text{V}$  ( $0 \pm 0.04 \mu\text{V}$  for control junction) for the two observed beads near the Hall junction. The theoretical response for a single bead over the Hall junction in **Figure 4.9** can be calculated by first fitting the voltage data obtained in **Figure 4.9b** to obtain the following equation:

$$v = \left( \iint_{-0.5}^{0.5} \frac{(2 \times (0.272)^2 - (x+0.34)^2 - (y-0.24)^2)^{\frac{5}{2}}}{((x+0.34)^2 + (y-0.24)^2 + (0.272)^2)^{\frac{5}{2}}} dx dy \right) \times ((344^3) \times (0.119 \times 10^{-8})), \quad (4.1)$$

where  $v$  = the measured voltage, and  $x$  and  $y$  are coordinate distances. Solving the equation yields  $0.34 \mu\text{V}$  in agreement with experimental. The equation can be modified to predict the voltage at the origin by the following equation:

$$v_0 = \left( \iint_{-0.5}^{0.5} \frac{(2 \times (0.272)^2 - (x+0)^2 - (y-0)^2)^{\frac{5}{2}}}{((x+0)^2 + (y-0)^2 + (0.272)^2)^{\frac{5}{2}}} dx dz \right) \times ((344^3) \times (0.119 \times 10^{-8})), \quad (4.2)$$

where the  $x$  and  $y$  coordinates are at the origin. Solving the above equation yields a predicted  $0.39 \mu\text{V}$  at the origin. The above equation can also be solved to predict the voltage readout as a function  $x, y,$  and  $z$ -distance away from the origin as shown in **Figure 4.10**, where a red color on the third axis represents a SPM particle positioned at the center of the device, while a blue color represents a SPM outside the detectable range of the Hall junction. The complete calculations are shown in detail in **Appendix C**. The measured voltage in **Figure 4.9** is consistent with the theoretical value for a single bead, and therefore it is believed that the measured Hall voltage reflects only one of the two beads, since only one of the beads lies within the red zone for the theoretical plot (arrow in **Figure 4.9c**). Improvement of the signal to noise can be achieved by operating the Hall device at higher frequencies; however, it is important to note that the sensitivity of the device can clearly distinguish a single bead binding event from the noise floor by an order of magnitude at the external frequency utilized.

#### 4.3.4 Selectivity and Detection Limits

The limit of detection for DNA in a real sample will reflect the length of DNA (annealing temperature), the sequence of target DNA, and the concentration of DNA present in a milieu of non-target DNA. In the Hall device platform, similar levels should be achievable since the technology is identical. Since the sensitivity will be influenced by the bead size, and the area of the transduction platform, the concentration limit of detection for target DNA was assessed using optical microscopy analysis of the binding of the target DNA onto  $2 \times 4 \mu\text{m}$  patterned GaAs Hall device mimics.

The thermodynamic stability of the three-strand DNA approach has been used for several sensor approaches, including optical, SERS, and colorimetric platforms. In the current study the stability of the three strands is experimentally verified using a gel shift

assay (**Figure 4.4**). In **Figure 4.11a-b**, the binding of the 35-base pair 3-strand target with the appended fluorescently labeled probe sequence and 350 nm magnetic bead to the optical mimic is shown. Inspection of a line-scan for the fluorescence intensity from the probe sequence shows good correlation with the Hall mimic patterns (**Figure 4.11b**). The signal fluctuations do not indicate single bead response as the fluorescein intensity depends on the particle size, number of DNA, labeling efficiency, and focal plane of the microscopy image. Little intensity is observed over the control PEGylated regions surrounding gold pads (identified with black arrows). The discrimination level approaches 10,000 counts above background for selective target DNA binding at the gold pads in buffered solution (**Figure 4.5, Figure 4.11a**).

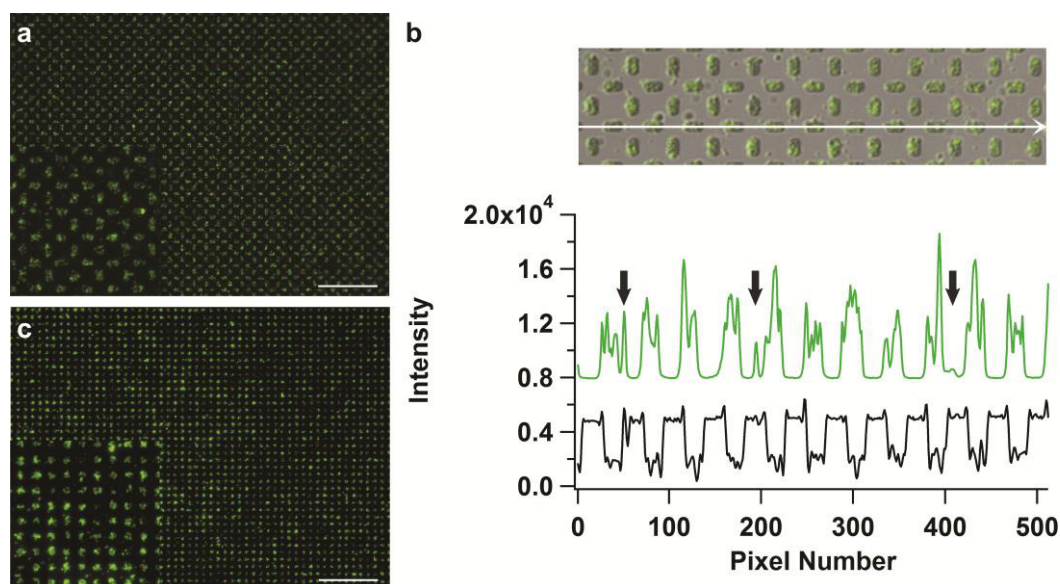


**Figure 4.11:** Three-strand DNA assembly on a mimic array (patterned on a GaAs substrate) for (a) complementary target only and (c) 10 ppm target in non-target DNA. The inlays in the lower left of (a) and (c) are an enlarged portion of (a) and (c), respectively. Scale bars = 50  $\mu\text{m}$ . A line-scan of the wide-field fluorescence microscopy image in (a) showing fluorescein-labeled probe DNA (green) and DIC (black) intensity correlates fluorescence intensity with nanobeads located primarily over gold pads, where the black arrows signify the presence of a small number of non-specifically bound nanobeads (b).

An important measure of device performance is the ability to discriminate target ssDNA in the presence of extraneous (non-complementary) sequences in solution, particularly at low levels of target DNA. The ability to discriminate target DNA in the presence of non-target sequences was analyzed by optical microscopy on 3  $\mu\text{m}$  patterned GaAs Hall device mimics in a buffered solution. Since the sensitivity of the device was

demonstrated to achieve a single bead detection limit ( $0.34 \mu\text{V}$  vs.  $0 \pm 0.04 \mu\text{V}$  noise floor), the choice of an optical mimic to only probe fidelity over a Hall junction allows analysis of the limit of detection for the three-strand annealing process. The presence of fluorescently tagged nanobeads was observed at a concentration of  $364 \text{ pM}$  target DNA, which corresponds to less than two complementary target DNA sequence per  $350 \text{ nm}$  nanobead (**Figure 4.11c**), in a solution containing  $36 \mu\text{M}$  non-target DNA. The measurements equate to detection at the  $10 \text{ ppm}$  level target. Comparison to a mimic array in which the receptor strand is non-complementary to the target strand indicates non-specific DNA binding is not observed (**Figure 4.5**). Although no real biological sample was analyzed, the sensitivity of the device has demonstrated for the first time the detection of a single SPM nanobead specifically assembled via complementary DNA base pairing over a Hall junction suggesting the technology holds substantial promise.

#### 4.4. Conclusions and Future Directions

The device strategy utilizing three-strand DNA assembly on a Hall magnetometer provides a detection platform with high specificity, low limit of detection (single bead), and very high fidelity. Sensitivity of the Hall biosensor is attributable to the properties of the Hall junction and is dependent on the size of the Hall junction, the frequency of the ac field oscillation, the moment of the SPM bead, and the distance of the SPM bead from the Hall junction. In the nanotechnology device, the use of a SPM nanobead does not hinder the specificity of Watson-Crick base pairing for the target nucleic acid as evidenced by sequence-specific DNA hybridization (**Figure 4.5, Figure 4.11**). At the frequency detection employed for the Hall device, the 3-D plot in **Figure 4.10** indicates sensitivity towards longer DNA or more complex architectures is achievable even up to distances approaching  $0.9 \mu\text{m}$  when the SPM bead is located directly over the center of the Hall junction. Higher frequency measurements will decrease the noise levels and therefore increase the sensitivity of the device to the magnetic bead position.

We have demonstrated the successful use of Hall magnetometry to detect a 35-base pair target DNA at the single magnetic nanobead level. Additional studies reaching single nucleotide polymorphism (SNP) detection limits are currently under investigation. Reduction of the dimension of the gold pad and improved registry, as well as bead homogeneity, will improve the overall device performance allowing Hall magnetometry to improve POC

diagnostics. Although the demonstrated Hall platform exhibits single 350 nm bead sensitivity, further optimizing the minimum bead concentration necessary for assembly will ultimately reduce the overall target ssDNA detection limit. Extrapolation of the device to a microarray of selectively labeled Hall sensors could represent a transformative biosensor platform. The parallel Hall device strategy could allow multiple DNA sequences to be simultaneously detected in a biological matrix since each magnetic bead and probe strand can be bar-coded by dye photoluminescence<sup>115</sup> and SPM bead size, since the response will be proportional to the SPM moment. Alternatively, the receptor DNA on the Hall junction can be selectively dip-penned for multi-sequence analysis<sup>146</sup>. By eliminating concerns associated with sample amplification<sup>92</sup> such an array would allow screening for nucleic acid targets of biomedical interest such as pathogens, or disease-related mutations<sup>147, 148</sup>.

## CHAPTER 5

# LIVE-CELL OPTICAL TRACKING OF A NOVEL DYE-LABELED MATRIX METALLOPROTEINASE INHIBITOR (MMPI) IN LNCAP AND LNCAP-MT1-GFP CELL LINES

*Portions of this chapter have been formatted for publication as follows:*

Hira, S.M., Jin, Y., Roycik, M.D., Bosco, D.B., Cao, J., Schwartz, M.A., Strouse, G.F., Sang, Q.X.A. Live-cell optical tracking of a novel dye-labeled matrix metalloproteinase inhibitor (MMPI) in prostate cancer cells. *Manuscript in preparation.*

### 5.1 Introduction

The mystery surrounding both the physiological and pathological roles of matrix metalloproteinases (MMPs) remains a focus of active research<sup>149</sup>. MMPs are a class of zinc containing endopeptidases which play a predominant role in remodeling the extracellular matrix (ECM) needed for cellular migration<sup>150</sup>. Additional roles of MMPs have been linked to cell proliferation, apoptosis, and wound healing, as well as intracellular functions involving cleavage of centrosomes and chromosomal instability<sup>151-154</sup>. Although normal levels of MMPs are needed for healthy, thriving cells, the overproduction of MMPs have been linked to a number of disease states and types of invasive cancers<sup>149, 155-158</sup>. Since cell migration is one of the most fundamental aspects of the development and maintenance of multicellular organisms, MMPs are an obvious target to further understand the intricate web of fundamental cellular structure and function.

There are currently 24 identified MMPs, of which subsets include but are not limited to the matrilysins, collagenases, stromelysins, gelatinases, and membrane-type bound MMPs<sup>155, 159</sup>. Of the 24 MMPs identified, only 23 are relevant to humans<sup>159</sup>. All MMPs contain three conserved regions including a signal sequence, pro-domain, and a catalytic domain. The signal sequence, also known as the pre-domain, consists of 17-20 amino acids largely hydrophobic in nature found at the N-terminus of the protein<sup>160</sup>. The pre-domain directs translation and is cleaved before further enzyme activation. The pro-domain

immediately follows the pre-domain and becomes the new N-terminus after cleavage containing about 80 amino acids<sup>160</sup>. The pro-domain serves as the major regulator of MMP function via a conserved peptide sequence of PRCGXPD known as the “cysteine switch”<sup>161</sup>. The cysteine (C) in the middle of the sequence can coordinate a single Zn<sup>2+</sup> ion located in the catalytic domain maintaining the enzyme in a zymogen state. The catalytic domain consists of 160-170 residues containing three histidine residues that fill the remaining coordination of zinc (4-coordinate)<sup>162</sup>. In addition to these conserved domains found in all MMPs, there are two semi-conserved regions found in all MMPs except MMP-7, MMP-23, and MMP-26 which are a hinge region with a variable peptide sequence rich in proline and a C-terminal hemopexin-like domain<sup>160</sup>. The hinge region contains up to 75 amino acid residues and due to the variability in sequence most likely allows flexibility in the protein structure<sup>160</sup>. The hemopexin-like domain is typically 200 residues and serves an assortment of functions such as substrate recognition and MMP activation<sup>160</sup>. There are also recognition sequences and specific regions found throughout the protein that can be characteristic of particular subclasses of MMPs. The specific regions serve vital roles in the function of MMPs as well as the recycling of MMPs from their designated target location in cellular environments. In the case of gelatinases (i.e. MMP-2, MMP-9), an additional fibronectin (FN) recognition site is found within the catalytic domain to allow for the interaction with particular substrates<sup>158</sup>. Membrane-type MMPs (MT1-MMP, also known as MMP-14) also contain a furin recognition sequence for activation, a trans-membrane tether for plasma membrane targeting, and a cytoplasmic domain coding for intracellular signaling sequence responsible for MMP recycling<sup>163, 164</sup>. Besides the conserved domains and specific recognition regions, synthetically modified MMPs containing the chimeric expression of green fluorescent protein (GFP) have been demonstrated<sup>157, 165</sup>. The addition of GFP was appended to the C-terminal end of the protein after the termination of the cytoplasmic tail. A pictorial description of the conserved and varying domains and recognition sequences is summarized in **Figure 5.1**. It is important to note that although the various domains of MMPs are depicted in a linear arrangement, the secondary and tertiary structure of these proteins is composed of a complex three-dimensional (3-D) structure. An example of the 3-D structure necessary for proper protein function is illustrated through the function of the “cysteine switch” to coordinate a zinc metal ion resulting in the prevention of a cascade of reactive steps leading to MMP activation.

Two MMPs (MT1-MMP and MMP-2) are of particular interest and have become the focus of the experiments performed later in this chapter. MT1-MMP is one of the few MMPs

that is tethered to the plasma membrane and serves roles in ECM remodeling and activation of other MMPs, particularly MMP-2. The latent form of the MT1-MMP is activated by furin in the trans-golgi<sup>164</sup>. Once activated, MT1-MMP is translocated to the plasma membrane to cleave the extracellular matrix and serve its many functions. It has been shown to degrade type I, II, and III collagen, as well as fibronectin substrates<sup>159</sup>. Roles of cleaving centrosomes in the nucleus and even the association with sub-cellular integrins have also been reported in literature<sup>166, 167</sup>. MMP-2 is predominately activated by MT1-MMP and serves a major role in gelatin cleavage in ECM remodeling<sup>158</sup>. Additional activation pathways via other membrane-tethered MMPs (MT2-MMP) and plasmin assisted activation have been reported<sup>159, 168-170</sup>. Due to the intimate connection between MT1-MMP and MMP-2 the two proteins are frequently identified in similar extracellular and intracellular environments.

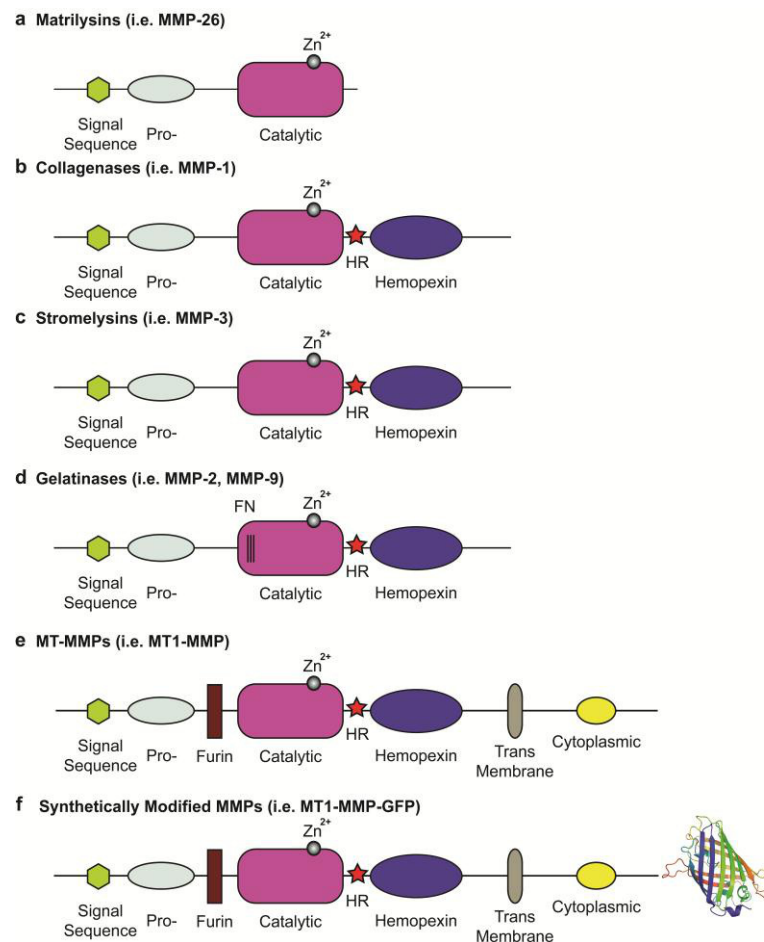


**Figure 5.1:** A pictorial description of the varying domains pertinent to MMPs. Subclassifications of MMPs are shown as follows: Matrilysins (a), Collagenases (b), Stromelysins (c), Gelatinases (d), MT-MMPs (e), and synthetically modified MMPs (f).

Since MMPs serve such a critical role in cellular function through either direct substrate cleavage needed for migration or in multiple signaling processes, natural regulatory molecules are needed to adjust their concentration. There are four tissue inhibitors of metalloproteinases (TIMP) that are naturally found in biological systems with affinities in the pM concentration range that can bind various structural domains and regulate MMP function<sup>158, 159, 162</sup>. The most important and relevant TIMP related to the studies herein is TIMP-2. This natural MMP inhibitor plays a role in conjunction with MT1-MMP in the predominant activation pathway of MMP-2<sup>158, 171, 172</sup>. In particular, TIMP-2 binds the N-terminus of MT1-MMP, which is tethered to the surface of the plasma membrane. The immobilized TIMP-2 is free to bind the hemopexin domain of pro-MMP-2. A second MT1-MMP protein is now able to cleave the pro-domain of MMP-2 and cause activation. After activation Uekita has reported that the MT1-MMP/TIMP-2 complex may be internalized and proposed that endocytosis may aid in the regulation of and promote fully active MMPs at the cell interface<sup>173</sup>. Jiang et al. have shown that the cytoplasmic tail sequence directly affects the amount of active MT1-MMP on the plasma membrane surface available for its membrane bound functions<sup>163</sup>. Even more recently, it has been shown that MT1-MMP is internalized through clatherin mediated endocytosis and can be recycled back to the plasma membrane<sup>174-178</sup>. Although these studies have produced new insights into the function and regulation of MMPs, more research needs to be completed to understand the global view of MMP substrate interactions.

In an effort to regulate MMP activity, a series of synthetic MMP Inhibitors (MMPIs) were developed over the last 30 years for application in the treatment of cardiac diseases and a variety of cancers<sup>179</sup>. In the midst of the forceful push to get potential drugs approved for clinical use, many of the clinical trials were designed poorly and rushed yielding even poorer outcomes. Unfortunately, most have failed clinical trials due to a myriad of toxic and painful side effects or a lack of decreasing MMP overall function<sup>180-183</sup>. A leading candidate in the late 1990's and early 2000's, Marimastat, failed phase III clinical trials due in part to toxic side effects and ineffective treatments when compared to a placebo. The phase III clinical trial report cites musculoskeletal toxicity and associated inferior patient survivability as a possible explanation for the failed clinical trials targeting breast cancer patients<sup>184</sup>. The end results of the report determined that MMPIs and their associated biological effects need to be better understood before additional drug candidates enter clinical trials. Many of the MMPI drug candidates were comprised of hydroxamate functional groups to coordinate the zinc in a bidentate fashion in the heart of the catalytic domain. The strong and potent properties of this

functionality are thought to be behind some of the failed clinical trials where many of these drug candidates did not have any MMP specificity, as well as displayed the propensity to scavenge metal ions in the surrounding biological matrix. The only MMPI approved for clinical use is Periostat, a dental drug administered after scaling and root planning procedures for the treatment of gum disease<sup>155</sup>.

Despite the vast interest in MMPIs as a therapeutic tool, little is known about how MMPIs interact with MMPs in a cellular environment and influence MMP function real-time. Evaluation of inhibitor function has traditionally been accomplished using an enzyme cleavage assay<sup>185</sup>. A multitude of methods have been used to probe MMP function including fluorescence beacons and energy transfer based assays, magnetic resonance imaging (MRI), positron emission tomography (PET), and quantum dot based techniques<sup>186-191</sup>. Unfortunately these techniques suffer from data acquired from ensemble measurements or do not probe MMPI interactions with MMPs. The use of fluorescently labeled peptide substrates to monitor MMP-2 inhibition by MMPIs in vivo was first reported by Bremer et al. in 2001<sup>192</sup>. While the in vivo animal study yielded unprecedented optical imaging of active MMPs functioning around tumors, the details of MMPI interactions with MMPs were not probed. Seven years later Faust et al. appended a fluorophore to a barbiturate based MMPI as a photoprobe for imaging MMPs in vitro<sup>193</sup>. The published results conclude that the selective labeling of the surface of A-673 cells by the dye labeled MMPI was due to the interaction of the MMPI with MMP-2 and MMP-9 secreted by the cells. In depth optical analysis of the association of MMPIs with MMPs in a cellular environment were not performed. More recently in 2009, Faust et al. probed the labeling of MMP-2 and MMP-9 in cryostat tumor sections with a dye labeled commercially available hydroxamate based MMPI showing selective association to tumors, but did not probe cellular interactions<sup>194</sup>. Finally a study accomplished by auf dem Keller et al. in 2010 modified Marimastat with <sup>18</sup>F for PET analysis<sup>195</sup>. Also described within this study was the appendage of a fluorescent marker to the target inhibitor to confirm association of the modified Marimastat with the plasma membrane. The FITC labeled Marimastat was incubated with MDA-MB-231 cells stably expressing MT1-MMP at a concentration of 10  $\mu$ M for 12 hours cells, washed, and were fixed prior to imaging. Similar to Faust et al, auf dem Keller et al. report the surface labeling of the cancerous cells<sup>193-195</sup>. It is important to note that none of the aforementioned literature references observed or suggested inhibitor internalization into cells. To date, an in depth analysis of the interaction of MMPIs with MMPs under real-time conditions immediately after the addition of an MMPI has not been reported.

The design of novel MMPIs are still being explored for potential therapeutic applications<sup>196-201</sup>. In an effort to identify and curb some of the apparent issues associated with previous MMPI targets, the design of YHJ-8-91 based off of YHJ-7-52 revolved around multiple criteria to enhance binding of the MMPI to the catalytic domain of MT1-MMP<sup>201</sup>. First, the implementation of a thiol-based zinc binding group was thought to decrease the binding affinity towards erroneous metal ions because it is not a bidentate chelator, while still maintaining a significant binding affinity for specific interactions<sup>199</sup>. Second, the use of a sulfonamide in the target inhibitor has been shown to be critical in MMPI drug design, as this functionality can hydrogen bond with the enzyme substrate and add stability to the catalytic interaction<sup>199</sup>. Third, the additional use of a diphenyl ether to interact with the S1' binding pocket should allow for enhanced individual MMP specificity. It has been previously shown that the molecular compounds interaction with the depth of the S1' pocket can result in specificity<sup>202</sup>. Combining all of these criteria may result in an MMPI that can target a relatively small subset of MMPs in an effort to surpass the previous clinical trial failures. To visualize the activity of MMPIs in a cellular environment, the appendage of a fluorophore on a flexible linker outside of the molecular binding pocket was undertaken. The fluorescent dye was chosen based on the ability to efficiently excite with a 561 nm laser source and emit photons in the red region of the color spectrum in an attempt to limit spectral bleed-through on our instrumental microscope platform. Also, the dye was chosen to exhibit favorable spectroscopic properties of quantum yield and stability while increasing molecular solubility of the target MMPI<sup>203</sup>. In addition to the target MMPI design, the use of a MMPI control that retains the S1' specificity, but lacks a thiol for zinc coordination and instead utilizes a hydroxyl functionality provides a sophisticated control for precise validation of molecular specificity (YHJ-7-82). It has previously been shown that YHJ-7-52 has a  $K_i$  of 2.1 nM for MT1-MMP and 2.2 nM for MMP-2 as shown through a fluorescent enzyme cleavage assay<sup>201</sup>. The YHJ-7-82 control exhibited a  $K_i$  of 10  $\mu$ M for MMP-2 and was offscale for MT1-MMP<sup>201</sup>. A final control rendering the Lissamine rhodamine B sulfonyl chloride unreactive by reacting the dye with propyl amine will be used to probe the possibility of dye enhanced cellular interactions. The chemical structures of the target inhibitor and the two controls are shown in **Figure 5.2**. The target inhibitor design and subsequent controls will be predominately evaluated on LNCaP-MT1-GFP cells<sup>165</sup>. This stably, over-MT1-MMP-expressing cell line was chosen as a model cell line due to the nature of this epithelial cell line to be present on the very onset of cancerous activity and the MT1-GFP chimera provides a convenient way to monitor the enzyme real-time in its native environment.

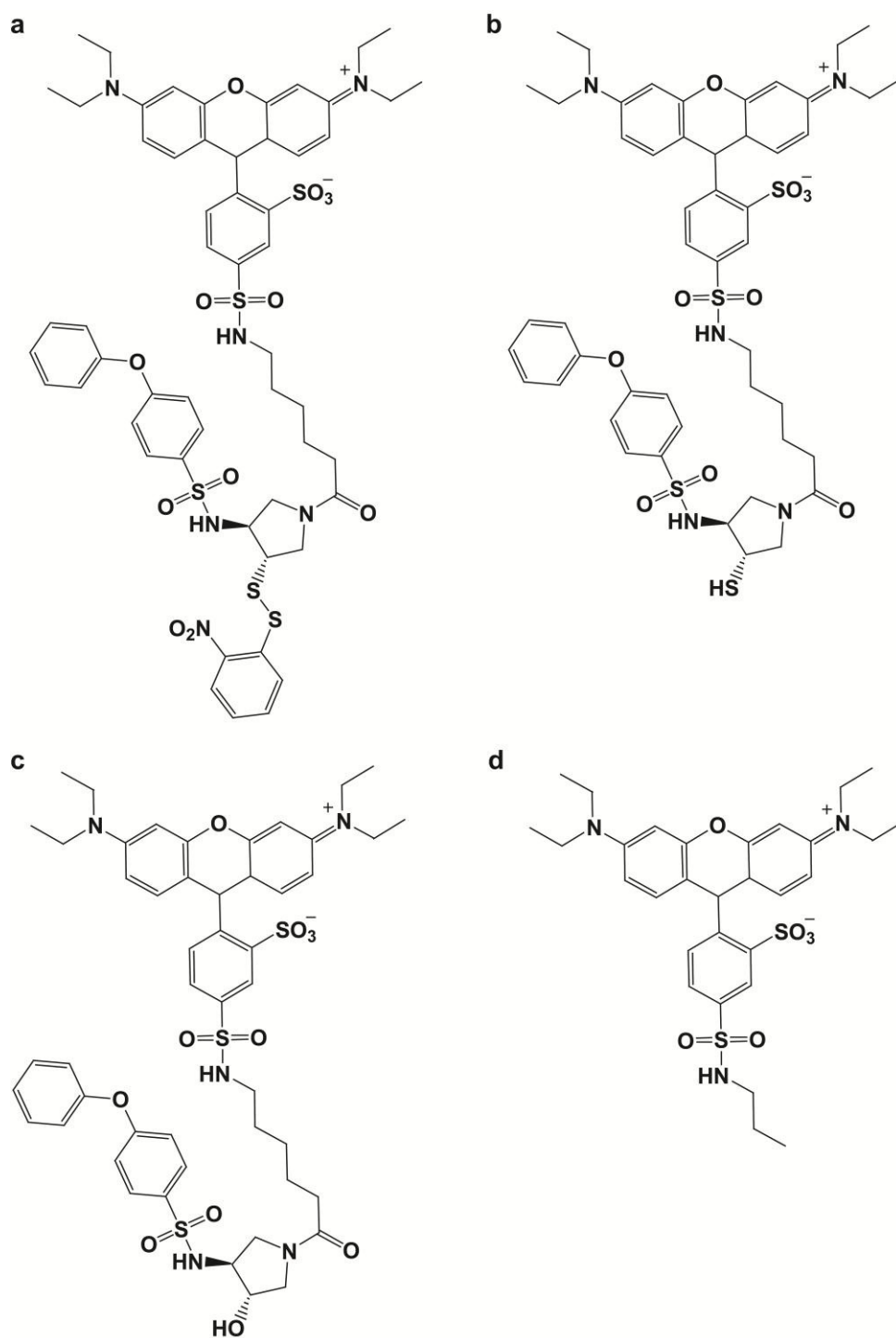


**Figure 5.2:** The chemical structures of YHJ-8-91 in protected/inactive (a) and deprotected/active (b) forms, YHJ-8-89 (c), and C<sub>3</sub>Dye (d).

The ability to optically track MMPs and follow the interaction real-time has the potential to gain new insights on how this class of evasive enzymes functions in extra-cellular and intracellular environments. It has been shown that MT1-MMP is involved in a complex recycling pathway to ensure cells maintain a functional active state on the plasma membrane.

We hypothesize that the use of dye-labeled MMPIs may be used to track the activity of MMPs within their respective environment. The experiments and subsequent results described herein are the first attempt at gaining new insights on how MMPIs interact with MMPs at the cellular level under real-time conditions using a dye-labeled inhibitor.

## 5.2 Syntheses of Dye Labeled Target MMPI and Controls

### 5.2.1 Synthesis of Disulfide Protected Dye Labeled Target MMPI

YHJ-7-52, previously synthesized in the research laboratory of Martin A. Schwartz by Yonghao Jin, was coupled to an amine reactive dye through a sulfonamide coupling reaction as shown in **Figure 5.3**. YHJ-7-52 was reacted with 6.26 mg of Lissamine rhodamine B sulfonyl chloride and triethylamine (TEA) in a 1.2:1:6 mole ratio in dry DMF under nitrogen for 2 days. The TEA and DMF were evaporated under hard vacuum leaving the product and unreacted dye behind. Thin layer chromatography (TLC) was carried out on reverse phase silica plates in a 10% methanol/ 90% methylene chloride solution as shown in **Figure 5.4**. The mobility shifts from left to right are Lissamine rhodamine B, reaction mixture, YHJ-7-52/ TEA, YHJ-7-52, Lissamine rhodamine B incubated in a 50:50 DMF/H<sub>2</sub>O solution for 24 hours. The TLC plates were pumped down under hard vacuum to limit smearing caused from DMF. A clean, isolated product band can be easily separated on reverse phase silica gel plates. The incubation of Lissamine rhodamine B sulfonyl chloride in 50:50 DMF/H<sub>2</sub>O was to determine if a chromatographic shift occurred resulting from the reaction of the sulfonyl chloride with water. The inhibitor-dye conjugate was isolated using reverse phase column chromatography using 10% methanol/ 90% methylene chloride. The separation of the inhibitor-dye complex from free dye was not as clean as TLC. Only a very small amount of crude mixture (< 1 mg) was able to be loaded at any one time, where ~150  $\mu$ g was isolated. Excess loading of crude material resulted in little to no mobility shift between the product and side-products or reactants making column chromatography difficult. Due to the difficulty in column purification loading, wet addition and dry loading were attempted, yielding no difference in separation outcomes. Characterization of the product was accomplished using nuclear magnetic resonance (NMR) and mass spectrometry analysis, where the mass spectrogram is shown in **Appendix D**. The mass spectrometry analysis confirmed a dominate peak at 1157.4  $\text{g}\cdot\text{mol}^{-1}$ . The  $K_i$  of the dye-labeled thiolated (active) inhibitor was experimentally determined to be 60 nM by a fluorescent enzyme cleavage assay.

All subsequent synthesis of the dye-labeled disulfide protected inhibitor was performed by Yonghao Jin in the research laboratory of Martin A. Schwartz (designated YHJ-8-91) and was purified using reverse phase high performance liquid chromatography (HPLC). Purified samples were evaporated to dryness and stored in the absence of light at -30 °C until cellular studies were performed.

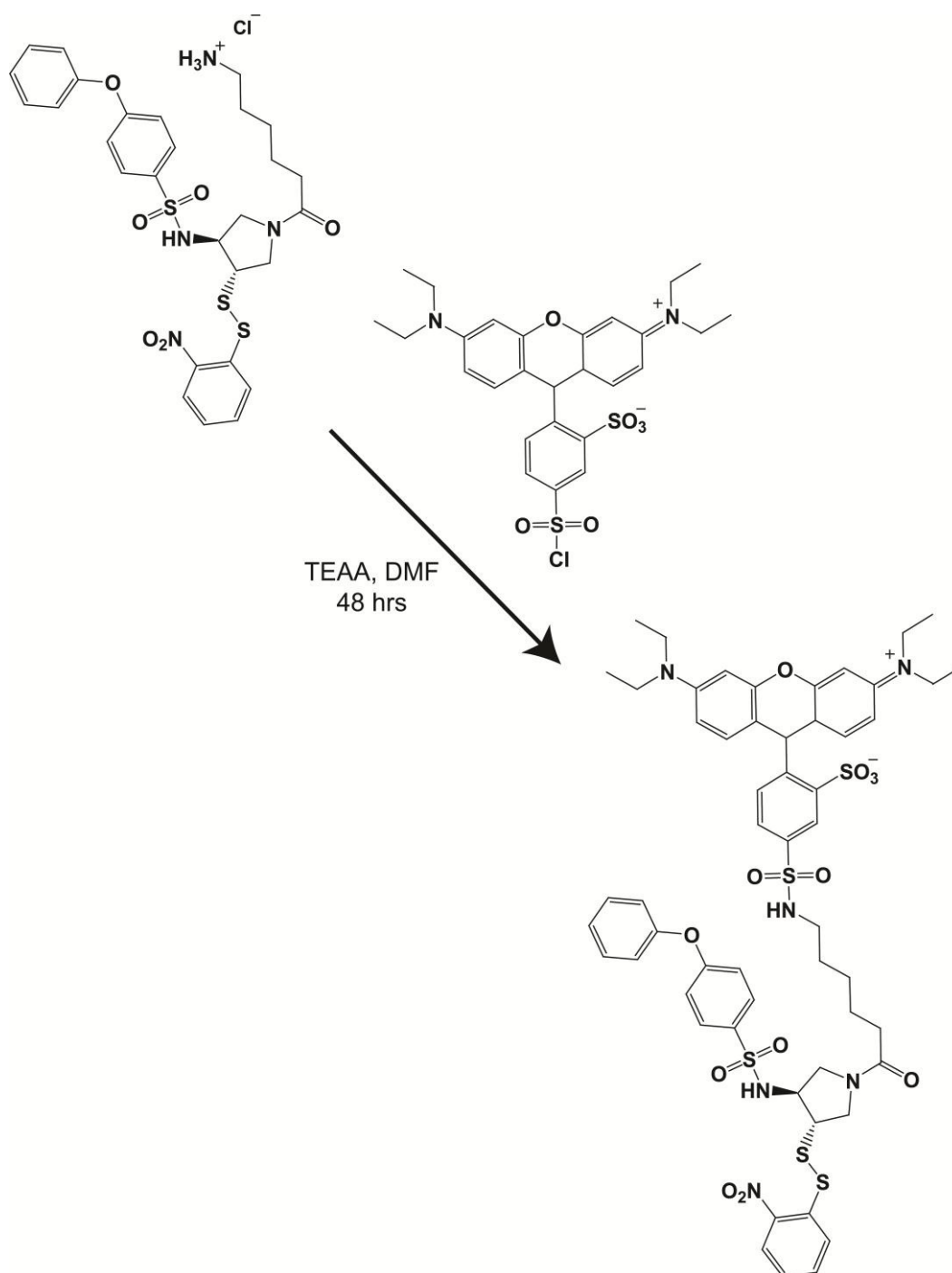


**Figure 5.3:** The reaction scheme for the synthesis of disulfide protected inhibitor.

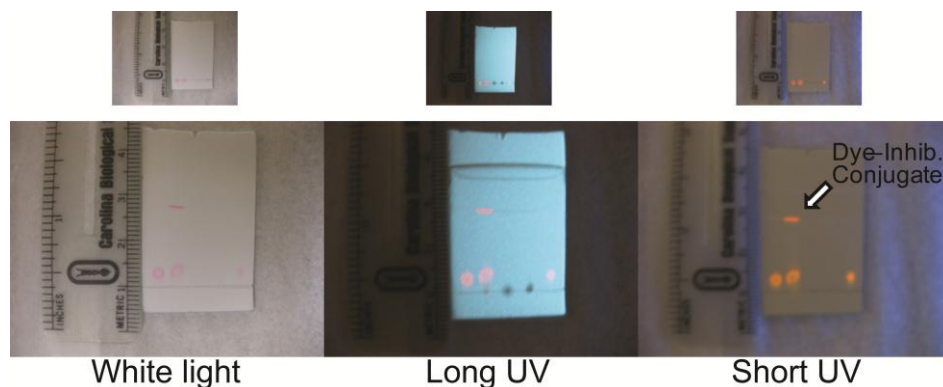


**Figure 5.4:** Thin Layer Chromatography results showing the difference in mobility between disulfide protected inhibitor and unreacted Lissamine rhodamine B under white light and UV illumination (bottom). The spotted reactants and reaction mixture are shown before solvent elution (top).

### 5.2.2 Syntheses of YHJ-8-89 and C<sub>3</sub>Dye Controls

Additional disulfide protected inhibitor (designated YHJ-8-91) and two controls (YHJ-8-89, C<sub>3</sub>Dye) were synthesized by Yonghao Jin in the research laboratory of Martin A. Schwartz to determine the molecular specificity of the inhibitor compounds. Lissamine rhodamine B sulfonyl chloride was purchased from Invitrogen and reacted with YHJ-7-82 in a similar fashion as the disulfide protected inhibitor, YHJ-8-91, to synthesize YHJ-8-89, a hydroxide control lacking the zinc binding group (ZBG). In addition, Lissamine rhodamine B sulfonyl chloride was reacted with propyl amine to determine if the MMPI-cell interactions were driven by the properties of the fluorescent dye. Additional YHJ-8-91, as well as YHJ-8-89 and C<sub>3</sub>Dye controls were purified via reverse phase HPLC and characterized using mass spectrometry and NMR (NMR shown in **Appendix E**). Samples were stored as a solid in the absence of light at -30 °C until cellular studies were performed.

### 5.3 Quantification of Target MMPI and Controls

The amount of inhibitor target or controls for subsequent cellular studies was quantified using absorption and the application of Beer's Law ( $A = \epsilon bc$ ). The chemical structures of the target MMPI and controls with corresponding offset absorption spectra are shown in **Figure 5.5**. A stock solution of the target molecule (or one of the two controls) was made using HPLC grade methanol and absorption was taken using a Carey 50 Bio UV-Visible spectrophotometer. 5  $\mu$ L of stock solution was added to 50  $\mu$ L of methanol in a

quartz cuvette (baseline corrected). The concentration was determined using a published extinction coefficient,  $\epsilon$ , of  $88,000 \text{ M}^{-1}\text{cm}^{-1}$  at  $568 \text{ nm}$ <sup>204</sup> for the fluorescent dye and a path length of  $0.3 \text{ cm}$ . The same  $\epsilon$  was used for the dye labeled MMPI and controls because any modification to the original dye molecule did not involve the conjugated ring system responsible for fluorescence. The appropriate amount of material for cellular studies was aliquoted from the stock solution and allowed to evaporate at RT. In the case of  $10 \text{ nM}$  samples used in the following studies a second dilution was performed to obtain the appropriate quantities for dilute cellular experiments. The aliquoted sample was stored in the absence of light at RT and used within days of obtaining the concentration to limit any possible degradation.

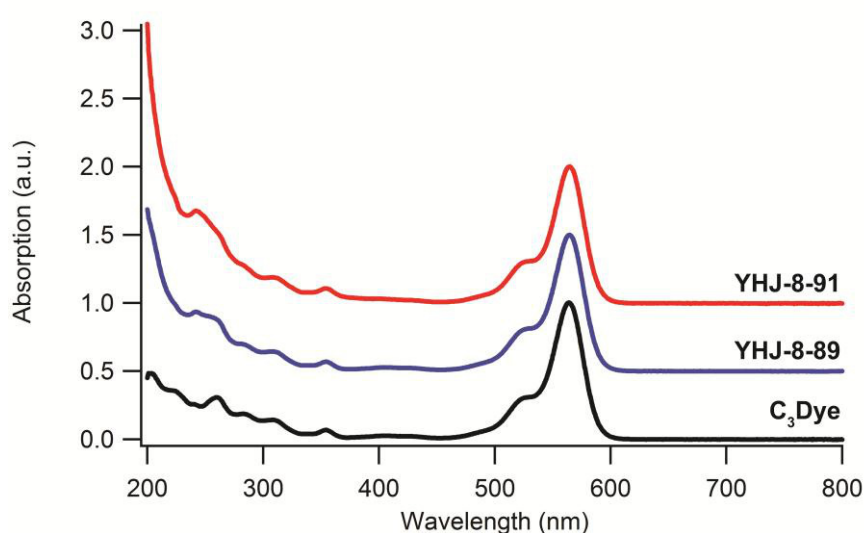


**Figure 5.5:** The normalized offset absorption spectra of YHJ-8-91, YHJ-8-89, and C<sub>3</sub>Dye.

## 5.4 Microscopy Details

Optical microscopy characterization was used to optically track the selective uptake of MMPI's into LNCaP cells, provided by the research laboratory of Jin Cao and cultured in the laboratory of Q.X. Amy Sang by M. Dru Roycik, and follow the time dependent uptake. LNCaP epithelial cells were chosen as a model cell line for the following studies focused on MMP-2, MMP-9, and MT1-MMP because that is where the MMPs originate. The use of the over-expressing MT1-GFP chimera cell line variant allows the membrane bound MT1-MMP to provide a natural plasma membrane stain to monitor molecular uptake and probe colocalization of inhibitors with MT1-MMP<sup>165</sup>. The inhibitor and controls were dissolved in

20  $\mu$ L of neat ethanol and deprotected at RT for 75 minutes with 1 mM tris(2-carboxyethyl)phosphine (TCEP) and 3 mM sodium hydroxide solutions. Laser Scanning Confocal Microscopy (LSCM) characterization of the target MMPI and controls were acquired with an inverted Nikon TE2000-E2 Eclipse C2Si spectral confocal microscope (Nikon Instruments Inc., Melville, NY, USA) equipped with a Nikon CFI Plan Apochromat 40X objective (NA 0.95, 0.14 mm WD), condenser (NA 0.52), differential interference contrast (DIC), and a transmitted light detector (TLD). A 488 nm argon ion laser was used to excite GFP and MT1-GFP chimera constructs (emission filter 515/30), a 561 nm diode pumped solid-state laser was used to excite Lissamine rhodamine B (emission filter: 605/75), and a 404 nm diode laser was used to excite Hoechst 34580, a minor groove intercalating fluorescent dye to observe the location of DNA (emission filter: 450/35). Imaging was generally acquired at a rate of 18.96  $\mu$ s using a 33.3  $\mu$ m pinhole. Spectral confocal at 5 nm resolution was used to verify that the observed fluorescence was attributed to the spectral profile of Lissamine rhodamine B and not due to any spectral or scattering artifacts. Laser powers were kept constant during the duration of an experiment and kept the same when comparing between experiments. The cells were plated in either glass bottom dishes or glass bottom 6-well plates and placed into a Pathology Devices live cell stage-top incubator at 37  $^{\circ}$ C, 5% CO<sub>2</sub>, and 75% humidity for the duration of an experiment. The data were analyzed using Nikon NIS Elements software. Multi-channel data acquisition utilized a frame lambda technique in which individual laser passes were made to image in respective channels to limit microscopic artifacts stemming from fluorescence bleed-through. Although spectral-bleed through is eliminated, slight x-y-z spacial shifts were observed from the time lag involved in multiple scans. This shift makes spectral colocalization studies qualitative. Attempts at normal LSCM were made to limit x-y-z spacial shift at the expense of spectral bleed through between GFP largely localized in the green channel into the red channel.

### **5.5 Cellular Uptake of Target MMPI into LNCaP-MT1-GFP and LNCaP-GFP Cell Lines**

The cellular uptake of MMPIs into LNCaP-MT1-GFP and LNCaP-GFP expressing cells was investigated. The initial study focused on monitoring the interaction and uptake of 10  $\mu$ g of deprotected dye-labeled thiolated inhibitor into LNCaP-MT1-GFP cells over the span of 24 hours under live cell microscopy conditions in an optical dish. The observed uptake of the dye-labeled thiolated inhibitor over time as shown in **Figure 5.6** was originally

unexpected and deviated from previously published literature, where the highest concentration of MMPs are located on the surface and the surrounding ECM. The DIC TLD images and individual contributions from the green color from the MT1-GFP chimera construct mainly tethered to the plasma membrane and the red color from the Lissamine rhodamine functionality on dye-labeled thiolated inhibitor, as well as the overlay are shown in **Figure 5.6a-d** for clarity. Red fluorescence originating from the fluorophore labeled MMPI is observed for every cell within the shown micrograph and localized in discrete packages with similar sizes. A digital zoom of one of the cells clearly shows that dye-labeled thiolated inhibitor is faintly located throughout the cell periphery and is being concentrated at the polar end of the cell in the region of the invadopodia (**Figure 5.6e-f**). To ensure that dye-labeled thiolated inhibitor was located within the plasma membrane of the cells, a series of images were acquired at fixed intervals and rendered into a 3-D projection as shown in **Figure 5.6g**. The uptake of dye-labeled thiolated inhibitor (red) into LNCaP-MT1-GFP cells (green) is clearly shown. Although the intensity of both MT1-GFP and the dye-labeled MMPI are intense at the polar end of the cell, attempts at spectral co-localization were unsuccessful. It is important to note that LNCaP-MT1-GFP also produce additional MMPs including but not limited to MMP-2 and MMP-9.

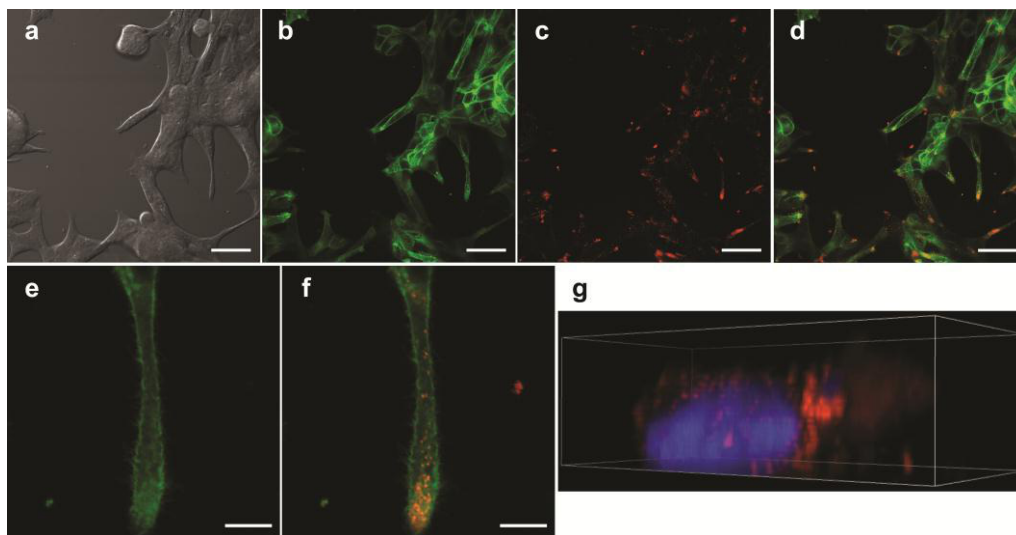


**Figure 5.6:** The cellular uptake of dye-labeled thiolated inhibitor in LNCaP-MT1-GFP. LSCM micrographs of TLD-DIC (**a**), MT1-GFP (**b**), rhodamine signature (**c**), and an overlay of MT1-GFP/rhodamine signature (**d**) are shown ~ 6.5 hrs post incubation. An electronic zoom of a portion of (**a-d**) is shown depicting MT1-GFP (**e**) and MT1-GFP/rhodamine signature overlay (**f**). The 3-D reconstruction image of LNCaP-MT1-GFP cells with internalized dye-labeled thiolated inhibitor after 24 hr post incubation is shown as a Hoechst 34580 (blue)/rhodamine signature (red) overlay (**g**). Scale bars (**a-d**) = 50  $\mu\text{m}$ , (**e-f**) = 10  $\mu\text{m}$ .

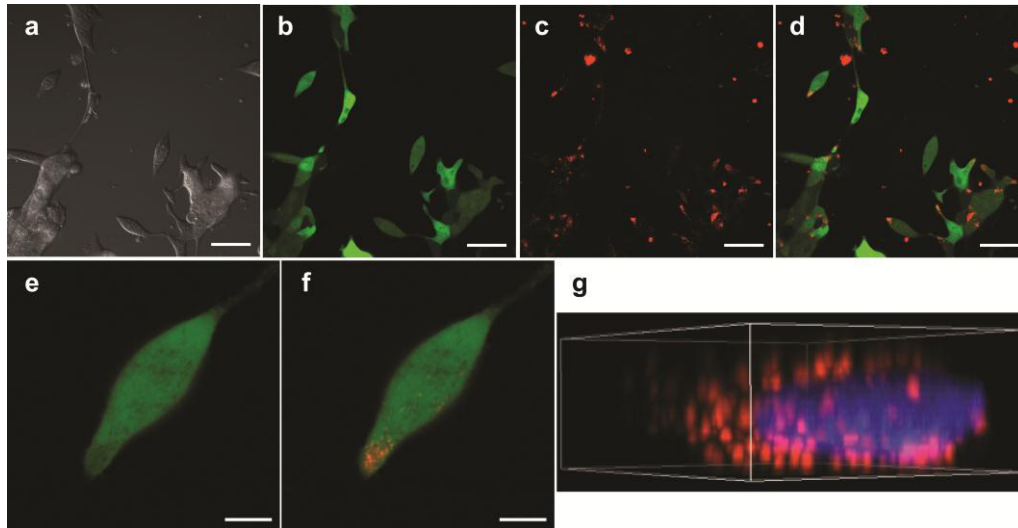


**Figure 5.7:** The cellular uptake of dye-labeled thiolated inhibitor in LNCaP-GFP. LSCM micrographs of TLD-DIC (**a**), GFP (**b**), rhodamine signature (**c**), and an overlay of GFP/rhodamine signature (**d**) are shown 4.25 hrs post incubation. An electronic zoom of a portion of (**a-d**) is shown depicting GFP (**e**) and GFP/rhodamine signature overlay (**f**). The 3-D reconstruction image of LNCaP-GFP cells with internalized dye-labeled thiolated inhibitor after 24 hr post incubation is shown as Hoechst 34580 (blue)/rhodamine signature (red) overlay (**g**). Scale bars (**a-d**) = 50  $\mu\text{m}$ , (**e-f**) = 10  $\mu\text{m}$ .

An additional study was conducted on LNCaP-GFP expressing cells. This cell line, from the same parental cell line as LNCaP-MT1-GFP, produces GFP throughout the entire cell that is not linked to MT1-MMP<sup>165</sup>. Literature precedence based on Western blots and zymograms have shown that LNCaP cells do not contain appreciable levels of MT1-MMP, which also affects the amount of active MMP-2 that is also present<sup>165, 205, 206</sup>. As LNCaP cells transition to a more aggressive state over time, the expression of MT1-MMP increases. On the contrary, LNCaP cells produce measureable quantities of MT2-MMP<sup>206</sup>. The delivery of 10  $\mu\text{g}$  of dye-labeled thiolated inhibitor was tracked over the course of 24 hours. Analogous to the data collected on LNCaP-MT1-GFP, the MMPI was internalized and trafficked toward the polar end of the cell over time as shown in **Figure 5.7**. The 3-D reconstruction image shown in **Figure 5.7g** confirms that the dye-labeled thiolated inhibitor is present within the confines of the plasma membrane. Similar experimental observations between two differently MMP expressing cell lines were observed. One of the possible explanations for the uptake and localization of dye-labeled thiolated inhibitor into both LNCaP-MT1-GFP and LNCaP-GFP cell lines are that the dye-labeled MMPI is targeting other MMPs other than the originally targeted MT1-MMP, MMP-2, MMP-9. Other possible causes for cell association

may stem from the Lissamine rhodamine B dye functionality causing non-specific uptake, unusually high concentration effects, MMPs from media, or a non-MMP related mechanism.

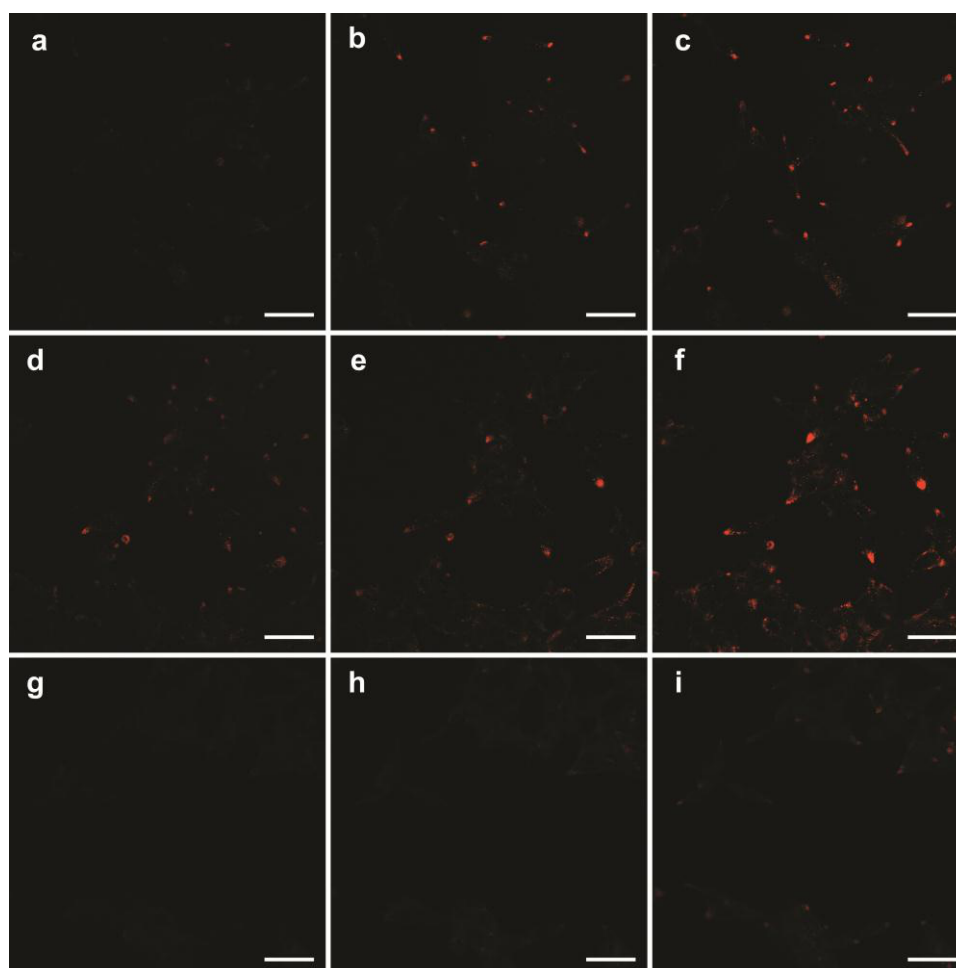


**Figure 5.8:** The qualitative cellular uptake of YHJ-8-91 (a-c), YHJ-8-89 (d-f), and C<sub>3</sub>Dye (g-i) at 1 hr (a,d,g), 2 hr (b,e,h), and 3 hr (c,f,i) post material incubation. Scale bars = 50  $\mu$ m.

### 5.6 Cellular Uptake of YHJ-8-91, YHJ-8-89, and C<sub>3</sub>Dye into LNCaP-MT1-GFP on a Static Region

The qualitative comparison of cellular uptake of YHJ-8-91 (10  $\mu$ g), YHJ-8-89 (10  $\mu$ g), and C<sub>3</sub>Dye (~7  $\mu$ g) into LNCaP-MT1-GFP expressing cells was investigated on a static region to determine if the Lissamine rhodamine B dye is responsible for aiding cellular uptake. The following studies were conducted using live-cell microscopy analysis on a static region of the optical dish over a 4 hour time span. Images were acquired at 15 min intervals. Since varying amounts of material were added, concentrations between all three compounds

are not equal; therefore, a direct comparison of the amount of material uptake by cells can not drawn. Qualitatively, the outcome of positive internalization under the current microscopy conditions, as well as the translocalization of material after uptake can still be assessed at the concentration used for each compound. The qualitative uptake for YHJ-8-91, YHJ-8-89, and C<sub>3</sub>Dye into LNCaP MT1-GFP cells at 1, 2, and 3 hrs post incubation is shown in **Figure 5.8**. Both YHJ-8-89 and YHJ-8-91 were clearly internalized within 3 hours post incubation. In addition, the C<sub>3</sub>Dye was observed to be associated with LNCaP-MT1-GFP, albeit at a lower observed intensity. The microscopy results from this study resulted in the need for a much lower concentration (nM) of MMPI and controls to be investigated to exclude artifacts from high concentrations (μM).

### **5.7 Quantification of the Cellular Uptake YHJ-8-91, YHJ-8-89, and C<sub>3</sub>Dye into LNCaP-MT1-GFP after 6 Hours of Incubation at 10 nM**

The direct quantitative comparison of cellular uptake between YHJ-8-91, YHJ-8-89, and C<sub>3</sub>Dye into LNCaP-MT1-GFP expressing cells was investigated after 6 hours of incubation. The compounds were aliquoted from a single stock solution using Beer's Law and deprotected as described in **Section 5.3** to achieve a final cellular concentration of 10 nM in the imaging environment. The experiments were conducted using 6-well uncoated glass plates from Mat-Tek, where each well contained ~300,000 cells. All three compounds were probed in duplicate within a single experiment and repeated three times over three consecutive days. The incubation of compounds were staggered within an individual experiment by 10 minutes to allow enough time to image each compound at the same time point. The LSCM settings were identical over the time course of this study to allow for direct comparison between compounds. Although the focal plane had to be adjusted for each well, the chosen focal plane of interest was close to the bottom of the cell. Micrographs were taken at two time points, 4 and 6 hours post compound incubation. Unlike other microscopy analysis shown thus far, the media containing the compound was removed at 5.5 hours and the cells were stained with Hoechst 34580 in an effort to identify the number of cells within an individual image to address concerns from previous studies. To minimize cell detachment from the glass surface, Hoechst 34580 was not removed from solution after staining (Hoechst 34580 exhibits a 2-4 fold increase in fluorescence intensity upon intercalation allowing background signal to be minimized). The 6 hour time point was imaged in PBS buffer to

allow for the staining of nuclear DNA. Representative micrographs for YHJ-8-91, YHJ-8-89, and C<sub>3</sub>Dye are shown in **Figure 5.9**. For clarity, the individual channels for DIC acquired with a TLD, the blue channel staining for the nucleus of the cells, the green channel containing signal from MT1-GFP, and the red channel containing signal from the Lissamine rhodamine B contained within YHJ-8-91, YHJ-8-89, and C<sub>3</sub>Dye, as well as overlays for comparison. The images shown in **Figure 5.9** clearly show a difference in cellular uptake between the three different compounds, where cells treated with YHJ-8-91 dominates in total amount of Lissamine rhodamine B signal. Both YHJ-8-91 and YHJ-8-89 show varying degrees of uptake. No appreciable localized C<sub>3</sub>Dye signal indicates that C<sub>3</sub>Dye does not transverse the plasma membrane at 10 nM under the current microscopy conditions.

Quantitative analysis of cellular uptake was accomplished by applying a threshold of 125 counts to the red channel and excluding all counts below the set threshold. The threshold was determined based on eliminating random counts outside of cells in the surrounding media. The total fluorescence intensity for an individual micrograph was calculated by dividing by the total number of cells partially or entirely contained within an image. A combination of the TLD-DIC image, blue channel, green channel, and red channel was utilized to assess the total number of cells within a micrograph. Contributions from compounds outside of the cell were not observed under these conditions, where the measured signal intensity is representative of cellular uptake. The data was pooled together ( $n \geq 20$ ) and evaluated for each compound at the 6 hour time point. A graph of the three compounds efficacy for uptake is shown in **Figure 5.10**. It is clearly shown that YHJ-8-91 was endocytosed at 348.9 fold higher than the C<sub>3</sub>Dye control and 6.6 fold higher than the YHJ-8-89, which lacks an efficient zinc binding group. It is important to emphasize that the only difference between the target C<sub>3</sub>Dye-labeled thiolated inhibitor and the dye labeled hydroxide control is a single functional group. The use of a molecular control of this specificity depicting a 6.6 fold increase for the target MMPI over a control in a biological matrix is remarkable. The observation that the dye control did not efficiently cross the plasma membrane eliminates concerns that the dye enhances uptake at relatively low concentrations. This characteristic may not hold at high cellular concentrations. The statistical difference between the amount of activated thiol and the hydroxide control uptaken into LNCaP-MT1-GFP cells suggests good selectively since the difference between molecules can be attributed to a single chemical functional group. The measureable uptake of YHJ-8-89 may be attributed to S1' interactions or some other non-specific molecular interaction with the enzyme substrate. The statistical analysis of **Figure 5.10** is shown in **Appendix F**. The 3-D

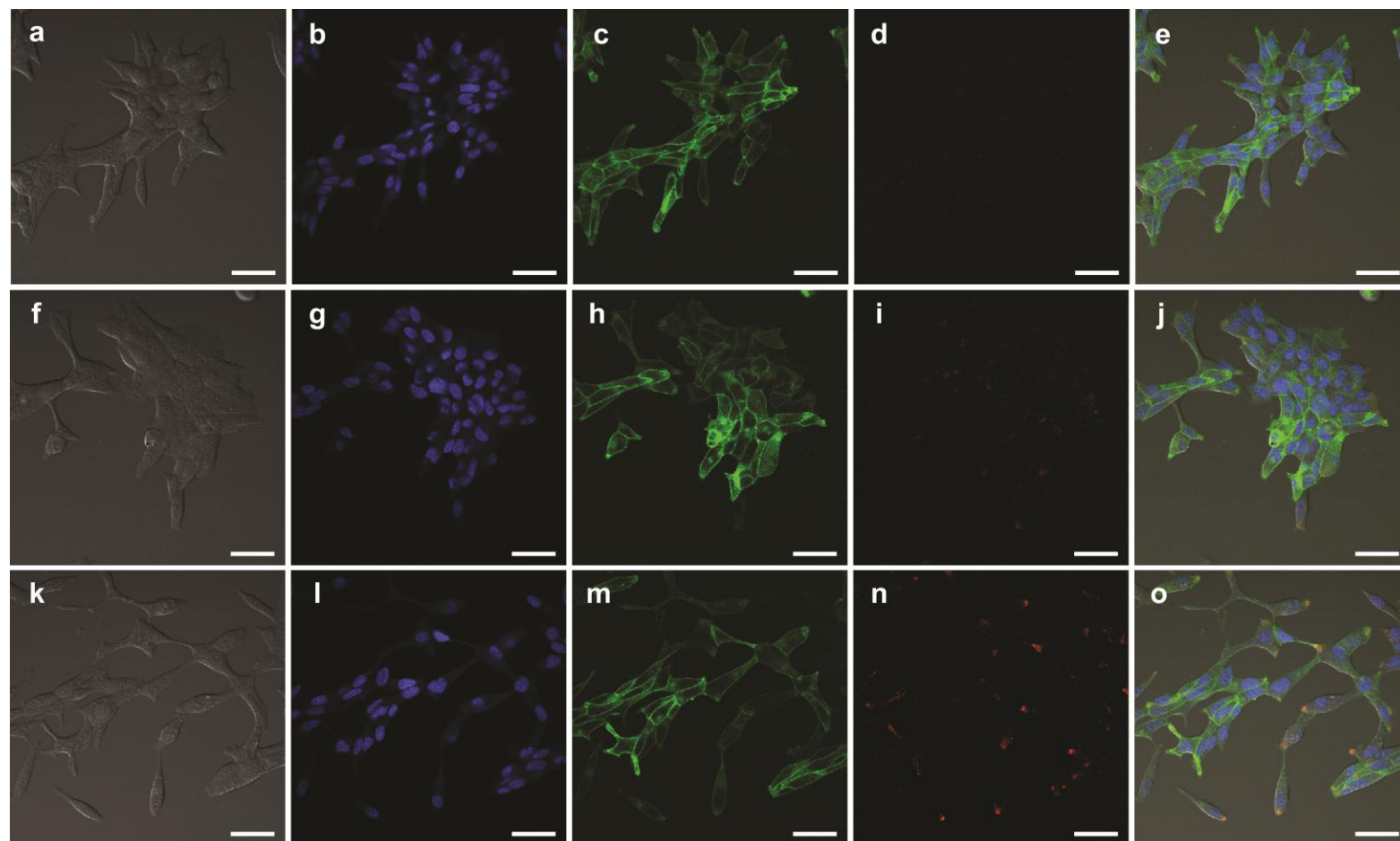


**Figure 5.9:** LSCM micrographs showing cellular uptake of YHJ-8-91 (**a-e**), YHJ-8-89 (**f-j**), and C<sub>3</sub>Dye (**k-o**) into LNCaP-MT1-GFP cells 6 hrs post incubation. The individual channels for TLD-DIC (**a,f,k**), Hoechst 34580 (**b,g,l**), MT1-GFP (**c,h,m**), YHJ-8-91 (**d**), YHJ-8-89 (**i**), C<sub>3</sub>Dye (**n**), and overlay TLD-DIC, Hoechst 34580, MT1-GFP, and respective compound (**e,j,o**). Scale bars = 50  $\mu$ m.

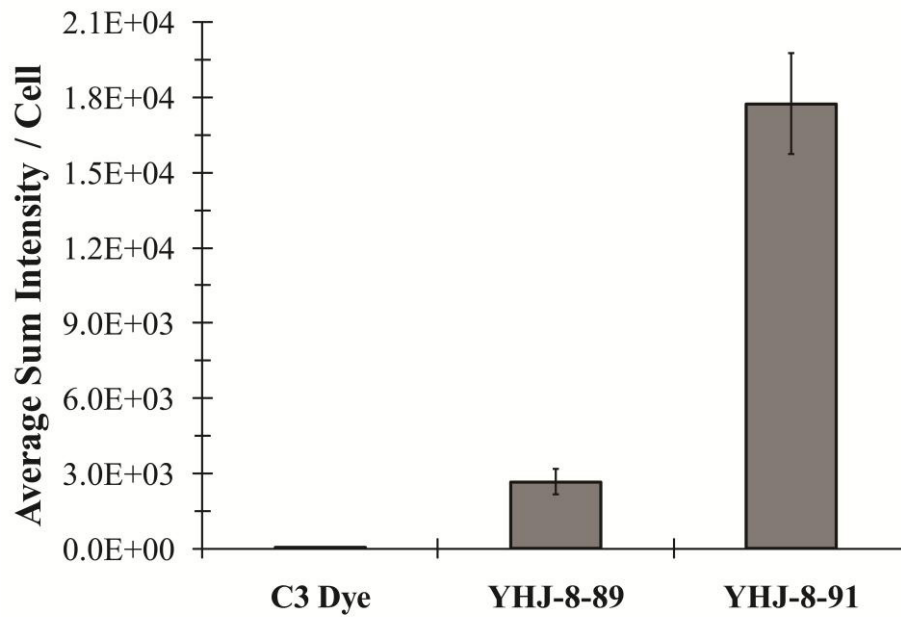


**Figure 5.10:** A graph of the quantitative uptake of YHJ-8-91, YHJ-8-89, and C<sub>3</sub>Dye in LNCaP-MT1-GFP cells 6 hours post incubation. Error bars represent standard error.

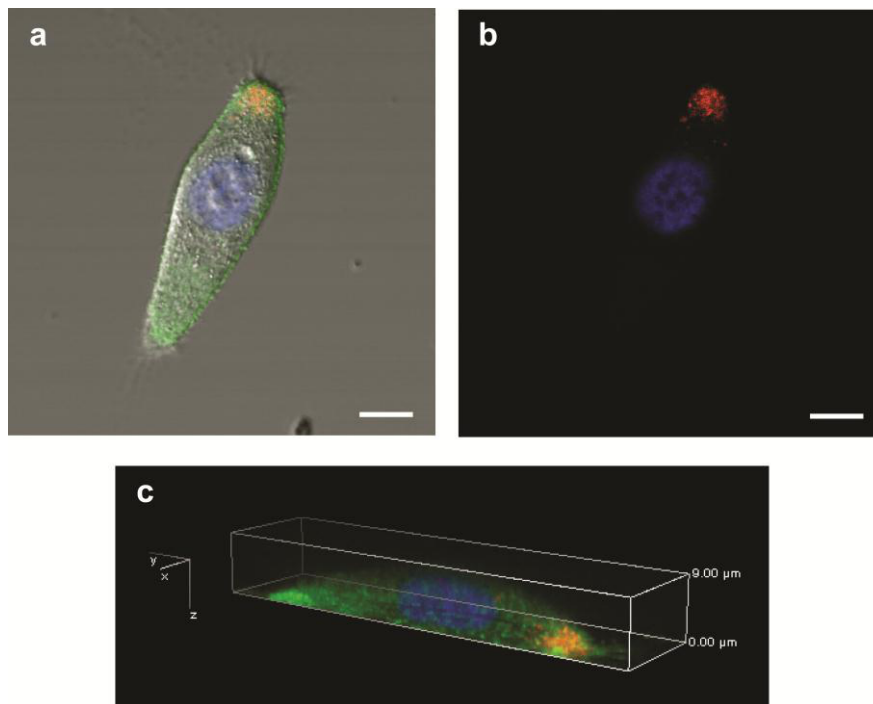


**Figure 5.11:** LSCM micrographs showing the cellular uptake of YHJ-8-91 6 hours post incubation. (a) The TLD-DIC image overlaid with Hoechst 34580 (blue), MT1-GFP (green) and YHJ-8-91 (red). (b) Hoechst 34580 (blue) and YHJ-8-91 (red) fluorescence overlaid image. (c) The 3-D reconstruction image of Hoechst 34580 (blue), MT1-GFP (green), and YHJ-8-91 cell membrane stain (red) overlay. Scale bars = 5  $\mu\text{m}$ .

reconstruction image is shown in **Figure 5.11** confirming internalization of YHJ-8-91.

## 5.8 Qualitative Time-Dependant Cellular Uptake of YHJ-8-91

The qualitative cellular uptake of YHJ-8-91 (10 nM) was probed over a 48 hour incubation time. CLSM was utilized to determine the presence of red emission originating from YHJ-8-91 inside of LNCaP-MT1-GFP cells. **Figure 5.12** shows an increase in the presence of red emission at 6, 24, and 48 hr time points. The acquired data in **Figure 5.12** has not been corrected for cell number. The large presence of internalized YHJ-8-91 at 24-48 hours at a concentration of 10 nM suggests that the LNCaP-MT1-GFP cells are not expunging the discrete packages from the cell in substantial quantities. The majority of discrete packages are localized at the invadopodia with some distribution throughout the cell. It has been recently shown that LNCaP cells overexpress myosin VI<sup>207, 208</sup>. To date, myosin VI is the only motor protein that delivers endocytotic packages to the negative end actin found at the invadopodia<sup>209</sup>. The microscopy data shown throughout this chapter suggests that the target MMPI is internalized via an endocytotic pathway and later trafficked toward the invadopodia. Live-cell microscopy imaging allowed the visualization of endocytotic internalization over the entire cell periphery before translocation of the packages elsewhere in the cell. Time-lapse images shown in **Figure 5.12** also suggest that the internalized packages are largely unsorted and remain at the polar end of the cell.

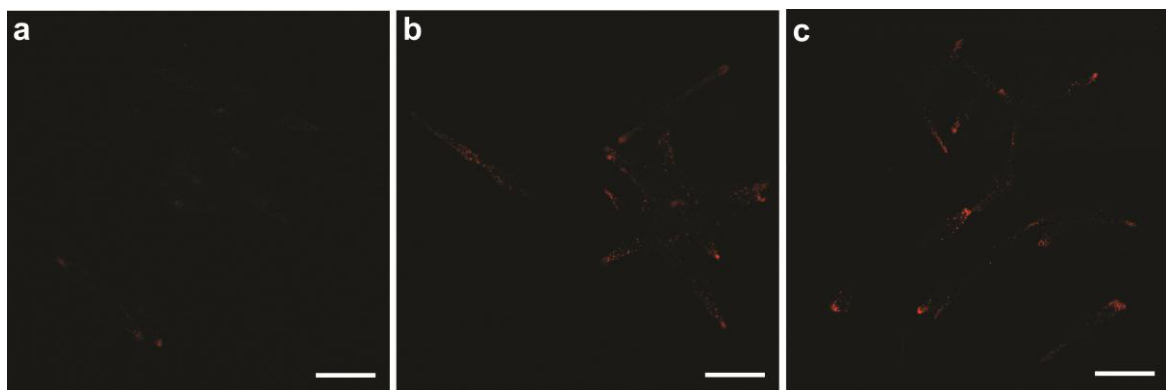


**Figure 5.12:** LSCM micrographs depicting cellular uptake of YHJ-8-91 (red) at 6, 24, and 48 hrs post incubation.

## 5.9 Probing MMPI-MMP Activity using Zymography

Zymography was used to determine if YHJ-8-91 has any effect on the ability of gelatinase A or B (MMP-2 or MMP-9, respectively) to cleave gelatin<sup>210</sup>. LNCaP-MT1-GFP cells were grown in media and media exchanged immediately prior to the addition of the target MMPI (YHJ-8-91) or controls (YHJ-8-89, C<sub>3</sub>Dye) at a concentration of 10  $\mu$ M and incubated for 6 hours. In addition to the two molecular controls, cells were incubated with a EtOH/TCEP/NaOH solution to monitor any adverse side effects of the solution on gelatin digestion. The cell media was removed from each well (2 mL) and aliquoted into 200  $\mu$ L vials, 29  $\mu$ L of a 70% glycerol stock was added to each vial, and the contents frozen at -80 °C until further use. Gelatin zymography was performed by Dale B. Bosco in the research laboratory of Q. X. Amy Sang as described by literature<sup>210</sup>. The cell media was thawed and the total protein of each fraction was determined by a bicinchoninic assay (BCA, Pierce). The same amount of protein was loaded in each lane, run on a SDS PAGE gel, renatured with Triton-X, allowed to digest gelatin for 60 hours in an incubator, and finally stained with coomassie brilliant blue. The results of the zymogram are shown in **Figure 5.13**. The white bands in the presence of the dark background are caused from the digestion of gelatin. Although the presence of both MMP-9 and MMP-2 can be visualized, only MMP-2 is clearly found in activated form. Quantification of the discernable pro-MMP-9, pro-MMP-2, and activated MMP-2 gelatin digestion was performed by M. Dru Roycik in the research laboratory of Q. X. Amy Sang as shown in **Figure 5.13b-d**. The percentage of active MMP-2 relative to pro-MMP-2 resulted in an increase of 2.6 fold when cells were treated with YHJ-8-91 when compared to an EtOH/TCEP/NaOH treatment. Bar graphs depicting gelatin digestion for MMP-2 and MMP-9 are shown in **Figure 5.13c-d**. The total amount of MMP-2 stays relatively constant and independent of the addition of YHJ-8-91 or the controls. The increase in gelatin digestion for cells incubated with YHJ-8-91 may be attributed to enzyme stabilization of the inhibitor interacting with the catalytic domain to reduce auto-degradation during the incubation stage of the experiment. The level of active MMP-2 in cells treated with YHJ-8-91 is similar to LNCaP-MT1-GFP cells not treated with anything in the absence of a media change. The zymogram results suggest that MMP-2 activity is being impacted by the addition of YHJ-8-91. Additional functional assays probing cellular migration may aide in supporting or discrediting this observation.

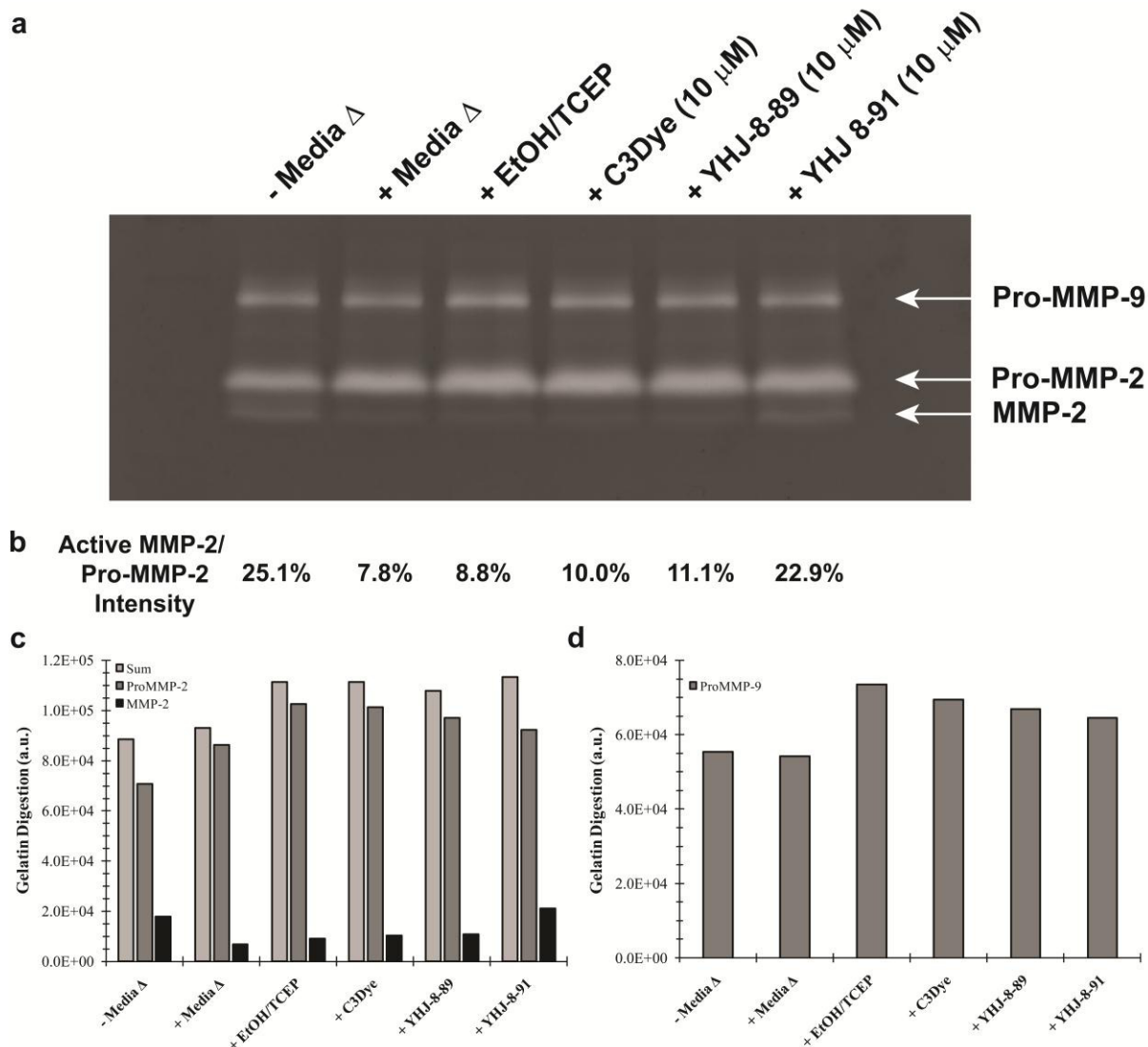


**Figure 5.13:** The gelatin zymogram of conditioned spent media from LNCaP-MT1-GFP cells incubated with C<sub>3</sub>Dye, YHJ-8-89, YHJ-8-91, and controls are shown, where white bands indicate gelatin digestion (a). The percentage of active MMP-2 to pro-MMP-2 from (a) shown in (b). Bar graphs indicating the level of gelatin digestion caused from MMP-2 (c) and MMP-9 (d).

## 5.10 Conclusions and Future Directions

The design of a novel MMPI (YHJ-8-91) containing a fluorescent marker was incubated with both LNCaP-MT1-GFP and LNCaP-GFP cell lines and found to be internalized over time. LNCaP-MT1-GFP cells produce active MMP-2 and MT1-MMP, while LNCaP-GFP cells do not produce measureable protein quantities of MMP-2 and MT1-MMP. The endocytotic packages are internalized all over the cell periphery and translocate to the polar end of the cell with time. The internalized MMPI is present in LNCaP-MT1-GFP

cells 48 hrs post incubation. Attempts at direct spectral co-localization of MT1-GFP with YHJ-8-91 under live-microscopy conditions were unsuccessful. Additional fixed-cell studies may alleviate some of the observed spacial artifacts. The zymogram data suggests that the addition of YHJ-8-91 to LNCaP-MT1-GFP cells causes an effect on MMP activity. With that said, one can not exclude other possibilities of either the involvement of non targeted MMPs or a non-MMP related cellular uptake mechanism from this data. Although a high degree of molecular specificity is responsible for cellular uptake of YHJ-8-91 demonstrated by YHJ-8-89 and C<sub>3</sub>Dye controls, more experimentation is needed to pin-point the mechanism and molecules responsible for this unusual phenomenon. Additional experiments using fluorescently labeled commercial MMPIs or nanoparticle platforms as optical trackers may help elucidate the role of YHJ-8-91 on MMP structure and function in LNCaP cells. Regardless of the cellular uptake mechanism, the internalization of MMPIs may influence their efficiency and applicability as realistic drug candidates as MMP targeted therapeutics.

## APPENDIX A

### A. KHÖLER ILLUMINATION ALIGNMENT PROTOCOL

*Khöler illumination is specific for a specific objective at a specific magnification.*

Alignment Protocol:

1. For general alignment use a low magnification objective such as 10X (if possible)
2. Loosen Set Screw, Remove DIC Polarizer and DIC Condenser Prism from Light Path, Open the condenser diaphragm, Close Field Diaphragm
3. Bring specimen (stained for Bright-field microscopy applications) into focus
4. Adjust the condenser height so the field diaphragm is in the same focal plane
5. Center the field diaphragm using the two centering screws
6. Adjust the aperture diaphragm by opening or closing the slider until the image transitions from light to dark or remove the eyepiece and adjust until ~75% of the field of view should appear light while ~25% of the field of view should appear dark
7. Tighten Set Screw

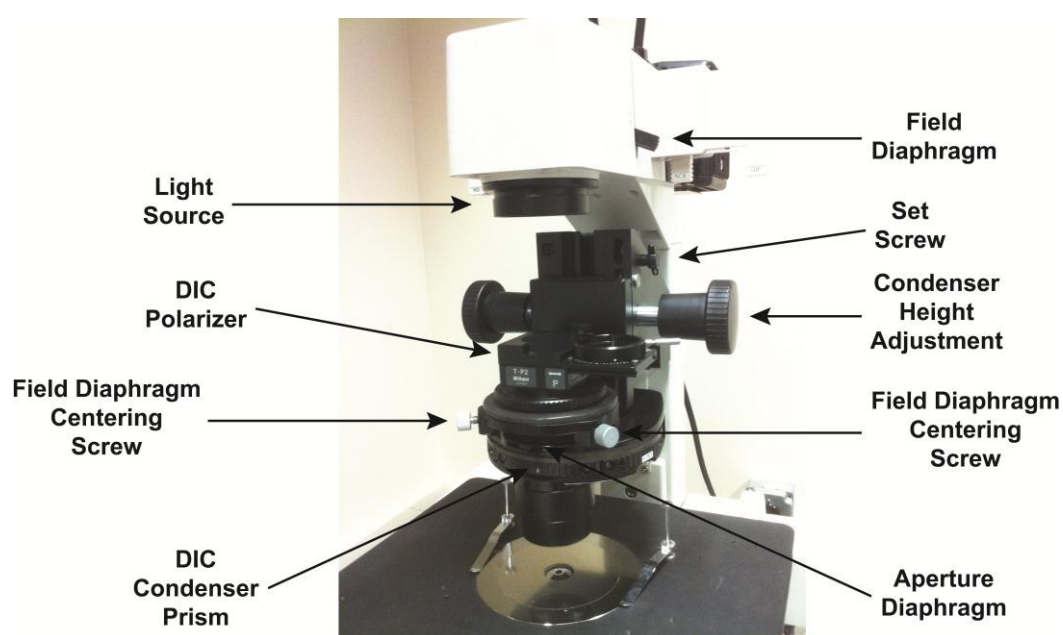


**Figure A1:** Labeled microscope components necessary for alignment for Köhler illumination.

## APPENDIX B

### B. NMR SPECTRA OF FITC-ACETYLENE

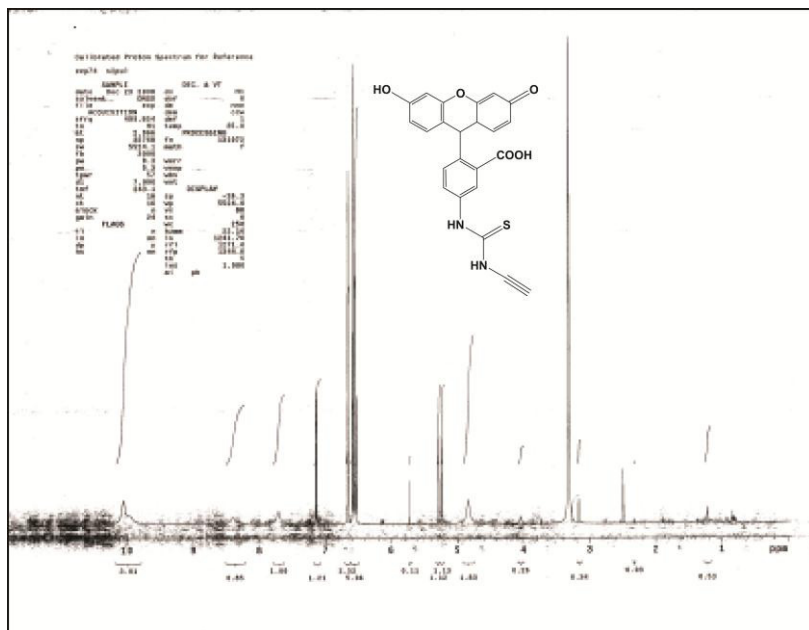


Figure B1: NMR spectrum of FITC-Acetylene.

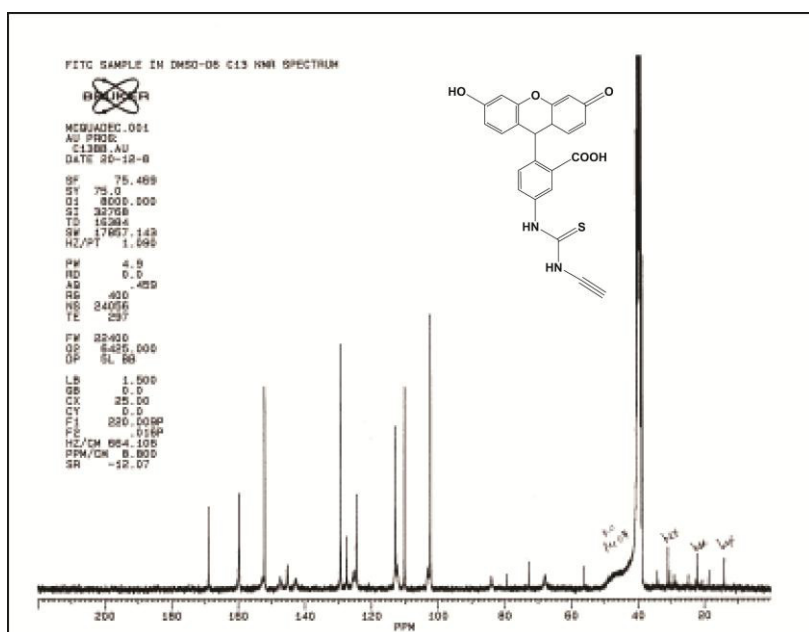
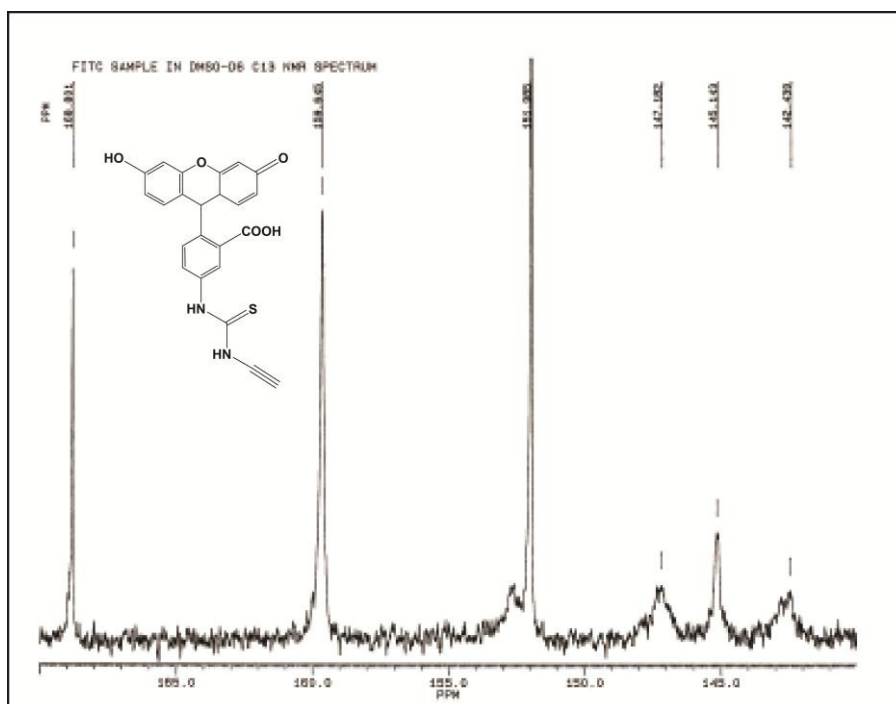
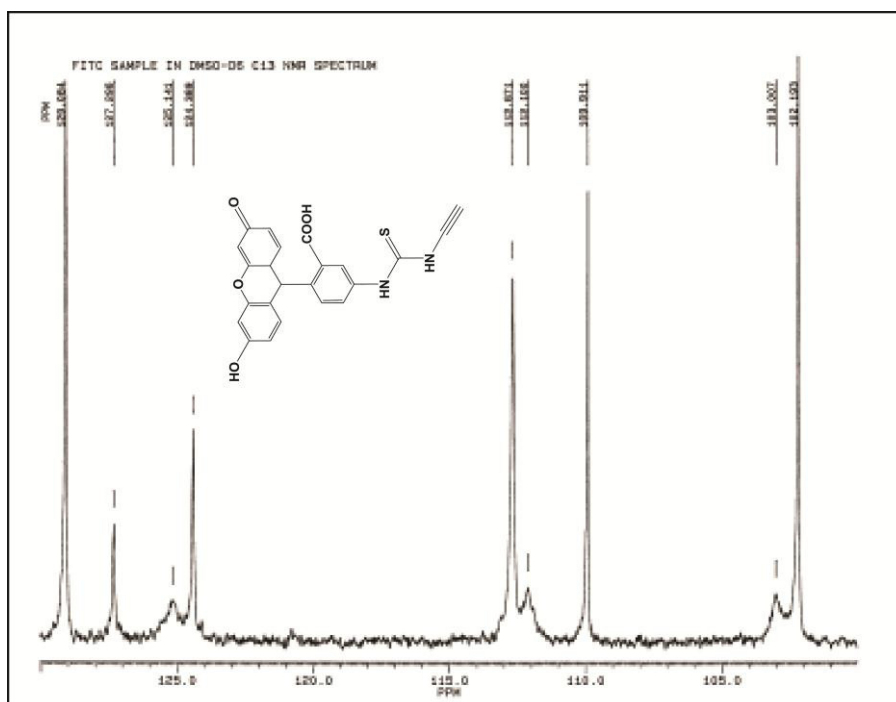


Figure B2: NMR spectrum of FITC-Acetylene.



**Figure B3:** NMR spectrum of FITC-Acetylene.



**Figure B4:** NMR spectrum of FITC-Acetylene.

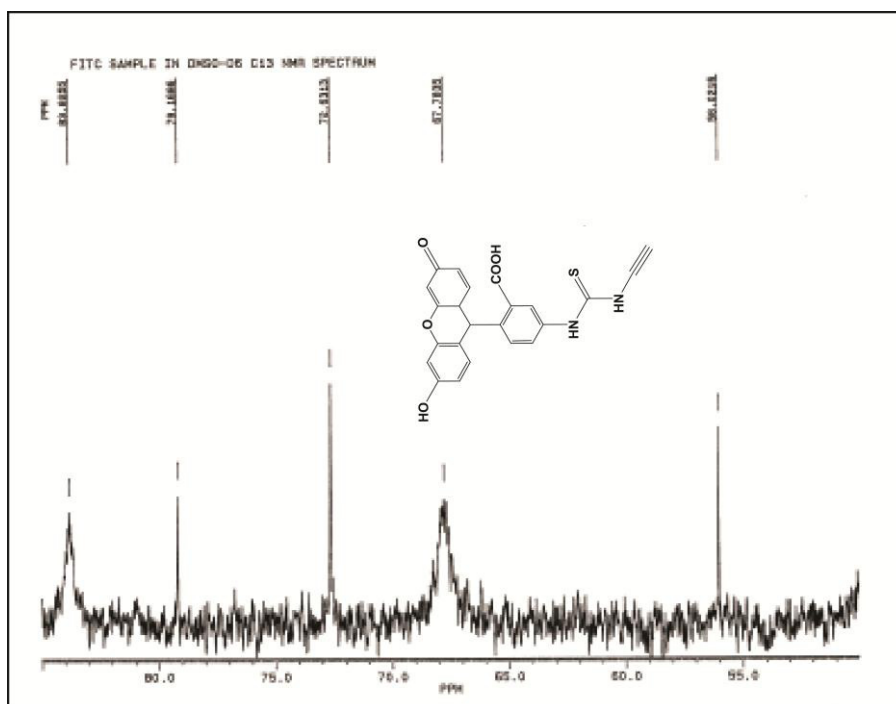


**Figure B5:** NMR spectrum of FITC-Acetylene.

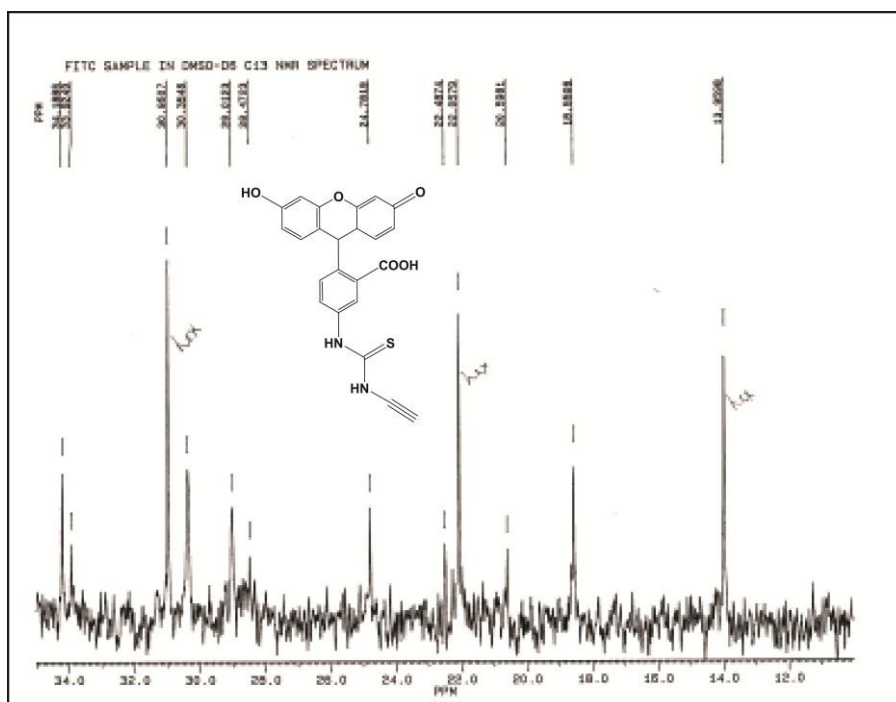


**Figure B6:** NMR spectrum of FITC-Acetylene.

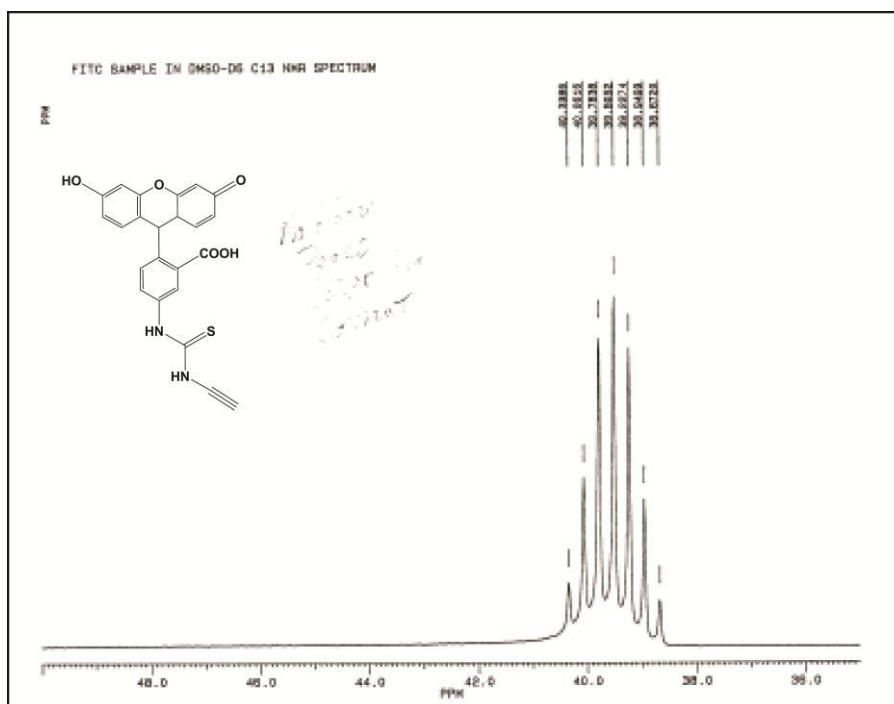


**Figure B7:** NMR spectrum of FITC-Acetylene.

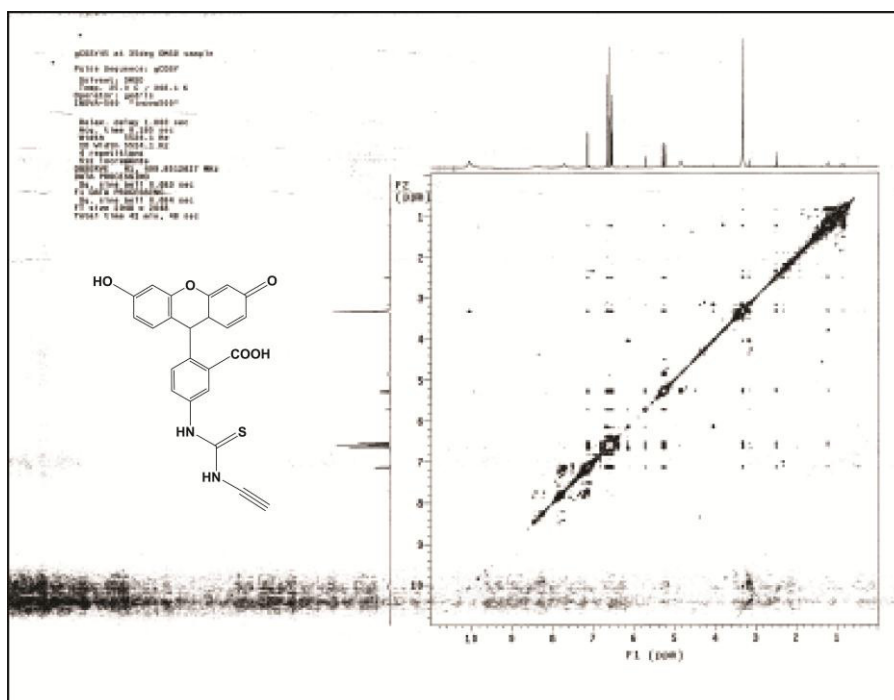


**Figure B8:** NMR spectrum of FITC-Acetylene.

## APPENDIX C

### C. THEORETICAL HALL SENSITIVITY CALCULATIONS

```

[For Z = 0.272, X = .34, Y = .24:
> printlevel := 2
                                printlevel := 2
(1)
> 
$$\left( \int_{-0.5}^{0.5} \int_{-0.5}^{0.5} \frac{2 \cdot (0.272)^2 - (x + 0.34)^2 - (y - 0.24)^2}{\left( (x + 0.34)^2 + (y - 0.24)^2 + (0.272)^2 \right)^{\frac{5}{2}}} dx dy \right) \cdot (344^3) \cdot 0.119 \cdot 10^{-8}$$

(2)
                                0.3388706964
> 
$$\text{int} \left( \left( \frac{2 \cdot (0.272)^2 - (x + 0.34)^2 - (y - 0.24)^2}{\left( (x + 0.34)^2 + (y - 0.24)^2 + (0.272)^2 \right)^{\frac{5}{2}}} \right), [x = -0.5 .. 0.5, y = -0.5 .. 0.5] \right) \cdot (344^3) \cdot 0.119 \cdot 10^{-8}$$

(3)
                                0.3388706964
> 
$$f := \left( \frac{2 \cdot (0.272)^2 - (x + 0)^2 - (y - 0)^2}{\left( (x + 0)^2 + (y - 0)^2 + (0.272)^2 \right)^{\frac{5}{2}}} \right) \cdot (344^3) \cdot 0.119 \cdot 10^{-8};$$

(4)
                                0.04844202496 (0.147968 - x^2 - y^2)
                                (x^2 + y^2 + 0.073984)^{5/2}
> 
$$\text{evalf}(\text{int}(f(x, y), [x = -0.5 .. 0.5, y = -0.5 .. 0.5]));$$

(5)
                                0.3947106354
> 
$$g := \left( \frac{2 \cdot \left( 0.272 + \frac{m}{30} \right)^2 - \left( x + 0 + \frac{l}{30} \right)^2 - (y - 0)^2}{\left( \left( x + 0 + \frac{l}{30} \right)^2 + (y - 0)^2 + \left( 0.272 + \frac{m}{30} \right)^2 \right)^{\frac{5}{2}}} \right) \cdot (344^3) \cdot 0.119 \cdot 10^{-8};$$

(6)
                                0.04844202496  $\left( 2 \left( 0.272 + \frac{1}{30} m \right)^2 - \left( x + \frac{1}{30} l \right)^2 - y^2 \right)$ 
                                 $\left( \left( x + \frac{1}{30} l \right)^2 + y^2 + \left( 0.272 + \frac{1}{30} m \right)^2 \right)^{5/2}$ 
> N := 45
                                N := 45
(7)
> Data := matrix(N + 1, N + 1);
for l from 0 to N do
for m from 0 to N do Data[l + 1, m + 1] := (int(g(x, y), [x = -0.5 .. 0.5, y = -0.5 .. 0.5])); od;
od;
evalm(Data)
:
:
> with(ExcelTools) :
> R := Array(Data);
(9)
                                R :=  $\begin{bmatrix} 1.46 \times 1.46 \text{ Array} \\ \text{Data Type: anything} \\ \text{Storage: rectangular} \\ \text{Order: Fortran\_order} \end{bmatrix}$ 
> Export(R)

```

**Figure C1:** Maple v13 theoretical Hall sensitivity calculations.

## APPENDIX D

### D. MASS SPECTROGRAM OF TARGET MMPI

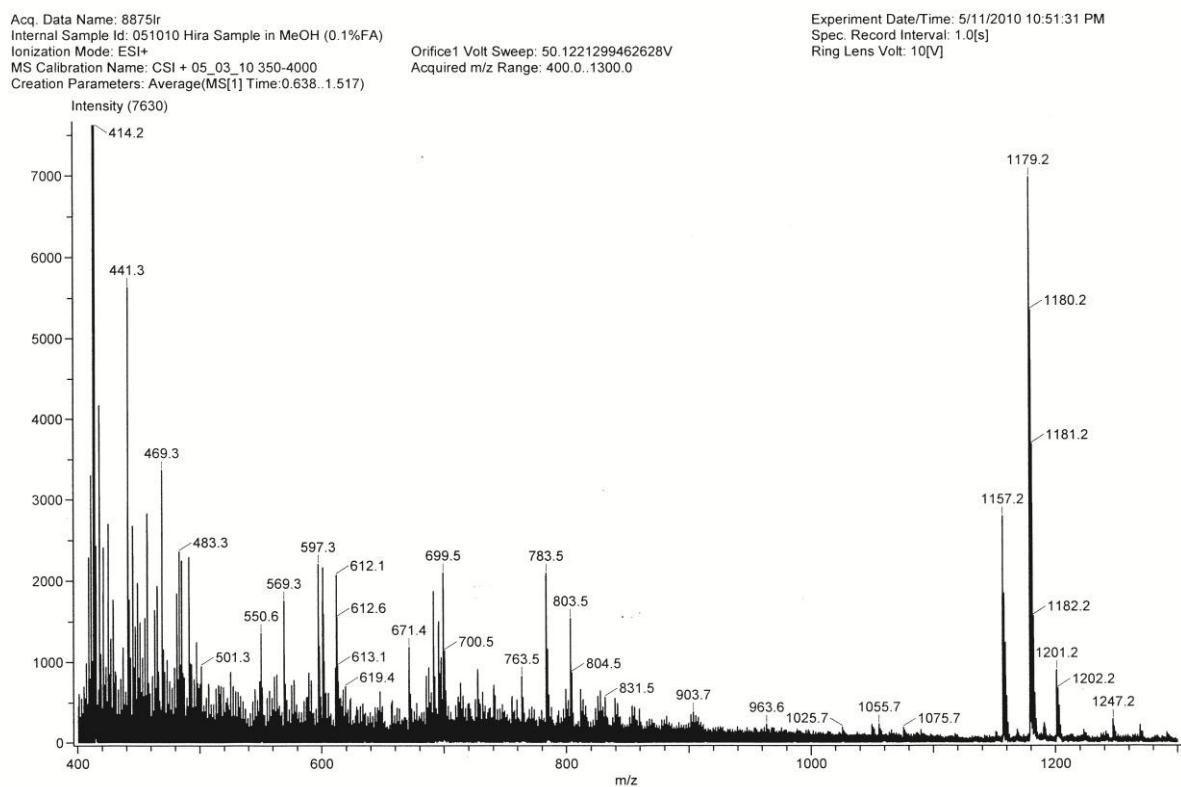


**Figure D1:** Mass spectrogram of target MMPI.

## APPENDIX E

### E. NMR spectra for YHJ-8-91, YHJ-8-89, and C<sub>3</sub>Dye

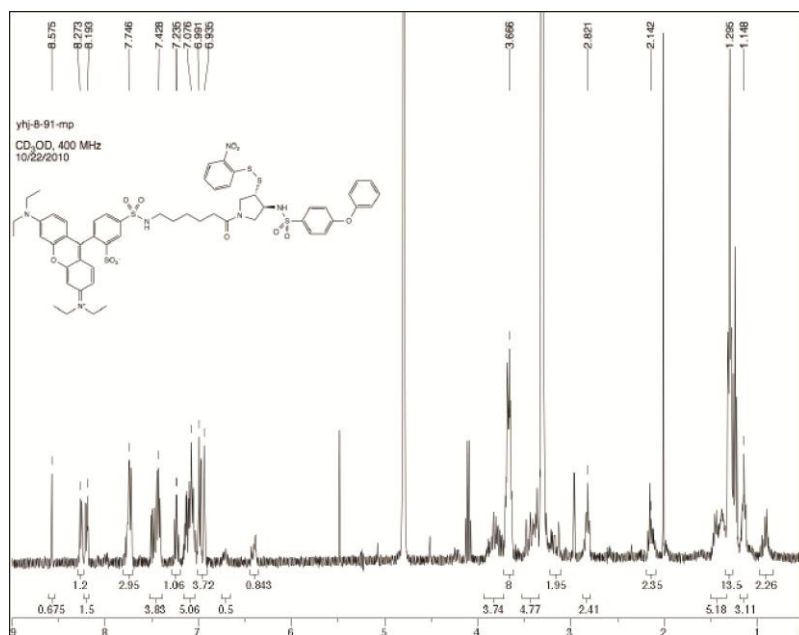


Figure E1: NMR spectrum of YHJ-8-91.

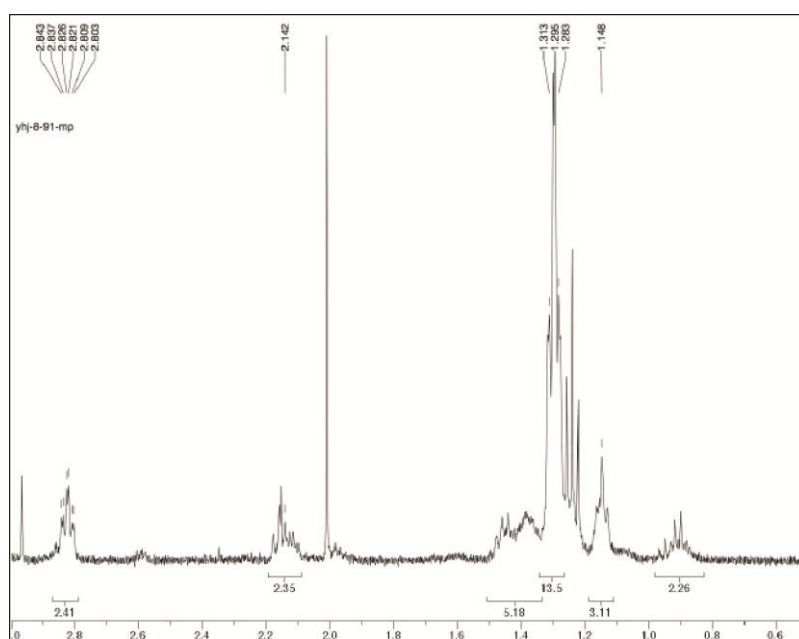
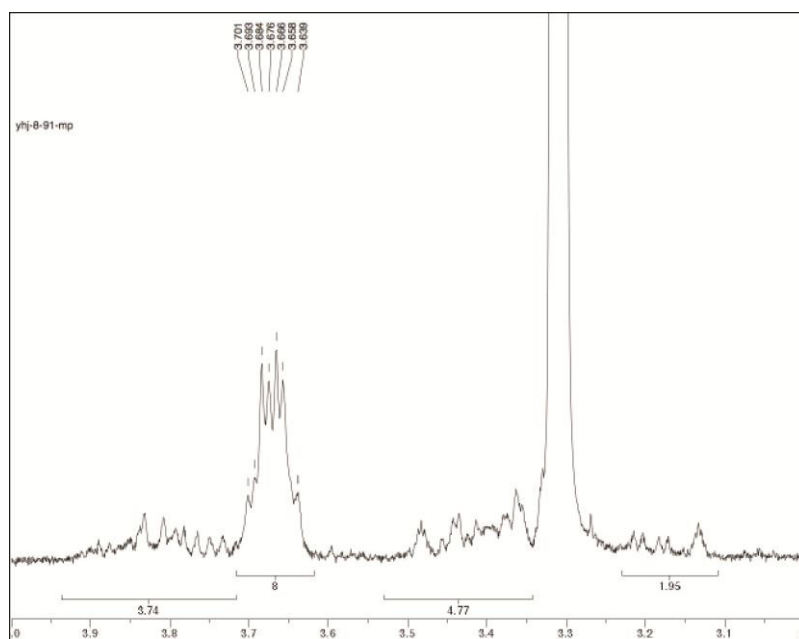
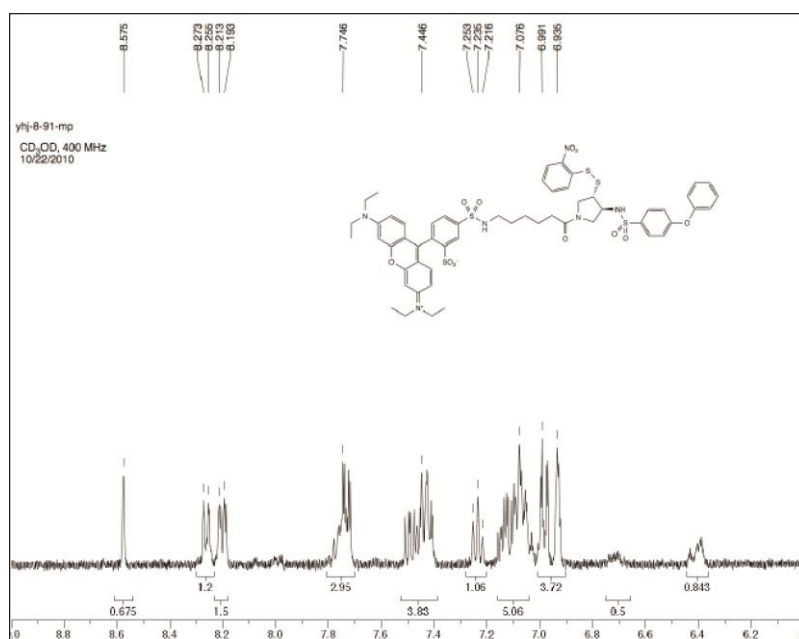


Figure E2: NMR spectrum of YHJ-8-91.



**Figure E3:** NMR spectrum of YHJ-8-91.



**Figure E4:** NMR spectrum of YHJ-8-91.

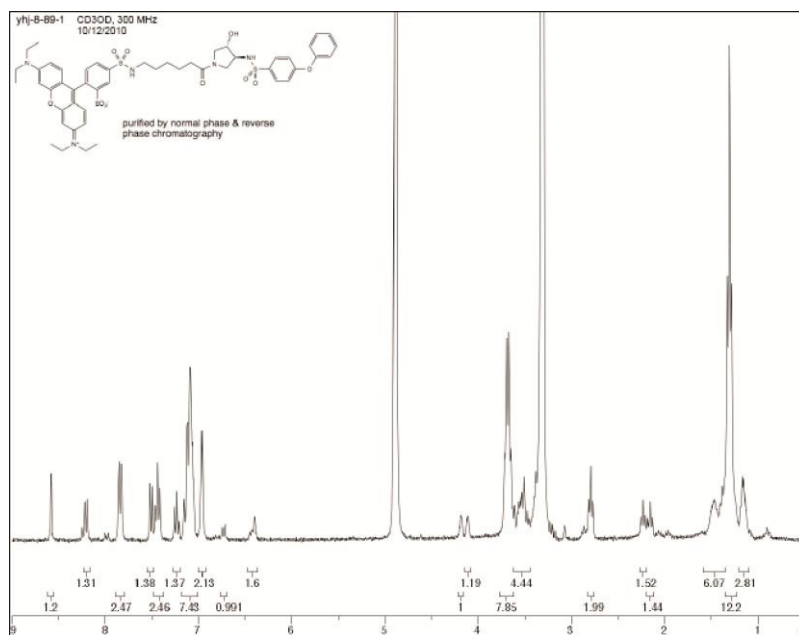


**Figure E5:** NMR spectrum of YHJ-8-89.

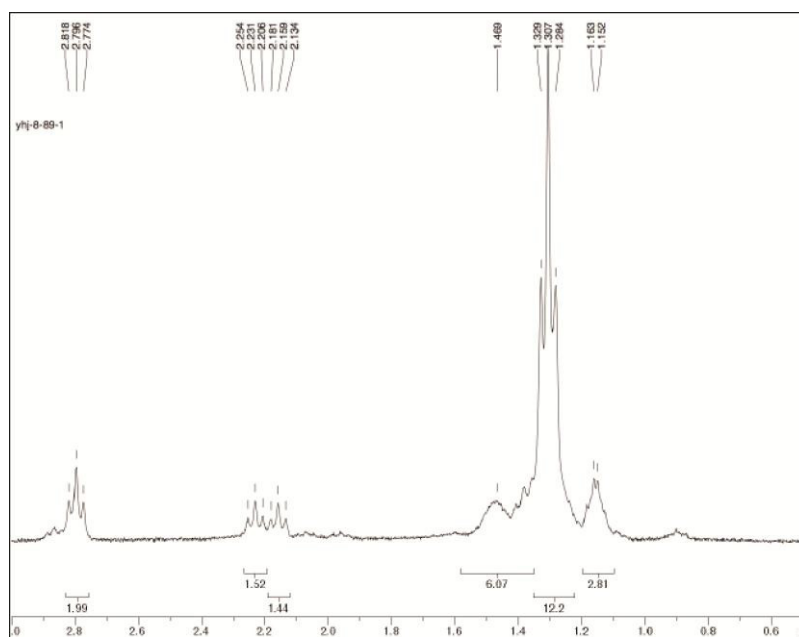


**Figure E6:** NMR spectrum of YHJ-8-89.

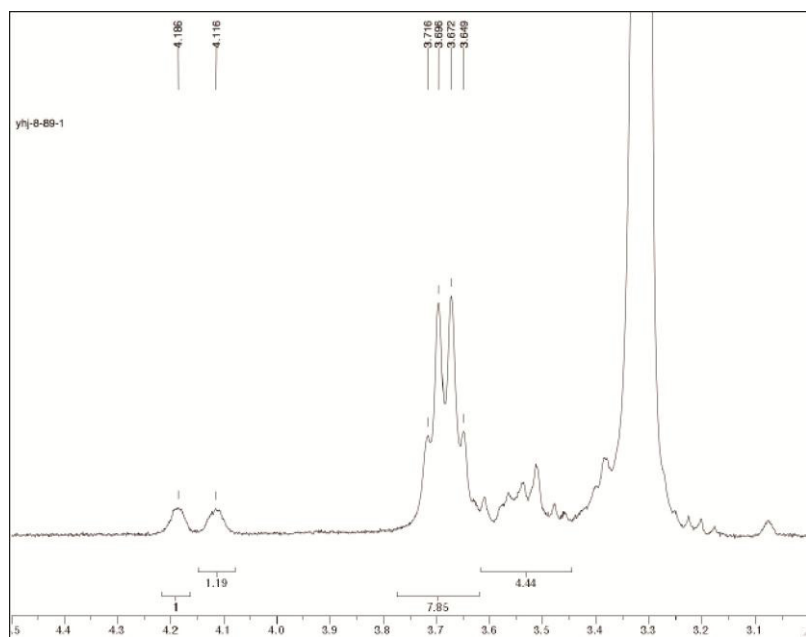


**Figure E7:** NMR spectrum of YHJ-8-89.

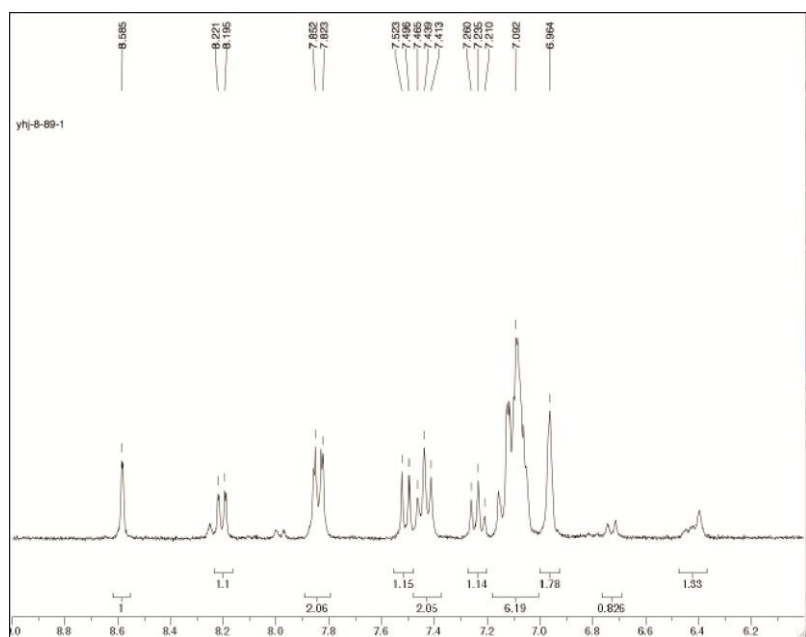


**Figure E8:** NMR spectrum of YHJ-8-89.

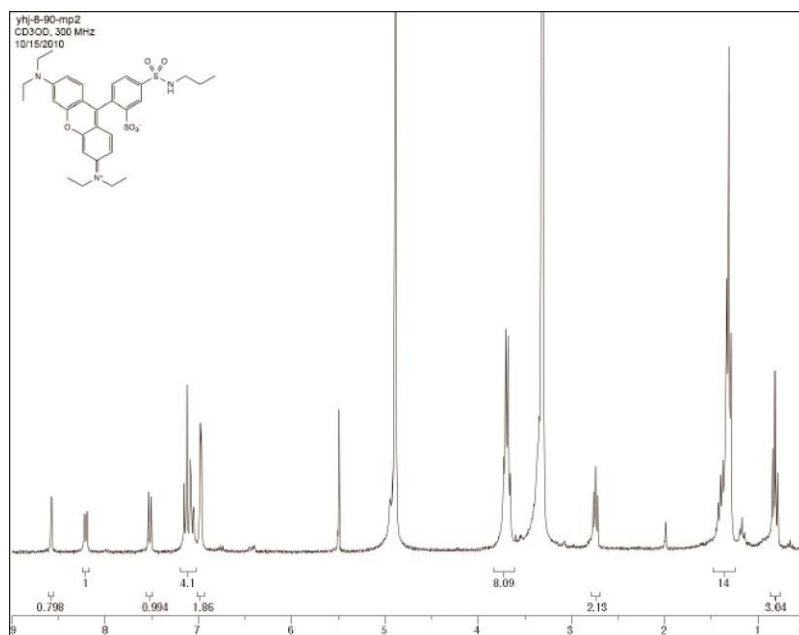


**Figure E9:** NMR spectrum of C<sub>3</sub>Dye.

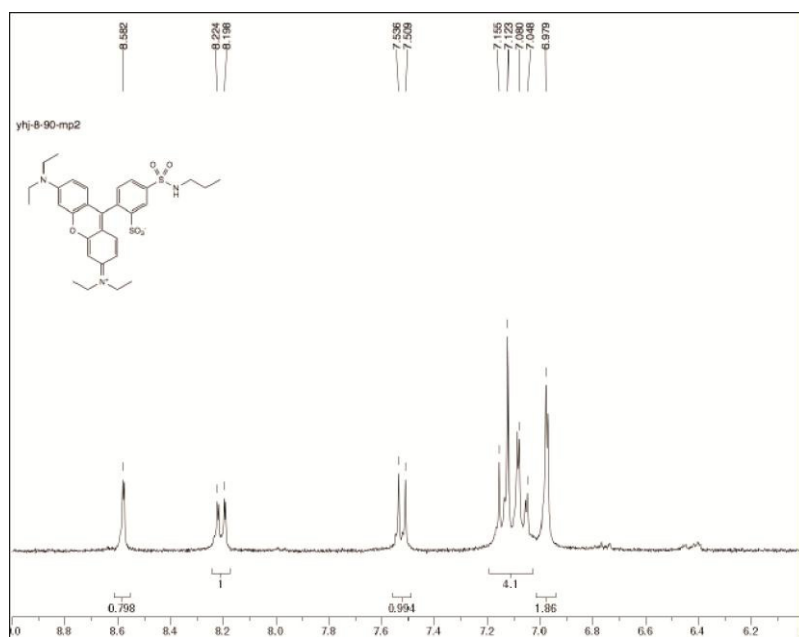


**Figure E10:** NMR spectrum of C<sub>3</sub>Dye.

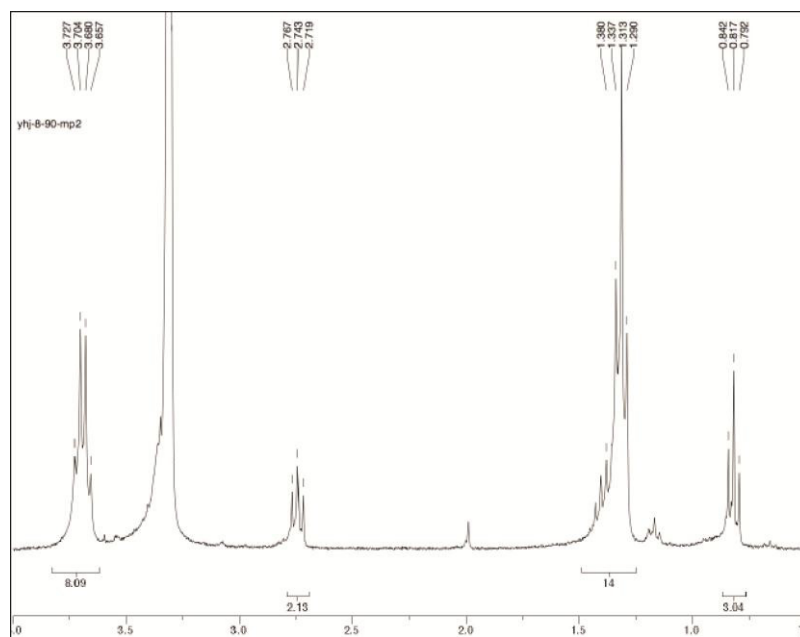


**Figure E11:** NMR spectrum of C<sub>3</sub>Dye.

## APPENDIX F

### F1. ANOVA STATISTICS ON THE CELLULAR UPTAKE OF THE MMPI AND CONTROLS

**Table F1:** ANOVA statistics on the quantification of the cellular uptake of YHJ-8-91, YHJ-8-89, and C<sub>3</sub>Dye 6 hours post incubation.

**Analyse-it v2.21**  
**1-way ANOVA**  
**16 December 2010**

n	64
---	----

Groups	n	Mean	SE	Pooled SE	SD
C3Dye	20	50.83	14.30	1353.55	63.95
Dye-OH	20	2671.49	488.95	1353.55	2186.66
Dye-SH	24	17737.03	1970.90	1235.61	9655.41

Source of variation	Sum squares	DF	Mean square	F statistic	p
Groups	4091217231	2	2045608615	55.83	<0.0001
Residual	2235144082	61	36641706		
Total	6326361313	63			

Tukey Contrast	Difference	99% CI		
C3Dye v Dye-OH	-2620.66	-8413.10	3171.78	
C3Dye v Dye-SH	-17686.20	-23232.04	-12140.36	(significant)
Dye-OH v Dye-SH	-15065.55	-20611.39	-9519.71	(significant)

# APPENDIX G

## G. COPYRIGHT RELEASE FORMS

Rightslink Printable License

<https://s100.copyright.com/App/PrintableLicenseFrame.jsp?publisher...>

### AMERICAN CHEMICAL SOCIETY LICENSE TERMS AND CONDITIONS

Mar 18, 2011

This is a License Agreement between Steven M Hira ("You") and American Chemical Society ("American Chemical Society") provided by Copyright Clearance Center ("CCC"). The license consists of your order details, the terms and conditions provided by American Chemical Society, and the payment terms and conditions.

**All payments must be made in full to CCC. For payment instructions, please see information listed at the bottom of this form.**

License Number	2632051440633
License Date	Mar 18, 2011
Licensed content publisher	American Chemical Society
Licensed content publication	Organic Letters
Licensed content title	Microcapsules with Three Orthogonal Reactive Sites
Licensed content author	Brian P. Mason et al.
Licensed content date	Apr 1, 2009
Volume number	11
Issue number	7
Type of Use	Thesis/Dissertation
Requestor type	Not specified
Format	Electronic
Portion	Table/Figure/Micrograph
Number of Table/Figure /Micrographs	15
Author of this ACS article	Yes
Order reference number	
Title of the thesis / dissertation	TARGETED DYE LABELING AS A TOOL FOR IMAGING MATERIAL AND BIOMATERIAL MICROENVIRONMENTS
Expected completion date	Apr 2011
Estimated size(pages)	121
Billing Type	Invoice
Billing Address	95 Chieftan Way ATTN: Chemistry Dept. Box 68 Tallahassee, FL 32306 United States
Customer reference info	
Total	0.00 USD
Terms and Conditions	

**Figure G1:** American Chemical Society copyright release.

---

**Date:** Thu, 10 Mar 2011 11:56:23 +0000 [03/10/2011 06:56:23 EDT]  
**From:** CONTRACTS-COPYRIGHT (shared) <Contracts-Copyright@rsc.org>  
**To:** 'Steven Hira' <shira@chem.fsu.edu>  
**Subject:** RE: Website Email: Copyright Information

---

Dear Steve

You do not formally have to request permission to reproduce your own figures provided that you include the following credit to the Royal Society of Chemistry:

Roberts, C.W., Hira, S.M., Mason, B.P., Strouse, G.F. & Stoltz, C.A., CrystEngComm, 13, 1074-1076, 2011 - Reproduced by permission of the Royal Society of Chemistry

Best wishes

Gill

Gill Cockhead (Mrs), Contracts & Copyright Executive  
Royal Society of Chemistry, Thomas Graham House  
Science Park, Milton Road, Cambridge CB4 0WF, UK  
Tel +44 (0) 1223 432134, Fax +44 (0) 1223 423623  
<http://www.rsc.org><<http://www.rsc.org/>>

**Figure G2:** Royal Society of Chemistry copyright release.

## REFERENCES

1. Zhang, J., Campbell, R.E., Ting, A.Y. & Tsien, R.Y. Creating new fluorescent probes for cell biology. *Nature Reviews Molecular Cell Biology* **3**, 906-918 (2002).
2. Yildiz, A. et al. Myosin V walks hand-over-hand: Single fluorophore imaging with 1.5-nm localization. *Science* **300**, 2061-2065 (2003).
3. Baumgart, T., Hess, S.T. & Webb, W.W. Imaging coexisting fluid domains in biomembrane models coupling curvature and line tension. *Nature* **425**, 821-824 (2003).
4. Fara, P. A microscopic reality tale. *Nature* **459**, 642-644 (2009).
5. Giepmans, B.N.G., Adams, S.R., Ellisman, M.H. & Tsien, R.Y. Review - The fluorescent toolbox for assessing protein location and function. *Science* **312**, 217-224 (2006).
6. Shaner, N.C. et al. Improved monomeric red, orange and yellow fluorescent proteins derived from *Discosoma* sp red fluorescent protein. *Nature Biotechnology* **22**, 1567-1572 (2004).
7. Bradbury, S., Evennett, P.J. Contrast techniques in light microscopy. (Bios Scientific Publishers, Oxford; 1996).
8. Spector, D.L., Goldman, R.D. (ed.) Basic methods in microscopy: Protocols and concepts from cells: A laboratory manual. (Cold Spring Harbor Press, Cold Spring Harbor; 2006).
9. Hibbs, A.R. Confocal microscopy for biologists. (Kluwer, New York; 2004).
10. Pawley, J.B. (ed.) Handbook of biological confocal microscopy, Edn. 3rd. (Springer, New York; 2006).
11. Sheppard, C.J.R., Shotton, D.M. Confocal laser scanning microscopy. (Bios Scientific Publishers, Oxford; 1997).
12. Alberts, B.J., A.; Lewis, J.; Raff, M.; Roberts, K.; Walter, P. Molecular Biology of the Cell, Edn. 4. (Garland Science, New York; 2002).
13. Yuan, J., Hira, S.M., Strouse, G.F. & Hirst, L.S. Lipid bilayer discs and banded tubules: Photoinduced lipid sorting in ternary mixtures. *Journal of the American Chemical Society* **130**, 2067-2072 (2008).
14. Mason, B.P., Hira, S.M., Strouse, G.F. & McQuade, D.T. Microcapsules with Three Orthogonal Reactive Sites. *Organic Letters* **11**, 1479-1482 (2009).

15. Korlach, J., Schwille, P., Webb, W.W. & Feigenson, G.W. Characterization of lipid bilayer phases by confocal microscopy and fluorescence correlation spectroscopy. *Proceedings of the National Academy of Sciences of the United States of America* **96**, 8461-8466 (1999).
16. Baumgart, T. et al. Large-scale fluid/fluid phase separation of proteins and lipids in giant plasma membrane vesicles. *Proceedings of the National Academy of Sciences of the United States of America* **104**, 3165-3170 (2007).
17. Groves, J.T. & Boxer, S.G. Micropattern formation in supported lipid membranes. *Accounts of Chemical Research* **35**, 149-157 (2002).
18. Wise, A.R., Nye, J.A. & Groves, J.T. Discrete arrays of liquid-crystal-supported proteolipid monolayers as phantom cell surfaces. *Chemphyschem* **9**, 1688-1692 (2008).
19. Takenawa, T. & Itoh, T. Phosphoinositides, key molecules for regulation of actin cytoskeletal organization and membrane traffic from the plasma membrane. *Biochimica Et Biophysica Acta-Molecular and Cell Biology of Lipids* **1533**, 190-206 (2001).
20. Simons, K. & Vaz, W.L.C. Model systems, lipid rafts, and cell membranes. *Annual Review of Biophysics and Biomolecular Structure* **33**, 269-295 (2004).
21. Veatch, S.L. & Keller, S.L. Separation of liquid phases in giant vesicles of ternary mixtures of phospholipids and cholesterol. *Biophysical Journal* **85**, 3074-3083 (2003).
22. Ayuyan, A.G. & Cohen, F.S. Lipid peroxides promote large rafts: Effects of excitation of probes in fluorescence microscopy and electrochemical reactions during vesicle formation. *Biophysical Journal* **91**, 2172-2183 (2006).
23. Zhao, Y., Mahajan, N., Lu, R.B. & Fang, J.Y. Liquid-crystal imaging of molecular-tilt ordering in self-assembled lipid tubules. *Proceedings of the National Academy of Sciences of the United States of America* **102**, 7438-7442 (2005).
24. Karlsson, M. et al. Micropipet-assisted formation of microscopic networks of unilamellar lipid bilayer nanotubes and containers. *Langmuir* **17**, 6754-6758 (2001).
25. Girotti, A.W. Photodynamic lipid-peroxidation in biological-systems. *Photochemistry and Photobiology* **51**, 497-509 (1990).
26. Scheinberg, D.A., Villa, C.H., Escorcía, F.E. & McDevitt, M.R. Conscripts of the infinite armada: systemic cancer therapy using nanomaterials. *Nature Reviews Clinical Oncology* **7**, 266-276 (2010).
27. Doshi, N. & Mitragotri, S. Designer Biomaterials for Nanomedicine. *Advanced Functional Materials* **19**, 3843-3854 (2009).

28. Kotov, N.A. et al. Nanomaterials for Neural Interfaces. *Advanced Materials* **21**, 3970-4004 (2009).
29. Kim, J., Piao, Y. & Hyeon, T. Multifunctional nanostructured materials for multimodal imaging, and simultaneous imaging and therapy. *Chemical Society Reviews* **38**, 372-390 (2009).
30. Huang, X.H., Jain, P.K., El-Sayed, I.H. & El-Sayed, M.A. Gold nanoparticles: interesting optical properties and recent applications in cancer diagnostic and therapy. *Nanomedicine* **2**, 681-693 (2007).
31. Ruoslahti, E., Bhatia, S.N. & Sailor, M.J. Targeting of drugs and nanoparticles to tumors. *Journal of Cell Biology* **188**, 759-768 (2010).
32. Larson, D.R. et al. Water-soluble quantum dots for multiphoton fluorescence imaging in vivo. *Science* **300**, 1434-1436 (2003).
33. Delehanty, J.B., Mattoussi, H. & Medintz, I.L. Delivering quantum dots into cells: strategies, progress and remaining issues. *Analytical and Bioanalytical Chemistry* **393**, 1091-1105 (2009).
34. Delehanty, J.B., Boeneman, K., Bradburne, C.E., Robertson, K. & Medintz, I.L. Quantum dots: a powerful tool for understanding the intricacies of nanoparticle-mediated drug delivery. *Expert Opinion on Drug Delivery* **6**, 1091-1112 (2009).
35. Gao, X.H. et al. In vivo molecular and cellular imaging with quantum dots. *Current Opinion in Biotechnology* **16**, 63-72 (2005).
36. Nie, S.M., Xing, Y., Kim, G.J. & Simons, J.W. Nanotechnology applications in cancer. *Annual Review of Biomedical Engineering* **9**, 257-288 (2007).
37. Smith, A.M., Duan, H.W., Mohs, A.M. & Nie, S.M. Bioconjugated quantum dots for in vivo molecular and cellular imaging. *Advanced Drug Delivery Reviews* **60**, 1226-1240 (2008).
38. Rosenberg, J.T., Kogot, J.M., Lovingood, D.D., Strouse, G.F. & Grant, S.C. Intracellular Bimodal Nanoparticles Based on Quantum Dots for High-Field MRI at 21.1 T. *Magnetic Resonance in Medicine* **64**, 871-882 (2010).
39. Cumberland, S.L. et al. Inorganic clusters as single-source precursors for preparation of CdSe, ZnSe, and CdSe/ZnS nanomaterials. *Chemistry of Materials* **14**, 1576-1584 (2002).
40. Gerbec, J.A., Magana, D., Washington, A. & Strouse, G.F. Microwave-enhanced reaction rates for nanoparticle synthesis. *Journal of the American Chemical Society* **127**, 15791-15800 (2005).

41. Lovingood, D.D. & Strouse, G.F. Microwave Induced In-Situ Active Ion Etching of Growing InP Nanocrystals. *Nano Letters* **8**, 3394-3397 (2008).
42. Uemura, T. et al. Effects of intratracheally administered indium phosphide on male Fischer 344 rats. *Journal of Occupational Health* **39**, 205-210 (1997).
43. Yamazaki, K. et al. Long term pulmonary toxicity of indium arsenide and indium phosphide instilled intratracheally in hamsters. *Journal of Occupational Health* **42**, 169-178 (2000).
44. Jain, P.K., Huang, X., El-Sayed, I.H. & El-Sayad, M.A. Review of some interesting surface plasmon resonance-enhanced properties of noble metal nanoparticles and their applications to biosystems. *Plasmonics* **2**, 107-118 (2007).
45. Liu, G.L. et al. A nanoplasmonic molecular ruler for measuring nuclease activity and DNA footprinting. *Nature Nanotechnology* **1**, 47-52 (2006).
46. Yun, C.S. et al. Nanometal surface energy transfer in optical rulers, breaking the FRET barrier. *Journal of the American Chemical Society* **127**, 3115-3119 (2005).
47. Jennings, T.L., Singh, M.P. & Strouse, G.F. Fluorescent lifetime quenching near d=1.5 nm gold nanoparticles: Probing NSET validity. *Journal of the American Chemical Society* **128**, 5462-5467 (2006).
48. Jennings, T.L., Schlatterer, J.C., Singh, M.P., Greenbaum, N.L. & Strouse, G.F. NSET molecular beacon analysis of hammerhead RNA substrate binding and catalysis. *Nano Letters* **6**, 1318-1324 (2006).
49. Singh, M.P. & Strouse, G.F. Involvement of the LSPR Spectral Overlap for Energy Transfer between a Dye and Au Nanoparticle. *Journal of the American Chemical Society* **132**, 9383-9391 (2010).
50. Kim, C.K. et al. Entrapment of Hydrophobic Drugs in Nanoparticle Monolayers with Efficient Release into Cancer Cells. *Journal of the American Chemical Society* **131**, 1360-1361 (2009).
51. Hong, R. et al. Glutathione-mediated delivery and release using monolayer protected nanoparticle carriers. *Journal of the American Chemical Society* **128**, 1078-1079 (2006).
52. Prigodich, A.E. et al. Nano-flares for mRNA Regulation and Detection. *Acs Nano* **3**, 2147-2152 (2009).
53. Mason, B.P.S., J.L.; McQuade, D.T. in *Molecular Recognition and Polymers: Control of Polymer Structure and Self-Assembly*. (ed. V.T. Rotello, S.) 179-206 (Wiley, Hoboken; 2008).

54. Kreft, O., Javier, A.M., Sukhorukov, G.B. & Parak, W.J. Polymer microcapsules as mobile local pH-sensors. *Journal of Materials Chemistry* **17**, 4471-4476 (2007).
55. Rivera-Gil, P., De Koker, S., De Geest, B.G. & Parak, W.J. Intracellular processing of proteins mediated by biodegradable polyelectrolyte capsules. *Nano Lett* **9**, 4398-4402 (2009).
56. De Geest, B.G. et al. Polyelectrolyte microcapsules for biomedical applications. *Soft Matter* **5**, 282-291 (2009).
57. Kobaslija, M. & McQuade, D.T. Polyurea microcapsules from oil-in-oil emulsions via interfacial polymerization. *Macromolecules* **39**, 6371-6375 (2006).
58. Poe, S.L., Kobaslija, M. & McQuade, D.T. Microcapsule enabled multicatalyst system. *Journal of the American Chemical Society* **128**, 15586-15587 (2006).
59. Price, K.E. et al. Microencapsulated linear polymers: "Soluble" heterogeneous catalysts. *Journal of the American Chemical Society* **128**, 10376-10377 (2006).
60. Poe, S.L., Kobaslija, M. & McQuade, D.T. Mechanism and application of a microcapsule enabled multicatalyst reaction. *Journal of the American Chemical Society* **129**, 9216-9221 (2007).
61. del Mercato, L.L. et al. LbL multilayer capsules: recent progress and future outlook for their use in life sciences. *Nanoscale* **2**, 458-467 (2010).
62. van Meer, G. Membrane curvature sorts lipids - Stabilized lipid rafts in membrane transport. *Embo Reports* **6**, 418-419 (2005).
63. Kolb, H.C., Finn, M.G. & Sharpless, K.B. Click chemistry: Diverse chemical function from a few good reactions. *Angewandte Chemie-International Edition* **40**, 2004-2021 (2001).
64. Wang, Q., Chittaboina, S. & Barnhill, H.N. Advances in 1,3-dipolar cycloaddition reaction of azides and alkynes - A prototype of "click" chemistry. *Letters in Organic Chemistry* **2**, 293-301 (2005).
65. Zhan, W.H., Barnhill, H.N., Sivakumar, K., Tian, T. & Wang, Q. Synthesis of hemicyanine dyes for 'click' bioconjugation. *Tetrahedron Letters* **46**, 1691-1695 (2005).
66. Ikeda, M. et al. Complex formation between cationic beta-1,3-glucan and hetero-sequence oligodeoxynucleotide and its delivery into macrophage-like cells to induce cytokine secretion. *Organic & Biomolecular Chemistry* **5**, 2219-2224 (2007).
67. Levy-Nissenbaum, E., Radovic-Moreno, A.F., Wang, A.Z., Langer, R. & Farokhzad, O.C. Nanotechnology and aptamers: applications in drug delivery. *Trends in Biotechnology* **26**, 442-449 (2008).

68. Hassane, F.S., Saleh, A.F., Abes, R., Gait, M.J. & Lebleu, B. Cell penetrating peptides: overview and applications to the delivery of oligonucleotides. *Cellular and Molecular Life Sciences* **67**, 715-726 (2010).
69. Lerman, L.S. Structure of DNA-acridine complex. *Proceedings of the National Academy of Sciences of the United States of America* **49**, 94-& (1963).
70. Teipel, U. (ed.) *Energetic Materials: Processing and Characterization of Particles*. (Wiley-VCH, Weinheim; 2005).
71. Choi, C.S. & Prince, E. Crystal-Structure of Cyclotrimethylene-Trinitramine. *Acta Crystallographica Section B-Structural Crystallography and Crystal Chemistry* **B 28**, 2857-& (1972).
72. Unknown in NIMIC/NATO(2004).
73. A. Freche, J.A., L. Donnio, and C. Spyckerelle in *Insensitive Munitions and Energetic Materials Symposium*, San Antonio, Texas, USA; (2000).
74. van der Heijden, A. et al. Energetic materials: Crystallization, characterization and insensitive plastic bonded explosives. *Propellants Explosives Pyrotechnics* **33**, 25-32 (2008).
75. L. Borne, A.B. in *12th International Detonation Symposium*, San Diego, California, USA; (2002).
76. I. J. Lochert, M.D.F., and B.L. Hamshere in *DSTO Systems Sciences Laboratory*, Edinburgh, Australia; (2003).
77. Armstrong, R.W. & Elban, W.L. Materials science and technology aspects of energetic (explosive) materials. *Materials Science and Technology* **22**, 381-395 (2006).
78. van der Heijden, A., Bouma, R.H.B. & van der Steen, A.C. Physicochemical parameters of nitramines influencing shock sensitivity. *Propellants Explosives Pyrotechnics* **29**, 304-313 (2004).
79. McGrane, S.D., Grieco, A., Ramos, K.J., Hooks, D.E. & Moore, D.S. Femtosecond micromachining of internal voids in high explosive crystals for studies of hot spot initiation. *Journal of Applied Physics* **105** (2009).
80. Armstrong, R.W. Dislocation Mechanics Aspects of Energetic Material Composites. *Reviews on Advanced Materials Science* **19**, 13-40 (2009).
81. Armstrong, R.W. Dislocation Mechanisms for Shock-Induced Hot-Spots. *Journal De Physique Iv* **5**, 89-102 (1995).

82. Stoltz, C.A., Mason, B.P. & Hooper, J. Neutron scattering study of internal void structure in RDX. *Journal of Applied Physics* **107** (2010).
83. Kim, D.Y. & Kim, K.J. Semi-quantitative Study on the Inclusion in Cooling Crystallization of RDX Using Various Solvents. *Propellants Explosives Pyrotechnics* **35**, 38-45 (2010).
84. Patil, M.N., Gore, G.M. & Pandit, A.B. Ultrasonically controlled particle size distribution of explosives: A safe method. *Ultrasonics Sonochemistry* **15**, 177-187 (2008).
85. W. H. M. Veltmans, A.E.D.M.v.d.H. in Proceedings of 14th International Symposium on Industrial Crystallisation (ICChemE), Cambridge, UK; (1995).
86. Elwenspoek, M., Bennema, P. & Vandereerden, J.P. Orientational Order in Naphthalene Crystal Solution Interfaces. *Journal of Crystal Growth* **83**, 297-305 (1987).
87. Roberts, C.W., Hira, S.M., Mason, B.P., Strouse, G.F. & Stoltz, C.A. Controlling RDX explosive crystallite morphology and inclusion content via simple ultrasonic agitation and solvent evaporation. *CrystEngComm* **13**, 1074-1076 (2011).
88. A. E. D. M. van der Heijde, W.D., C. J. M. van der Wulp in Proceedings of the 30th International Annual Conference of ICT, Karlsruhe, Germany; (1999).
89. van der Heijden, A. & Bouma, R.H.B. Crystallization and characterization of RDX, HMX, and CL-20. *Crystal Growth & Design* **4**, 999-1007 (2004).
90. Lim, D.V., Simpson, J.M., Kearns, E.A. & Kramer, M.F. Current and developing technologies for monitoring agents of bioterrorism and biowarfare. *Clinical Microbiology Reviews* **18**, 583-607 (2005).
91. Ivnitski, D. et al. Nucleic acid approaches for detection and identification of biological warfare and infectious disease agents. *Biotechniques* **35**, 862-869 (2003).
92. Ince, J. & McNally, A. Development of rapid, automated diagnostics for infectious disease: advances and challenges. *Expert Review of Medical Devices* **6**, 641-651 (2009).
93. Giljohann, D.A. & Mirkin, C.A. Drivers of biodiagnostic development. *Nature* **462**, 461-464 (2009).
94. Lazcka, O., Del Campo, F.J. & Munoz, F.X. Pathogen detection: A perspective of traditional methods and biosensors. *Biosensors & Bioelectronics* **22**, 1205-1217 (2007).
95. Wang, J. Electrochemical biosensors: Towards point-of-care cancer diagnostics. *Biosensors & Bioelectronics* **21**, 1887-1892 (2006).

96. Plutowski, U., Jester, S.S., Lenhert, S., Kappes, M.M. & Richert, C. DNA-based self-sorting of nanoparticles on gold surfaces. *Advanced Materials* **19**, 1951-1956 (2007).
97. Gabureac, M., Bernau, L., Utke, I. & Boero, G. Granular Co-C nano-Hall sensors by focused-beam-induced deposition. *Nanotechnology* **21**.
98. Bain, C.D. et al. Formation of monolayer films by the spontaneous assembly of organic thiols from solution onto gold. *Journal of the American Chemical Society* **111**, 321-335 (1989).
99. Herne, T.M. & Tarlov, M.J. Characterization of DNA probes immobilized on gold surfaces. *Journal of the American Chemical Society* **119**, 8916-8920 (1997).
100. Wink, T., vanZuilen, S.J., Bult, A. & vanBennekom, W.P. Self-assembled monolayers for biosensors. *Analyst* **122**, R43-R50 (1997).
101. Festag, G. et al. Optimization of gold nanoparticle-based DNA detection for microarrays. *Journal of Fluorescence* **15**, 161-170 (2005).
102. Song, X.D., Shi, J. & Swanson, B. Flow cytometry-based biosensor for detection of multivalent proteins. *Anal. Biochem.* **284**, 35-41 (2000).
103. Shi, L.M. et al. The MicroArray Quality Control (MAQC) project shows inter- and intraplatform reproducibility of gene expression measurements. *Nature Biotechnology* **24**, 1151-1161 (2006).
104. Cao, Y.W.C., Jin, R.C. & Mirkin, C.A. Nanoparticles with Raman spectroscopic fingerprints for DNA and RNA detection. *Science* **297**, 1536-1540 (2002).
105. Campbell, C.T. & Kim, G. SPR microscopy and its applications to high-throughput analyses of biomolecular binding events and their kinetics. *Biomaterials* **28**, 2380-2392 (2007).
106. Taton, T.A., Mirkin, C.A. & Letsinger, R.L. Scanometric DNA array detection with nanoparticle probes. *Science* **289**, 1757-1760 (2000).
107. Dubertret, B., Calame, M. & Libchaber, A.J. Single-mismatch detection using gold-quenched fluorescent oligonucleotides. *Nature Biotechnology* **19**, 365-370 (2001).
108. Algar, W.R., Massey, M. & Krull, U.J. The application of quantum dots, gold nanoparticles and molecular switches to optical nucleic-acid diagnostics. *Trac-Trends in Analytical Chemistry* **28**, 292-306 (2009).
109. Husale, S., Persson, H.H.J. & Sahin, O. DNA nanomechanics allows direct digital detection of complementary DNA and microRNA targets. *Nature* **462**, 1075-1078 (2009).

110. Clack, N.G., Salaita, K. & Groves, J.T. Electrostatic readout of DNA microarrays with charged microspheres. *Nature Biotechnology* **26**, 825-830 (2008).
111. Johnson, D.S. et al. Systematic evaluation of variability in ChIP-chip experiments using predefined DNA targets. *Genome Research* **18**, 393-403 (2008).
112. Algar, W.R. & Krull, U.J. Toward A Multiplexed Solid-Phase Nucleic Acid Hybridization Assay Using Quantum Dots as Donors in Fluorescence Resonance Energy Transfer. *Analytical Chemistry* **81**, 4113-4120 (2009).
113. Gaylord, B.S., Heeger, A.J. & Bazan, G.C. DNA detection using water-soluble conjugated polymers and peptide nucleic acid probes. *Proceedings of the National Academy of Sciences of the United States of America* **99**, 10954-10957 (2002).
114. Zhang, J., Ting, B.P., Jana, N.R., Gao, Z.Q. & Ying, J.Y. Ultrasensitive Electrochemical DNA Biosensors Based on the Detection of a Highly Characteristic Solid-State Process. *Small* **5**, 1414-1417 (2009).
115. Li, Y.G., Cu, Y.T.H. & Luo, D. Multiplexed detection of pathogen DNA with DNA-based fluorescence nanobarcodes. *Nature Biotechnology* **23**, 885-889 (2005).
116. Qin, W.J., Yim, O.S., Lai, P.S. & Yung, L.Y.L. Dimeric gold nanoparticle assembly for detection and discrimination of single nucleotide mutation in Duchenne muscular dystrophy. *Biosensors & Bioelectronics* **25**, 2021-2025.
117. Peterson, A.W., Heaton, R.J. & Georgiadis, R.M. The effect of surface probe density on DNA hybridization. *Nucleic Acids Research* **29**, 5163-5168 (2001).
118. Martins, V.C. et al. Femtomolar limit of detection with a magnetoresistive biochip. *Biosensors & Bioelectronics* **24**, 2690-2695 (2009).
119. Mirkin, C.A., Letsinger, R.L., Mucic, R.C. & Storhoff, J.J. A DNA-based method for rationally assembling nanoparticles into macroscopic materials. *Nature* **382**, 607-609 (1996).
120. Storhoff, J.J. et al. Gold nanoparticle-based detection of genomic DNA targets on microarrays using a novel optical detection system. *Biosensors & Bioelectronics* **19**, 875-883 (2004).
121. Storhoff, J.J., Lucas, A.D., Garimella, V., Bao, Y.P. & Muller, U.R. Homogeneous detection of unamplified genomic DNA sequences based on colorimetric scatter of gold nanoparticle probes. *Nature Biotechnology* **22**, 883-887 (2004).
122. Braun, G. et al. Surface-enhanced Raman spectroscopy for DNA detection by nanoparticle assembly onto smooth metal films. *Journal of the American Chemical Society* **129**, 6378-6379 (2007).

123. Arruda, D.L. et al. Microelectrical sensors as emerging platforms for protein biomarker detection in point-of-care diagnostics. *Expert Review of Molecular Diagnostics* **9**, 749-755 (2009).
124. Schotter, J. et al. Comparison of a prototype magnetoresistive biosensor to standard fluorescent DNA detection. *Biosensors & Bioelectronics* **19**, 1149-1156 (2004).
125. Germano, J. et al. A portable and autonomous magnetic detection platform for biosensing. *Sensors* **9**, 4119-4137 (2009).
126. Graham, D.L. et al. Magnetic field-assisted DNA hybridisation and simultaneous detection using micron-sized spin-valve sensors and magnetic nanoparticles. *Sensors and Actuators B-Chemical* **107**, 936-944 (2005).
127. Ferreira, H.A. et al. Detection of cystic fibrosis related DNA targets using AC field focusing of magnetic labels and spin-valve sensors. *Ieee Transactions on Magnetics* **41**, 4140-4142 (2005).
128. Hall, D.A. et al. GMR biosensor arrays: A system perspective. *Biosensors & Bioelectronics* **25**, 2051-2057 (2010).
129. Osterfeld, S.J. et al. Multiplex protein assays based on real-time magnetic nanotag sensing. *Proceedings of the National Academy of Sciences of the United States of America* **105**, 20637-20640 (2008).
130. Baselt, D.R. et al. A biosensor based on magnetoresistance technology. *Biosensors & Bioelectronics* **13**, 731-739 (1998).
131. Edelstein, R.L. et al. The BARC biosensor applied to the detection of biological warfare agents. *Biosensors & Bioelectronics* **14**, 805-813 (2000).
132. Li, Y.Q. et al. Hall magnetometry on a single iron nanoparticle. *Applied Physics Letters* **80**, 4644-4646 (2002).
133. Sandhu, A. et al. High efficiency Hall effect micro-biosensor platform for detection of magnetically labeled biomolecules. *Biosensors & Bioelectronics* **22**, 2115-2120 (2007).
134. Mihajlovic, G. et al. Detection of single magnetic bead for biological applications using an InAs quantum-well micro-Hall sensor. *Applied Physics Letters* **87**, 112502 (2005).
135. Mihajlovic, G., Xiong, P., von Molnar, S., Field, M. & Sullivan, G.J. InAs quantum well Hall devices for room-temperature detection of single magnetic biomolecular labels. *Journal of Applied Physics* **102**, 034506 (2007).
136. Manandhar, P. et al. The detection of specific biomolecular interactions with micro-Hall magnetic sensors. *Nanotechnology* **20**, 35501 (2009).

137. Besse, P.A., Boero, G., Demierre, M., Pott, V. & Popovic, R. Detection of a single magnetic microbead using a miniaturized silicon Hall sensor. *Applied Physics Letters* **80**, 4199-4201 (2002).
138. Gaster, R.S. et al. Matrix-insensitive protein assays push the limits of biosensors in medicine. *Nature Medicine* **15**, 1327-1332 (2009).
139. Mihajlovic, G., von Molnar, S in *Nanoscale Magnetic Materials and Applications*. (ed. J.P. Liu, Fullerton, E., Gutfleisch, O., Sellmyer, D.J.) 685-710 (Springer, New York; 2009).
140. Behet, M., Bekaert, J., De Boeck, J. & Borghs, G. InAs/Al<sub>0.2</sub>Ga<sub>0.8</sub>Sb quantum well Hall effect sensors. *Sensors and Actuators a-Physical* **81**, 13-17 (2000).
141. Ron, H. & Rubinstein, I. Alkanethiol monolayers on preoxidized gold-encapsulation of gold oxide under an organic monolayer. *Langmuir* **10**, 4566-4573 (1994).
142. Tsai, M.Y. & Lin, J.C. Preconditioning gold substrates influences organothiol self-assembled monolayer (SAM) formation. *Journal of Colloid and Interface Science* **238**, 259-266 (2001).
143. Kannan, B., Kulkarni, R.P. & Majumdar, A. DNA-based programmed assembly of gold nanoparticles on lithographic patterns with extraordinary specificity. *Nano Letters* **4**, 1521-1524 (2004).
144. Gonzalez, M., Argarana, C.E. & Fidelio, G.D. Extremely high thermal stability of streptavidin and avidin upon biotin binding. *Biomolecular Engineering* **16**, 67-72 (1999).
145. Lee, C.Y. et al. Surface coverage and structure of mixed DNA/alkylthiol monolayers on gold: Characterization by XPS, NEXAFS, and fluorescence intensity measurements. *Analytical Chemistry* **78**, 3316-3325 (2006).
146. Demers, L.M. et al. Direct patterning of modified oligonucleotides on metals and insulators by dip-pen nanolithography. *Science* **296**, 1836-1838 (2002).
147. Kohler, J. et al. Familial hypertrophic cardiomyopathy mutations in troponin I (K183 Delta, G203S, K206Q) enhance filament sliding. *Physiological Genomics* **14**, 117-128 (2003).
148. Parmacek, M.S. & Solaro, R.J. Biology of the troponin complex in cardiac myocytes. *Progress in Cardiovascular Diseases* **47**, 159-176 (2004).
149. Sang, Q.X.A. et al. Matrix metalloproteinase inhibitors as prospective agents for the prevention and treatment of cardiovascular and neoplastic diseases. *Current Topics in Medicinal Chemistry* **6**, 289-316 (2006).

150. Rodriguez, D., Morrison, C.J. & Overall, C.M. Matrix metalloproteinases: What do they not do? New substrates and biological roles identified by murine models and proteomics. *Biochimica Et Biophysica Acta-Molecular Cell Research* **1803**, 39-54 (2010).
151. Golubkov, V.S. et al. Membrane type-1 matrix metalloproteinase (MT1-MMP) exhibits an important intracellular cleavage function and causes chromosome instability. *Journal of Biological Chemistry* **280**, 25079-25086 (2005).
152. Mazzone, M. et al. Intracellular processing and activation of membrane type 1 matrix metalloprotease depends on its partitioning into lipid domains. *Journal of Cell Science* **117**, 6275-6287 (2004).
153. Wysocki, A.B., Staianoico, L. & Grinnell, F. Wound fluid from chronic leg ulcers contains elevated levels of metalloproteinases MMP-2 and MMP-9. *Journal of Investigative Dermatology* **101**, 64-68 (1993).
154. Golubkov, V.S. & Strongin, A.Y. Proteolysis-driven oncogenesis. *Cell Cycle* **6**, 147-150 (2007).
155. Hu, J.L., Van den Steen, P.E., Sang, Q.X.A. & Opdenakker, G. Matrix metalloproteinase inhibitors as therapy for inflammatory and vascular diseases. *Nature Reviews Drug Discovery* **6**, 480-498 (2007).
156. Wolf, K. et al. Multi-step pericellular proteolysis controls the transition from individual to collective cancer cell invasion. *Nature Cell Biology* **9**, 893-U839 (2007).
157. Cao, J. et al. Membrane type 1 matrix metalloproteinase induces epithelial-to-mesenchymal transition in prostate cancer. *Journal of Biological Chemistry* **283**, 6232-6240 (2008).
158. Nagase, H., Visse, R. & Murphy, G. Structure and function of matrix metalloproteinases and TIMPs. *Cardiovascular Research* **69**, 562-573 (2006).
159. Visse, R. & Nagase, H. Matrix metalloproteinases and tissue inhibitors of metalloproteinases - Structure, function, and biochemistry. *Circulation Research* **92**, 827-839 (2003).
160. Crocker, J. in *The Biology of Disease*, Edn. 2nd. (ed. J. Philips, Murray, P., Kish, P.R.) (Blackwell Science Ltd., Malden, MA, USA; 2001).
161. Vanwart, H.E. & Birkedalhansen, H. The cysteine switch - a principle of regulation of metalloproteinase activity with potential applicability to the entire matrix metalloproteinase gene family. *Proceedings of the National Academy of Sciences of the United States of America* **87**, 5578-5582 (1990).

162. Zitka, O. et al. Matrix Metalloproteinases. *Current Medicinal Chemistry* **17**, 3751-3768 (2010).
163. Jiang, A.X. et al. Regulation of membrane-type matrix metalloproteinase 1 activity by dynamin-mediated endocytosis. *Proceedings of the National Academy of Sciences of the United States of America* **98**, 13693-13698 (2001).
164. Remacle, A.G., Rozanov, D.V., Fugere, M., Day, R. & Strongin, A.Y. Furin regulates the intracellular activation and the uptake rate of cell surface-associated MT1-MMP. *Oncogene* **25**, 5648-5655 (2006).
165. Cao, J., Chiarelli, C., Kozarekar, P. & Adler, H.L. Membrane type I-matrix metalloproteinase promotes human prostate cancer invasion and metastasis. *Thrombosis and Haemostasis* **93**, 770-778 (2005).
166. Gonzalo, P., Moreno, V., Galvez, B.G. & Arroyo, A.G. MT1-MMP and integrins: Hand-to-hand in cell communication. *Biofactors* **36**, 248-254 (2010).
167. Cauwe, B. & Opdenakker, G. Intracellular substrate cleavage: a novel dimension in the biochemistry, biology and pathology of matrix metalloproteinases. *Critical Reviews in Biochemistry and Molecular Biology* **45**, 351-423 (2010).
168. Nagase, H. & Woessner, J.F. Matrix metalloproteinases. *Journal of Biological Chemistry* **274**, 21491-21494 (1999).
169. Mazzieri, R. et al. Control of type IV collagenase activity by components of the urokinase-plasmin system: A regulatory mechanism with cell-bound reactants. *Embo Journal* **16**, 2319-2332 (1997).
170. Morrison, C.J. & Overall, C.M. TIMP independence of matrix metalloproteinase (MMP)-2 activation by membrane type 2 (MT2)-MMP is determined by contributions of both the MT2-MMP catalytic and hemopexin C domains. *Journal of Biological Chemistry* **281**, 26528-26539 (2006).
171. Zucker, S. et al. Tissue inhibitor of metalloproteinase-2 (TIMP-2) binds to the catalytic domain of the cell surface receptor, membrane type 1 matrix metalloproteinase 1 (MT1-MMP). *Journal of Biological Chemistry* **273**, 1216-1222 (1998).
172. Zucker, S., Hymowitz, M., Conner, C., DeClerck, Y. & Cao, J. TIMP-2 is released as an intact molecule following binding to MT1-MMP on the cell surface. *Experimental Cell Research* **293**, 164-174 (2004).
173. Uekita, T. et al. Membrane-type 1 matrix metalloproteinase cytoplasmic tail-binding protein-1 is a new member of the Cupin superfamily - A possible multifunctional protein acting as an invasion suppressor down-regulated in tumors. *Journal of Biological Chemistry* **279**, 12734-12743 (2004).

174. Itoh, Y. & Seiki, M. MT1-MMP: an enzyme with multidimensional regulation. *Trends in Biochemical Sciences* **29**, 285-289 (2004).
175. Frittoli, E., Palamidessi, A., Disanza, A., Scita, G. Secretory and endo/exocytic trafficking in invadopodia formation: The MT1-MMP paradigm. *European Journal of Cell Biology* **90**, 108-114 (2011).
176. Wu, Y.I. et al. Activation-coupled membrane-type 1 matrix metalloproteinase membrane trafficking. *Biochemical Journal* **407**, 171-177 (2007).
177. Bravo-Cordero, J.J. et al. MT1-MMP proinvasive activity is regulated by a novel Rab8-dependent exocytic pathway. *Embo Journal* **26**, 1499-1510 (2007).
178. Osenkowski, P., Toth, M. & Fridman, R. Processing, shedding, and endocytosis of membrane type 1-matrix metalloproteinase (MT1-MMP). *Journal of Cellular Physiology* **200**, 2-10 (2004).
179. Coussens, L.M., Fingleton, B. & Matrisian, L.M. Cancer therapy - Matrix metalloproteinase inhibitors and cancer: Trials and tribulations. *Science* **295**, 2387-2392 (2002).
180. Zucker, S. & Cao, J. Selective matrix metalloproteinase (MMP) inhibitors in cancer therapy Ready for prime time? *Cancer Biology & Therapy* **8**, 2371-2373 (2009).
181. Turk, B. Targeting proteases: successes, failures and future prospects. *Nature Reviews Drug Discovery* **5**, 785-799 (2006).
182. Drag, M. & Salvesen, G.S. Emerging principles in protease-based drug discovery. *Nature Reviews Drug Discovery* **9**, 690-701 (2010).
183. Pavlaki, M. & Zucker, S. Matrix metalloproteinase inhibitors (MMPi): The beginning of phase I or the termination of phase III clinical trials. *Cancer and Metastasis Reviews* **22**, 177-203 (2003).
184. Sparano, J.A. et al. Randomized phase III trial of marimastat versus placebo in patients with metastatic breast cancer who have responding or stable disease after first-line chemotherapy: Eastern Cooperative Oncology Group Trial E2196. *Journal of Clinical Oncology* **22**, 4683-4690 (2004).
185. Knight, C.G., Willenbrock, F. & Murphy, G. A novel coumarin-labeled peptide for sensitive continuous assays of the matrix metalloproteinases. *Febs Letters* **296**, 263-266 (1992).
186. Cobos-Correa, A., Trojanek, J.B., Diemer, S., Mall, M.A. & Schultz, C. Membrane-bound FRET probe visualizes MMP12 activity in pulmonary inflammation. *Nature Chemical Biology* **5**, 628-630 (2009).

187. Ouyang, M.X. et al. Simultaneous Visualization of Protumorigenic Src and MT1-MMP Activities with Fluorescence Resonance Energy Transfer. *Cancer Research* **70**, 2204-2212 (2010).
188. Ouyang, M.X. et al. Visualization of polarized membrane type 1 matrix metalloproteinase activity in live cells by fluorescence resonance energy transfer imaging. *Journal of Biological Chemistry* **283**, 17740-17748 (2008).
189. Zhao, T. et al. A novel strategy to tag matrix metalloproteinases-positive cells for in vivo imaging of invasive and metastatic activity of tumor cells. *Journal of Controlled Release* **144**, 109-114 (2010).
190. Zhang, Y., So, M.K. & Rao, J.H. Protease-modulated cellular uptake of quantum dots. *Nano Letters* **6**, 1988-1992 (2006).
191. Scherer, R.L., McIntyre, J.O. & Matrisian, L.M. Imaging matrix metalloproteinases in cancer. *Cancer and Metastasis Reviews* **27**, 679-690 (2008).
192. Bremer, C., Tung, C.H. & Weissleder, R. In vivo molecular target assessment of matrix metalloproteinase inhibition. *Nature Medicine* **7**, 743-748 (2001).
193. Faust, A. et al. Synthesis and evaluation of a novel fluorescent photoprobe for imaging matrix metalloproteinases. *Bioconjugate Chemistry* **19**, 1001-1008 (2008).
194. Faust, A. et al. Synthesis and Evaluation of a Novel Hydroxamate Based Fluorescent Photoprobe for Imaging of Matrix Metalloproteinases. *Bioconjugate Chemistry* **20**, 904-912 (2009).
195. Keller, U.A.D. et al. Novel Matrix Metalloproteinase Inhibitor [F-18]Marimastat-Aryltrifluoroborate as a Probe for In vivo Positron Emission Tomography Imaging in Cancer. *Cancer Research* **70**, 7562-7569 (2010).
196. Rouffet, M. et al. From Sensors to Silencers: Quinoline-and Benzimidazole-Sulfonamides as Inhibitors for Zinc Proteases. *Journal of the American Chemical Society* **132**, 8232-8233 (2010).
197. Park, H.I. et al. The intermediate S1 ' pocket of the endometase/matrixlysin-2 active site revealed by enzyme inhibition kinetic studies, protein sequence analyses, and homology modeling. *Journal of Biological Chemistry* **278**, 51646-51653 (2003).
198. Hurst, D.R. et al. Catalytic- and ecto-domains of membrane type 1-matrix metalloproteinase have similar inhibition profiles but distinct endopeptidase activities. *Biochemical Journal* **377**, 775-779 (2004).

199. Hurst, D.R. et al. Inhibition of enzyme activity of and cell-mediated substrate cleavage by membrane type 1 matrix metalloproteinase by newly developed mercaptosulphide inhibitors. *Biochemical Journal* **392**, 527-536 (2005).
200. Schwartz, M.A., Jin, Y., Hurst, D.R., Sang, Q.-X.A. "Substituted heterocyclic mercaptosulfide inhibitors" (Florida State University Research Foundation, Inc., USA). Application: WO/2005/032541; 2005).
201. Schwartz, M.A., Jin, Y., Sang, Q.-X.A. "Substituted heterocyclic mercaptosulfonamide metalloprotease inhibitors" (Florida State University Research Foundation, Inc., USA). Application: WO/2010/028051; 2010).
202. Grams, F. et al. Pyrimidine-2,4,6-triones: A new effective and selective class of matrix metalloproteinase inhibitors. *Biological Chemistry* **382**, 1277-1285 (2001).
203. Smith, S.N. & Steer, R.P. The photophysics of Lissamine rhodamine-B sulphonyl chloride in aqueous solution: implications for fluorescent protein-dye conjugates. *Journal of Photochemistry and Photobiology a-Chemistry* **139**, 151-156 (2001).
204. Haugland, R.P. The handbook: A guide to fluorescent probes and labeling technologies, Edn. 10th. (Invitrogen Corp., 2005).
205. Nagakawa, O. et al. Expression of membrane-type 1 matrix metalloproteinase (MT1-MMP) on prostate cancer cell lines. *Cancer Letters* **155**, 173-179 (2000).
206. Daja, M.M., Niu, X., Zhao, Z., Brown, J.M. & Russell, P.J. Characterization of expression of matrix metalloproteinases and tissue inhibitors of metalloproteinases in prostate cancer cell lines. *Prostate Cancer and Prostatic Diseases* **6**, 15-26 (2003).
207. Puri, C. et al. Overexpression of myosin VI in prostate cancer cells enhances PSA and VEGF secretion, but has no effect on endocytosis. *Oncogene* **29**, 188-200 (2010).
208. Dunn, T.A. et al. A novel role of myosin VI in human prostate cancer. *American Journal of Pathology* **169**, 1843-1854 (2006).
209. Soldati, T. & Schliwa, M. Powering membrane traffic in endocytosis and recycling. *Nature Reviews Molecular Cell Biology* **7**, 897-908 (2006).
210. Clark, I.M. Matrix metalloproteinase protocols (methods in molecular biology), Edn. 1st. (Humana Press, 2001).

# BIOGRAPHICAL SKETCH

STEVEN M. HIRA

## EDUCATION

---

**Florida State University**, Tallahassee, Florida, August 2004 - April 2011

Ph.D. in Inorganic Chemistry

Advisor: Prof. Geoffrey F. Strouse

Dissertation Title: *Targeted dye labeling as a tool for imaging material and biomaterial microenvironments*

**Roger Williams University**, Bristol, Rhode Island, September 1999 - December 2003

B.S in Chemistry, Marine Biology

## PUBLICATIONS

---

1. Hira, S.M., Jin, Y., Roycik, M.D., Bosco, D.B., Cao, J., Schwartz, M.A., Strouse, G.F., Sang, Q.X.A. Live-cell optical tracking of a novel dye labeled matrix metalloproteinase inhibitor (MMPI) in prostate cancer cells. *Manuscript in preparation*.
2. Hira, S.M., Aledealat, K., Chen, K., Field, M., Sullivan, G.J., Chase, P.B., Xiong, P., von Molnár, S., Strouse, G.F. Detection of target single stranded DNA using a micro-fabricated Hall magnetometer with correlated optical readout. *Manuscript submitted*.
3. Roberts, C.W., Hira, S.M., Mason, B.P., Strouse, G.F., Stoltz, C.A. Controlling RDX explosive crystallite morphology and inclusion content *via* simple ultrasonic agitation and solvent evaporation. *CrystEngComm* **13**, 1074-1076 (2011).
4. Mason, B.P., Hira, S.M., Strouse, G.F., McQuade, D.T. Microcapsules with three orthogonal reactive sites. *Organic Letters* **11**(7), 1479-1482 (2009).
5. Yuan, J., Hira, S.M., Strouse, G.F., Hirst, L.S. Lipid Bilayer Discs and Banded Tubules: Photoinduced lipid sorting in ternary mixtures. *Journal of the American Chemical Society* **130**(6), 2067-2072 (2008).
6. Sarno, D.M., Martin, J.J., Hira, S.M., Timpson, C.J., Gaffney, J.P., Jones, W.E., Jr. Enhanced conductivity of thin film polyaniline by self-assembled transition metal complexes. *Langmuir* **23**(2), 879-884 (2007).
7. Yun, C.S., Javier, A., Jennings, T., Fisher, M.; Hira, S., Peterson, S., Hopkins, B., Reich, N.O., Strouse, G.F. Nanometal surface energy transfer in optical rulers, breaking the FRET barrier. *Journal of the American Chemical Society* **127**(9), 3115-3119 (2005).

## PATENTS

---

1. U.S. Provisionary Patent Application No. 61/393,981 - (2010)  
“Devices and Methods for Detection of Biomolecular Interactions”

## CONFERENCE PRESENTATIONS (presented, co-authored)

---

2010 - 54<sup>th</sup> Biophysical Society National Meeting, San Francisco, CA - Poster - 2107-POS. Hira, S.M., Aledealat, K., Chen, K., Xiong, P., von Molnár, S., Chase, P.B., Strouse, G.F. “Magnetic and fluorescence detection of hybridized DNA assemblies immobilized onto a Hall device“

2008 - American Physical Society March Meeting, New Orleans, LA. Aledealat, K., Hira, S.M., Chen, K., Mihajlovic, G., Xiong, P., Strouse, G.F., Chase, P.B., Field, M., Sullivan, G.J. “InAs quantum well  $\mu$ -Hall sensors for magnetic biosensing“

2008 - 52<sup>nd</sup> Biophysical Society National Meeting, Long Beach, CA - Poster - 1666-POS. Hira, S.M., Aledealat, K., Xiong, P., von Molnár, S., Strouse, G.F., Chase, P.B. “Fluorescence and magnetic detection of hybridized DNA assemblies on a micro-Hall device“

2007 - 234<sup>th</sup> American Chemical Society National Meeting, Boston, MA - Poster - ANYL-140. Hira, S.M., Strouse, G.F., Chase, P.B., Xiong, P., von Molnár, S. “Fluorescent and magnetic detection of controlled DNA assemblies on Au patterned SiO<sub>2</sub> devices“

2007 - Materials Research Society National Meeting, Boston, MA - Oral - PP8.5. Hira, S.M., Xiong, P., von Molnár, S., Chase, P.B., Strouse, G.F. “Fluorescent and magnetic detection of hybridized DNA assemblies on a Au patterned SiO<sub>2</sub> device“

2006 - Materials Research Society National Meeting, Boston, MA - Oral - D17.4. Hira, S., Manandhar, P., Xiong, P., Chase, P.B., von Molnár, S., Strouse, G. “Optical and magnetic mismatch detection of controlled DNA assemblies onto Au patterned SiO<sub>2</sub> devices“

2004 - 228<sup>th</sup> American Chemical Society National Meeting, Philadelphia, PA – PMSE-207. Martin, J.J., Hira, S.M., Ochanda, F., Gaffney, J.P., Sarno, D.M., Jones, W.E. “Modification of conducting polymer thin films by self-assembled transition metal surfaces“

2003 - 225<sup>th</sup> American Chemical Society National Meeting, New Orleans, LA - Poster - CHED-699. Hira, S.M., Minnella, J.E., , Timpson, C.J. “Spectroelectrochemical investigations of ligand-bridged ruthenium complexes based on trans-trans-[Cl(pyridine)(4)Ru-(L)-Ru(pyridine)(4)Cl]“

2001 - 221<sup>st</sup> American Chemical Society National Meeting, San Diego, CA - Poster - CHED-40. Hira, S.M., Petrichko, R.J., Kuber, A.L., Nandor, H., Von Riesen, D.D., Timpson, C.J. "Synthesis and characterization of novel ligand-bridged ruthenium complexes"

2001 - 221<sup>st</sup> American Chemical Society National Meeting, San Diego, CA - CHED-362 Kuber, A., Nandor, H., Hira, S., Petrichko, R., Von Riesen, D.D., Timpson, C. "In-situ generation of trans-[Ru(pyridine)(4)(L)(solvent)](2+) obtained by Cl- abstraction from trans-[Ru(pyridine)(4)(L)(Cl)](+)"

2000 - 219<sup>th</sup> American Chemical Society National Meeting, San Francisco, CA - CHED-716. Calvo, D.R., Koehler, E.O., Grant, B.A., Kuber, A.L., Shah, N.K., Hira, S.M., Von Riesen, D.D., Timpson, C.J. "Synthesis and characterization of novel ligand-bridged ruthenium compounds"

## AWARDS AND FUNDING

---

Navy Surface Warfare Center (NSWC) - Indian Head Division (2010)

- \$10,000 Subcontract for microscopy characterization development and analysis of energetic materials

Hoffman Merit Award - Florida State University (2004)

- \$3,000 award to first year Teaching Assistants for previous academic achievements

Nation Science Foundation Research Experience for Undergraduates (NSF-REU) - (2003)

## MEMBERSHIPS/AFFILIATIONS

---

American Chemical Society (ACS)

Materials Research Society (MRS)

Biophysical Society

## EXPERIENCE

---

### **Graduate Research Assistant**

*Florida State University,*

August 2004 - April 2011

Advisor: Prof. Geoffrey F. Strouse

Research involved:

The use of optical probes for material and biomaterial imaging and detection

- Bio-functionalization and interfacing of condensed matter surfaces for bio-sensor applications
- Design and Syntheses of materials for optical detection (dye-labeling, Au nanoparticles)
- Synthetic DNA design and nanoparticle surface and bio-functionalization

- Material delivery into cells (CHO, HEK, HEKu, hMSC, LNCaP, LNCaP-GFP, LNCaP-MT1-GFP)
- Microscopy characterization included: Bright-field, Wide-field, Total Internal Reflectance Fluorescence (TIRF), Laser Scanning Confocal Microscopy (LCSM), Spectral Confocal Microscopy, Live-cell imaging, Atomic Force Microscopy (AFM), Scanning Electron Microscopy (SEM)
- Other skills/techniques included: Absorption (UV-Vis), Photoluminescence, Gel Electrophoresis, Chromatography (HPLC, FPLC, Ion Exchange, Size Exclusion), cell culture (BSL1, BSL2)

**Graduate Teaching Assistant** - Florida State University, 2004 - 2006, 2010

Courses Taught:

- General Chemistry I Lab, CHM 1045 (majors)
- General Chemistry II Recitation, CHM 1046 (majors)

Duties included:

- Prepared and provided lectures and quizzes
- Graded exams, quizzes and lab reports
- Encouraged and held office hours for one-on-one student consultations
- Demonstrated proper lab technique and safety

**Undergraduate Research Assistant**

*Roger Williams University,*

September 1999 - December 2003

Advisor: Prof. Cliff J. Timpson

Research involved:

Synthesized and characterized ruthenium polypyridyl complexes for alternative energy applications

Analytical techniques included:

Absorption (UV-Vis), infra-red (IR), Electrochemistry (cyclic voltammetry, bulk electrolysis, spectrophotometric studies)

**Undergraduate Research Assistant**

*State University of New York (SUNY) at Binghamton,*

NSF-REU, May 2003 - August 2003

Advisor: Prof. Wayne E. Jones, Jr.

Research involved:

Synthesized and characterized polymer thin films for inorganic hybrid materials for electronics packaging applications

Analytical techniques included:

Absorption (UV-Vis), IR, AFM, 4-probe conductivity

**Gordon Research Conference (GRC)**

Site Manager - *Roger Williams University*,  
May-August 2000 - 2002

Administrative duties involved:

Organized and maintained GRC conference site

Direct contact time with conference chair, conferees, RWU personnel

Managed 3 GRC staff

**ADDITIONAL SKILLS**

---

*Proficient with the following software:* Adobe Suite, Microsoft Office, Origin, Igor,  
Chem Office, Maple